Antiferroelectric–ferroelectric transition in binary systems of solid solutions based on sodium niobate

I. V. Pozdnyakova, L. A. Reznichenko, and V. G. Gavrilyachenko

Rostov State University, Physics Research Institute
(Submitted May 12, 1999)
Pis'ma Zh. Tekh. Fiz. **25**, 1–5 (October 12, 1999)

The dielectric properties of the $(1-x)\mathrm{NaNbO_3}-x\mathrm{KNbO_3}$ and $(1-x)\mathrm{NaNbO_3}-x\mathrm{PbTiO_3}$ systems are investigated. The antiferroelectric–ferroelectric transition regions are determined. It is established that in the $(1-x)\mathrm{NaNbO_3}-x\mathrm{KNbO_3}$ system the antiferroelectric phase is stable for $x \leq 0.01$ and the ferroelectric phase is stable for $x \geq 0.0175$; the transition from one phase into another occurs in the concentration range $0.01 < x < 0.0175$. In the $(1-x)\mathrm{NaNbO_3}-x\mathrm{PbTiO_3}$ system the transition region lies in the range $0.07 < x < 0.11$. © *1999 American Institute of Physics.* [S1063-7850(99)00110-X]

In some systems of solid solutions (SSs) based on $\mathrm{NaNbO_3}$, a ferroelectric (FE) phase, similar to the phase into which antiferroelectric (AFE) sodium niobate transforms in an external electric field, arises when the concentration of the second component is low.[1] Such systems include, specifically, $(1-x)\mathrm{NaNbO_3}-x\mathrm{LiNbO_3}$, $(1-x)\mathrm{NaNbO_3}-x\mathrm{KNbO_3}$, and $(1-x)\mathrm{NaNbO_3}-x\mathrm{PbTiO_3}$. There are many papers devoted to these systems, mainly because of their interesting physical properties and the possibility of wide practical applications,[2–4] but to date the AFE–FE transition region has not been studied in detail for the $(1-x)\mathrm{NaNbO_3}-x\mathrm{KNbO_3}$ and $(1-x)\mathrm{NaNbO_3}-x\mathrm{PbTiO_3}$ systems. Our objective in the present work is to determine the region of the AFE–FE transition in these systems and to compare the data obtained for various $\mathrm{NaNbO_3}$-based solid solutions.

I. SAMPLES AND EXPERIMENTAL PROCEDURE

Ceramic samples of $(1-x)\mathrm{NaNbO_3}-x\mathrm{KNbO_3}$ and $(1-x)\mathrm{NaNbO_3}-x\mathrm{PbTiO_3}$ were obtained by solid-phase syn-

thesis followed by hot pressing. Twenty $(1-x)\mathrm{NaNbO_3}-x\mathrm{KNbO_3}$ compositions from the concentration range $0 \leq x \leq 0.1$ were investigated with average step size $\Delta x \approx 0.005$, and twenty $(1-x)\mathrm{NaNbO_3}-x\mathrm{PbTiO_3}$ compositions from the concentration range $0 \leq x \leq 0.17$ were studied with average step size $\Delta x \approx 0.0085$. The temperature dependence of the permittivity $\varepsilon(T)$ with and without an electric field as well as the dielectric hysteresis loop were obtained. The experimental samples were prepared in the form of 8–10 mm in diameter and 1 mm thick disks. The electrodes were deposited by annealing silver paste.

The experimental apparatus made it possible to obtain $\varepsilon(T)$ by the bridge method ($f = 20$ kHz, $E_\sim = 10$ V/cm) with a constant electric field. To eliminate errors in determining the field acting on the sample, the conduction current was monitored; the field on the sample was 0.5–5 kV/cm. The concentration dependence of the transition temperatures ($T_c(x)$) and the variation of T_c under the action of the field
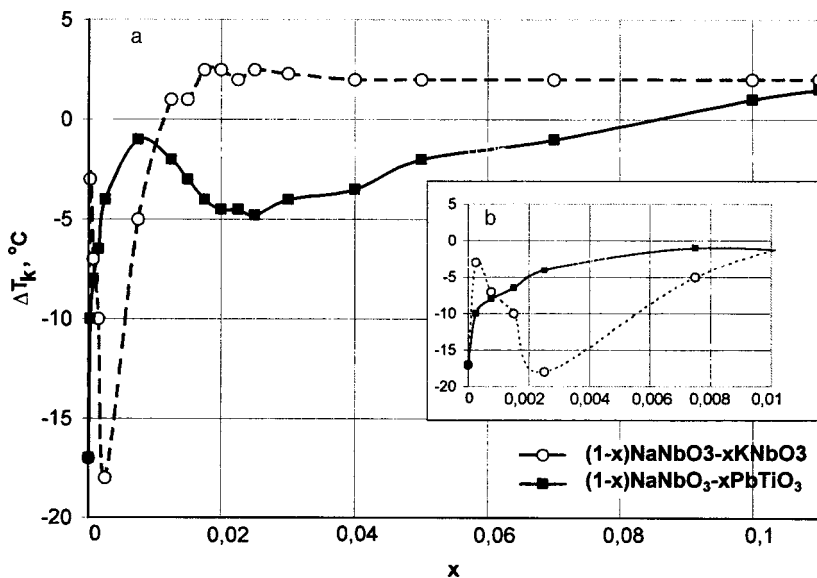

FIG. 1. Shift ΔT_c induced in the Curie temperature by a 1 kV/cm field versus the concentration x in the $(1-x)\mathrm{NaNbO_3}-x\mathrm{KNbO_3}$ and $(1-x)\mathrm{NaNbO_3}-x\mathrm{PbTiO_3}$ systems.
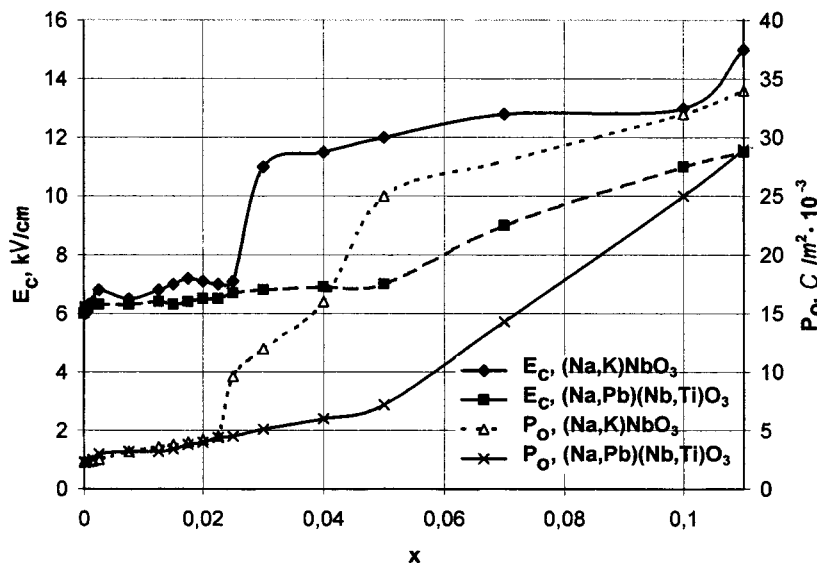
FIG. 2. Coercive field E_c and residual polarization P_r versus the concentration x in the $(1-x)$ NaNbO$_3$–xKNbO$_3$ and $(1-x)$NaNbO$_3$–xPbTiO$_3$ systems.

$(\Delta T_c(x))$ were determined from the data obtained in the temperature measurements.

The dielectric hysteresis loops were observed using a Sawyer–Tower scheme at room temperature and frequency 50 Hz; the field on the sample was 20–50 kV/cm. The dependence of the coercive field (E_c) and the residual polarization (P_r) on x was determined in these investigations.

II. RESULTS AND DISCUSSION

Figure 1 shows the changes ΔT_c in T_c for a constant electric field of 1 kV/cm versus x in the $(1-x)$ NaNbO$_3$–xKNbO$_3$ system (Fig. 1a) and the $(1-x)$ NaNbO$_3$–xPbTiO$_3$ system (Fig. 1b). It is evident that T_c for $(1-x)$NaNbO$_3$–xKNbO$_3$, $x \leqslant 0.01$, shifts in the direction of low temperatures in a field, as is characteristic of antiferroelectrics, while the shift for $x \geqslant 0.0175$ is in the opposite direction, as in ferroelectrics. In $(1-x)$NaNbO$_3$–xPbTiO$_3$ in an electric field T_c shifts in samples with $x \leqslant 0.07$ in the direction of low temperatures, while for $x \geqslant 0.11$ it shifts in the direction of high temperatures. The small peaks in the curves $\Delta T_c(x)$ for small values of x seem to be due to the high density of defects in these compositions.

Figure 2 shows the concentration dependence of the coercive field $E_c(x)$ and the residual polarization $P_r(x)$ for the $(1-x)$NaNbO$_3$–xKNbO$_3$ and $(1-x)$NaNbO$_3$–xPbTiO$_3$ systems. A large increase in E_c and P_r is observed at x

~ 0.01 in the former and at $x \sim 0.11$ in the latter.

In summary, our investigation shows that in $(1-x)$ NaNbO$_3$–xKNbO$_3$ the AFE phase is stable for $x \leqslant 0.01$, and in the FE phase it is stable for $x \geqslant 0.0175$; the transition from the AFE into the FE phase occurs in the range $0.01 < x < 0.0175$. In $(1-x)$NaNbO$_3$–xPbTiO$_3$ the AFE–FE transition occurs in the range $0.07 < x < 0.11$. The change in the phase state occurs in different concentration ranges in these systems because for heterovalent substitution in both cationic sublattices in $(1-x)$NaNbO$_3$–xPbTiO$_3$ a large number of vacancies can form, as a result of which the internal field acting on the ferroelectrically active cations can be much weaker than in $(1-x)$NaNbO$_3$–xKNbO$_3$, and the FE phase will stabilize at high impurity cation concentrations.

[1] *The Physics of Ferroelectric Phenomena*, edited by G. A. Smolenskiĭ (Nauka, Leningrad, 1985).
[2] A. V. Turik, V. A. Tais'eva, and L. A. Reznichenko, Izv. Akad. Nauk SSSR, Neorg. Mater. **14**, 912 (1978).
[3] O. N. Razumovskaya, L. A. Shilkina, and L. A. Reznichenko, Izv. Akad. Nauk SSSR, Neorg. Mater. **15**, 2207 (1979).
[4] L. A. Reznichenko, A. Ya. Dantsiger, and V. P. Sakhnenko, *Fundamental Problems of Piezoelectronics* (MP ''Kniga,'' Rostov University Press, Rostov-on-Don, 1995), Vol. 2, pp. 13–25.

Translated by M. E. Alferieff

Controllable electrochromic effect in a liquid-crystal cell with J aggregates

Yu. P. Piryatinskiĭ, V. G. Nazarenko, and O. V. Yatsun

Institute of Physics, Ukrainian National Academy of Sciences, Kiev
(Submitted February 5, 1999)
Pis'ma Zh. Tekh. Fiz. **25**, 6–10 (October 12, 1999)

It is shown that organic nanocrystals (J aggregates) can be successfully produced and oriented in a liquid-crystal matrix. An external electric field can reorient and destroy them. © *1999 American Institute of Physics.* [S1063-7850(99)00210-4]

Submicron-size organic and inorganic semiconductor particles are now getting close attention. Thus, J aggregates of certain molecular dyes have very high nonlinear cubic susceptibilities.[1] The extended (rod-shaped) form and the presence of a large electronic dipole along the axis of the aggregate are key properties for producing ''macroanisotropic'' media based on ordered J aggregates. Ordering of J aggregates in flowing solutions[2] and polymers[3] as a method for producing ''macroanisotropy'' is, in principle, static and uncontrollable. In the present work we investigate the behavior of J aggregates in a nematic liquid crystal, which, on the one hand, is characterized by long-range orientational order and, on the other, can reorient tehmeselves in an electric field.

Molecules of the model liquid crystal (LC) 5CB were chosen as the media for orienting J aggregates. Electrodes were sputtered on the inner surfaces of a 20-μm LC cell and layers of the orienting material were deposited. The orienting material fixed the required orientation of the 5CB molecules on the surface and in the interior volume of the cell (planar or homeotropic). A dye from the pseudoisocyanine family, astrophlonite, was used for the molecules that easily form J aggregates. The dye concentration in the LC was 0.5 wt.%. The formation of the planar or homeotropic orientation of the nematic phase of the mixture was monitored with a polarized optical microscope. The photoluminescence (PL) of the samples was excited by radiation from a mercury lamp with a maximum at $\lambda = 365$ nm and a nitrogen laser with a maximum at $\lambda = 337$ nm at right angles to the surface of the cell. The PL was recorded at a small angle with respect to the direction of excitation. If it is assumed that the radiative dipole moment of a 5CB molecule is directed along the molecular axis, then the PL anisotropy of a uniaxial LC can be related to the degree of ordering of the nematic phase as[4]

$$s = (I_{pl} - I_{pp})/(I_{pl} + 2I_{pp}), \qquad (1)$$

where I_{pl} and I_{pp} are the intensities of the PL components that are linearly polarized parallel and perpendicular to the polarization plane of the exciting radiation.

Figure 1 shows the polarized PL spectra of planar nematic phase of a LC with J aggregates for various experimental conditions: 1 — polarization of the exciting wave parallel to the direction of predominant orientation of the 5CB molecules and identical to the PL detection polarization and no orienting electric field; 2 — the same polarization conditions as for 1) but an ac electric field with frequency $f = 1$ kHz and amplitude $U_0 = 12$ V is applied to the electrodes of the cell; 3 — polarization of the exciting wave is parallel to the direction of rubbing of the orienting layer of the cell and orthogonal to the detection polarization of the PL of the LC, no orienting field; 4 — the polarization conditions are similar to 3), but an electric field with frequency $f = 1$ kHz and amplitude $U_0 = 12$ V is applied to the cell.

The characteristic time and concentration dependence of the PL of the dye allow one to relate the long-wavelength bands in Fig. 1 with the PL peak at $\lambda = 577$ nm to the emission of J aggregates. There is virtually no PL of the dye monomers because of the high degree of aggregation. The short-wavelength bands in Fig. 1 represent the PL of the matrix: 5CB molecules. An electric field applied to the LC cell substantially decreases the intensity of the PL of both the LC and the J aggregates. The PL decreases by approximately $\Delta I = 35\%$. The electrochromic effect for J aggregates can be observed visually. Without an electric field the cell is rose-colored, whereas in a field the cell is almost completely colorless.

The anisotropy of the PL (degree of ordering) of a planar LC and J aggregates can be estimated from Fig. 1 (1 and 3) using Eq. (1). Thus, the anisotropy at the peak PL for the LC is $s_{lc} = 0.61$, and for J aggregates $s_J = 0.49$. As we can see, the LC matrix imposes on the J aggregates an orientation isomorphic to the LC molecules, though the degree of the orientational ordering of the aggregates is less than for 5CB molecules. However, on the basis of the curves 2 and 4 in Fig. 1 it can be inferred that the values of s obtained are not the highest possible. Nonetheless, under the action of a high-frequency electric field the LC effectively reorients the J aggregates of the dye along the field. This is indicated not only by the PL spectra but also by microscopic investigations. Thus, if the dye concentration in the LC is increased to a value on the order of 1 wt.%, then microcrystals of the dye, which are visible under an optical microscope, will ''appear'' in the interior volume of the matrix. Reorientation of these microcrystals can be observed by applying a field to the electrodes of the cell. In this case the electrochromism is $\Delta I = 35\%$, but this is evidently not the maximum possible.

Let us consider a nematic LC with homeotropic orientation of 5CB molecules in the cell. The result for ideal homeotropic orientation, when the 5CB molecules make a strictly right angle with the surface of the cell, is obvious.
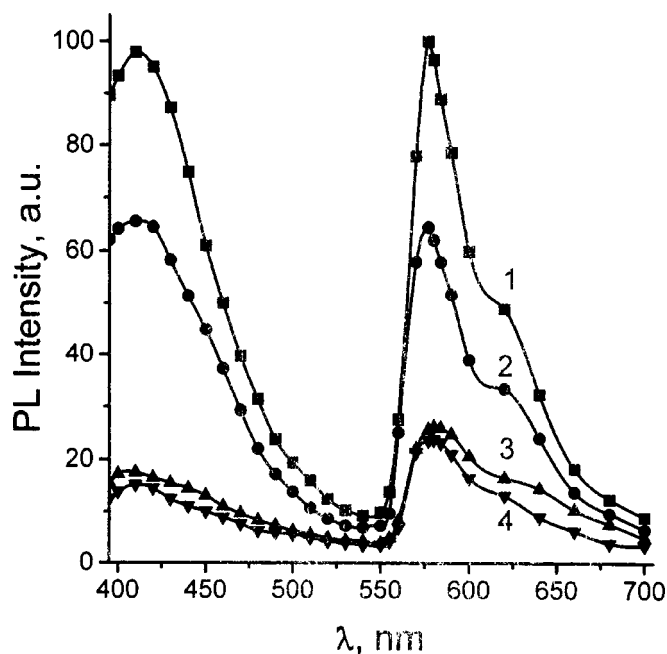
FIG. 1. Polarized PL spectra of a planar nematic 5CB with *J* aggregates. The experimental conditions are described in the text.
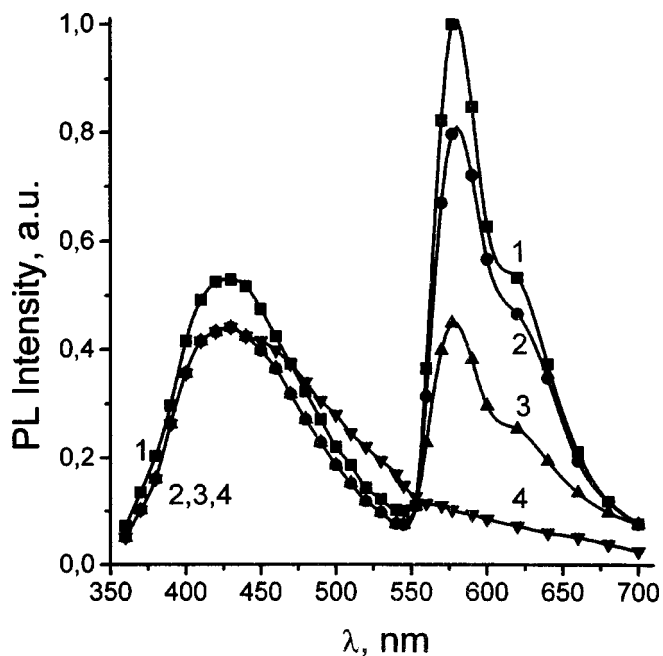

FIG. 2. PL spectra of a nematic LC and *J* aggregates with oblique homeotropic orientation of 5CB molecules: 1 — no field, 2–4 — an electric field with amplitude $U_0 = 12$ V and frequency $f = 100$–1000 (2), 10 (3), and 1 Hz (4) is applied to the electrodes of the cell.

Irrespective of the frequency and the intensity of the electric field and the wavelength of PL excitation, neither the 5CB itself nor the *J* aggregates in the LC matrix exhibit an electrochromic effect. The case of oblique homeotropic orientation, when the angle between the axis of the LC molecules and the substrate is somewhat different from a right angle, resembles the planar case. However, ΔI is much smaller here (Fig. 2). Depending on the specific homeotropic cell (angle of inclination of the 5CB molecules with respect to the substrate plane), ΔI can vary, but it does not exceed 10–15%.

Figure 2 also demonstrates the frequency effect of an electric field on the *J* aggregates. A field with $f > 100$ Hz nearly reorients *J* aggregates along the field. A low-frequency electric field without < 10 Hz effectively decomposes the *J* aggregates into individual molecules. In addition, the rate at which aggregates are converted into monomers rises as the field frequency *f* falls. Figure 2 (3 and 4) shows how a low-frequency electric field suppresses the *J* band and increases the intensity of the monomolecular PL. The intensity of the 5CB emission does not change much. *J* aggregates can also be rapidly destroyed by a low-frequency electric field if the cell is filled with a planar LC or any polar organic solvent. Electrohydrodynamic flows arising between the electrodes in a constant or low-frequency ac electric field in the cell give rise to degradation.

[1] V. L. Bogdanov, E. N. Viktorova, and S. V. Kulya, JETP Lett. **53**, 105 (1991).
[2] G. Scheibe, *Optische Anregungen organischer Systeme* (Verlag Chemie, Weinheim, 1966), p. 109.
[3] L. Misawa, H. Ono, and K. Minoshima, Appl. Phys. Lett. **63**, 577 (1993).
[4] L. M. Blinov, *Electro- and Magneto-Optical Properties of Liquid Crystals* (Wiley, New York, 1983; Nauka, Moscow, 1978).

Translated by M. E. Alferieff

High-transmission focusing x-ray diffractor: numerical simulation of the reflecting surface

M. I. Mazuritskiĭ, A. V. Soldatov, E. M. Latush, V. L. Lyashenko, and A. Marcelli

Rostov State University
(Submitted April 29, 1999)
Pis'ma Zh. Tekh. Fiz. **25**, 11–16 (October 12, 1999)

Models of stepped x-ray diffractors of a new type with ellipsoidal and toroidal step surfaces are calculated in the point x-ray source approximation. The Monte Carlo method is used to obtain an image of the diffraction zones of reflection and to investigate the influence of surface curvature on the shape and area of these zones. © *1999 American Institute of Physics.*
[S1063-7850(99)00310-9]

The principal dispersing components by means of which x-rays in a given wavelength range can be extracted are perfect crystals and crystals with a mosaic structure: quartz, silicon, germanium, lithium fluoride, mica, graphite, and others. The conventional crystal–diffraction methods for decomposing the x-ray radiation into a spectrum have been developed and described quite completely.[1–5] They employ reflection at the grazing angle θ (between the incident beam and the tangent plane at the point of incidence) from a system of atomic planes of the crystal. The condition for interference enhancement is the Bragg relation

$$n\lambda = 2d \sin\,\theta, \qquad (1)$$

where n is the diffraction order, λ is the radiation wavelength, and d is the interplanar spacing. The condition (1) holds for all diffracted rays. The resolving power increases as the parameter $\Delta\lambda/\lambda(\Delta E/E)$ falls off, where the value of the latter is determined by the mosaic imperfection of the crystal employed, by the method used to decompose the x-ray radiation into a spectrum, and by the size of the reflecting Bragg surface of the diffractor crystal. The Bragg (diffraction) zone of reflection is a set of points on the surface of the crystal for which in a prescribed wavelength range $\lambda - \Delta\lambda \leq \lambda \leq \lambda + \Delta\lambda$ the grazing angle satisfying Eq. (1) lies in the range $\theta - \Delta\theta \leq \theta \leq \theta + \Delta\theta$. The value of $\Delta\theta$ is determined from the condition

$$\Delta\theta = (\Delta\lambda/\lambda)\tan\,\theta. \qquad (2)$$

Ordinarily in practice a crystal is chosen so that its own degree $\Delta\theta$ of mosaic structure, determined from the rocking curve, is less than or equal to the degree fixed by the size of the reflecting Bragg zone.

It is obvious that the greater $\Delta\theta$, the larger the area of the diffraction zone and, in consequence, the higher the intensities of the spectra. Ordinarily, a compromise must be made between a quite high spectral resolution (associated with the small reflecting area of the crystal) and a large aperture of the diffractor. At present, reflection from flat or curved crystals is used to monochromatize x-ray radiation. These crystals are used for point sources of radiation and enable focusing of beans with a prescribed wavelength into the detection window of the detector.

In the present letter we propose a new method for numerical simulation of the shape of a diffraction zone on the surface of a curved crystal. The present approach makes it possible to determine, to a high degree of accuracy, the required geometric parameters, specifically, for a new class of diffractors[6–8] with a complicated stepped surface.

Ellipsoidal and toroidal curvatures are analyzed as examples. The cylindrical and spherical curvatures can be regarded as particular cases of ellipsoidal curvature. We shall apply the method for an arbitrary fixed resolution and angular interval $\Delta\theta$. The essence of the method is as follows. A function of the scalar product of two vectors directed away from a point $P(XYZ)$ on the surface of a diffractor crystal (Fig. 1) is obtained analytically: The vector $\mathbf{n}$ normal to the surface and the vector $\mathbf{PS}$ directed away from the diffraction zone into the point S on the focusing circle, where the source lies. The angle between these vectors is $90° - \theta$, since SP is the ray striking the point P of an atomic plane of the crystal:

$$\Phi(X,Y,Z) = \frac{(\mathbf{n} \cdot \mathbf{PS})}{|\mathbf{n}| \cdot |\mathbf{PS}|} = \sin\,(\theta \pm \Delta\theta). \qquad (3)$$

The point with the coordinates (X,Y,Z) lies in the Bragg reflection zone if the angle θ lies in the range $\theta \pm \Delta\theta$. Therefore the condition determining whether or not a point lies in the diffraction zone is

$$\sin\,(\theta - \Delta\theta) \leq \Phi(X,Y,Z) \leq \sin\,(\theta + \Delta\theta). \qquad (4)$$

In our case, we used the Monte Carlo method to visualize the diffraction region of reflection of the crystal and to estimate the relative surface area of this region. The calculations were performed on a pentium IBM PC. The point $P(X,Y,Z)$ was displayed on a screen and was considered to lie in the diffraction zone of reflection if the condition (4) was satisfied for the corresponding values of (X,Y,Z). Random numbers, which were ''dealt'' using a standard pseudorandom number generator, served as the coordinates (X,Z). The values of Y were calculated from the equations presented below, which give the curvature of the crystallographic planes.
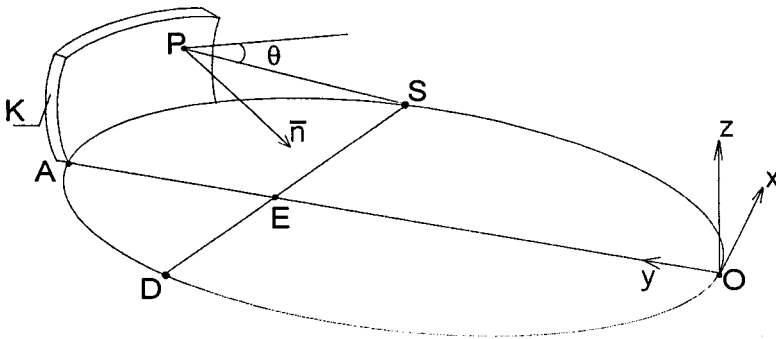
FIG. 1. Arrangement of the readout system, focusing circle, radiation source *S*, and normal vector **n** at a point *P* on the surface of the current crystal *K*.

As is well known, the equation for an ellipsoid of revolution representing a circle of radius *a* in the *XY* plane has the form

$$X^2 + Y^2 + \left(\frac{a}{b}\right)^2 Z^2 = 1, \tag{5}$$

where *X*, *Y*, and *Z* are dimensionless quantities, expressed in units of *a*.

The equation for a torus for which *a* is the radius of the axial circle in the *XY* plane and *b* is the radius of the circle of revolution around the *z* axis has the form

$$X^2 + Y^2 = \left(\frac{a}{a+b} + \sqrt{\left(\frac{b}{a+b}\right)^2 - Z^2}\right)^2, \tag{6}$$

where *X*, *Y*, and *Z* are dimensionless quantities, expressed in units of $a+b$.

The vector **n** normal at the point $P(X,Y,Z)$ and the vector **PS** can be expressed as follows:

$$\mathbf{PS} = (\cos\theta \sin\theta - X)\mathbf{i} + (\cos^2\theta - Y)\mathbf{j} - Z\mathbf{k}, \tag{7}$$

$$\mathbf{n} = -X\mathbf{i} - Y\mathbf{j} - \beta Z\mathbf{k}, \tag{8}$$

$$\beta = 1/\gamma^2, \quad \gamma = b/a \quad \text{for an ellipsoid of revolution,} \tag{9}$$

$$\beta = \frac{(1-\gamma) + \sqrt{\gamma^2 - Z^2}}{\sqrt{\gamma^2 - Z^2}}, \quad \gamma = \frac{b}{a+b} \quad \text{for a torus.} \tag{10}$$

Figure 2 displays plots of the area of the diffraction zone as a function of the curvature parameters of the crystal for an ellipsoid and a torus. The values of the area, normalized to the corresponding value S_1 for a spherical crystal, are plotted along the ordinate. Both curves are nonmonotonic. The maximum *C* in both plots corresponds to a ratio of the parameters such that the ellipsoid and the torus degenerate into a sphere. This occurs when the curvature in the *XY* plane is equal to the curvature of the crystal in the *YZ* plane, which corresponds to $a=b$ for an ellipsoid and $a+b \cong b$ ($a \ll b$) for a torus. The maximum *B* for an ellipsoidal diffractor is reached for $b = a\sin(\theta)$ which is the distance from the source *S* to the apex *A* of the curved crystal. For a torus, the position of the first peak corresponds to a different value of the radius of curvature in the *YZ* plane: $b = (a+b)\sin^2(\theta)$. In other words, the radius of curvature in the *YZ* plane is equal to the length of the segment *EA* (Fig. 1). In the plane of the focusing circle, this is the distance from the point of intersection of the chord connecting the source *S* and the detector

D to the apex of the crystal. Figure 2 also shows figures of the diffraction zones obtained by the Monte Carlo method for various values of the parameter γ. According to Eqs. (9) and (10) the dimensionless parameter γ is equal to the ratio b/a for an ellipsoid and $b/(a+b)$ for a torus. It is evident that the form of the Bragg zone depends strongly on the value of this parameter.

Recently, new principles were suggested[6–8] for constructing diffractors for x-ray spectroscopy and microanalysis that possess at the same time a high transmission and high spectral resolution. The approach described in the present letter made it possible to calculate the optimal curvature parameters of crystalline planes for these new types of x-ray diffractors. Specifically, in Ref. 8 it was proved that the new pseudospherical stepped diffractor is effective for use as a CAMEBAX x-ray microanalyzer (CAMECA Company).
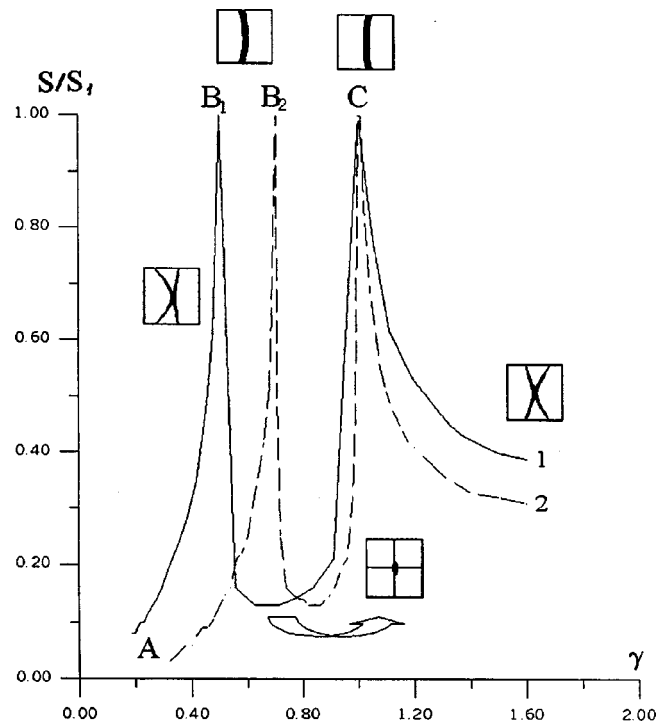

FIG. 2. Plots of the reduced area of the diffraction zone versus the curvature parameters of the crystal: 1 — for a torus, 2 — for an ellipsoid. Insets: Images of the Bragg diffraction zones in the parameter range corresponding to the closest points of the curve.

[1] A. G. Michette, *Optical System for Soft X-Rays,* (Plenum Press, New York, 1986), p 351.

[2] A. K. Freund, *X-Ray Optics,* (ESRF, Grenoble, 1987), p. 54.

[3] C. Bonnelle and C. Mande, *Advances in X-Ray Specroscopy* (Pergamon Press, New York, 1982), p. 423.

[4] D. B. Wittry and S. J. Sun, J. Appl. Phys. **67**, 1633 (1990).

[5] D. B. Wittry and S. J. Sun, J. Appl. Phys. **68**, 387 (1990).

[6] A. Marcelli, A. Soldatov, and M. Mazuritsky, European Patent, No. 7830282, 6–2208.

[7] A. Marcelli, A. Soldatov, and M. Mazuritsky, Japanese Patent, No. 39427/97.

[8] A. Marcelli, M. Mazuritsky, and A. Soldatov, in *Crystal and Multilayer Optics*, edited by A. Macrander, A. Freund, and T. Ishikawa. (SPIE, San Diego, 1998), Vol. 3448.

Translated by M. E. Alferieff

InAsSb/InAsSbP heterostructure lasers with a large range of current tuning of the lasing frequency

T. N. Danilova, A. P. Danilova, A. N. Imenkov, N. M. Kolchanova, M. V. Stepanov, V. V. Sherstnev, and Yu. P. Yakovlev

A. F. Ioffe Physicotechnical Institute, Russian Academy of Sciences, St. Petersburg, Russia
(Submitted May 13, 1999)
Pis'ma Zh. Tekh. Fiz. **25**, 17–23 (October 12, 1999)

The lasing spectra and the shift in the position of the modes in the current range $(1-5)I_{th}$ with various methods of pumping the nonequilibrium charge carriers are analyzed. It is shown that the pumping method does not influence the character of the tuning of the radiation line. The large short-wavelength tuning range (up to 50 Å) is due not to the heating of the crystal lattice in the active-region material but rather the nonuniform nonequilibrium charge-carrier density distribution over the width of the stripe. © *1999 American Institute of Physics.*
[S1063-7850(99)00410-3]

1. An important element of superhigh-resolution diode laser spectrometers is a frequency-tunable fast-response diode semiconductor laser. In previous work, we reported instantaneous, smooth current tuning of the lasing frequency of InAsSb/InAsSbP heterostructure diode lasers emitting near 3.3 μm.[1–7] It was found that smooth tuning of the lasing frequency of a diode laser is possible by varying the current in the range of longer and shorter wavelengths, which occurs at a rate higher than the thermal-relaxation rate.[1] In Ref. 6, a change in the radiation wavelength by 15 Å in the single-mode lasing regime, i.e., in a regime where the intensity of the predominant mode is greater than the total intensity of all other modes, was obtained in InAsSb/InAsSbP laser structures. Wavelength tuning by 30 Å into the short-wavelength region in structures with a small stripe width (10 μm) in a single-mode regime with a total shift of a single mode by 55 Å was reported in Ref. 4.

Our objective in the present work is to obtain a wider range of wavelength tuning of laser radiation in the single-mode lasing regime and to determine the effect of the method used to pump nonequilibrium charge carriers on the tuning process. For this, lasers with a larger strip width than in Ref. 4 were investigated.

2. We studied laser diodes based on the double heterostructures N-InAsSb$_{0.17}$P$_{0.35}$/n-InAsSb$_{0.05}$P/P-InAsSb$_{0.17}$P$_{0.35}$, obtained by liquid-phase epitaxy on a p-InAs substrate with hole density $(5-8) \cdot 10^{18}$ cm^{-3}. The active region was 1 μm thick, and the wide-gap emitters were 3 μm thick. The active region was not specially doped. The electron density in it was 10^{16} cm^{-3}. The N-InAsSbP layer was doped with Sn to electron density of about $1 \cdot 10^{18}$ cm^{-3}, and the P-InAsSbP layer was doped with Zn to density $(2-5) \cdot 10^{18}$ cm^{-3}. The arrangement of the layers and the energy diagram of the diode structures are shown in Fig. 1.

Mesostrips with a width of 16 μm were formed by photolithography on the structures grown. Fabry–Perot cavities of length 250–375 μm were obtained by cleaving. The laser was 500 μm wide in the region of the substrate, and the substrate was about 100 μm thick.

The investigations were performed at liquid-nitrogen temperature using various methods for pumping the nonequilibrium charge carriers: in the cw regime with the laser powered by short current pulses with 0.04 ms and a duty factor of 100, saw-tooth pulses with a repetition frequency from 10^2 to 10^4 Hz, and alternating square pulses with a duty factor of 2 and a 36 Hz repetition frequency.

The spectral composition of the radiation obtained with different methods of pumping and with different pump currents ranging from the threshold value I_{th} up to $5I_{th}$ was
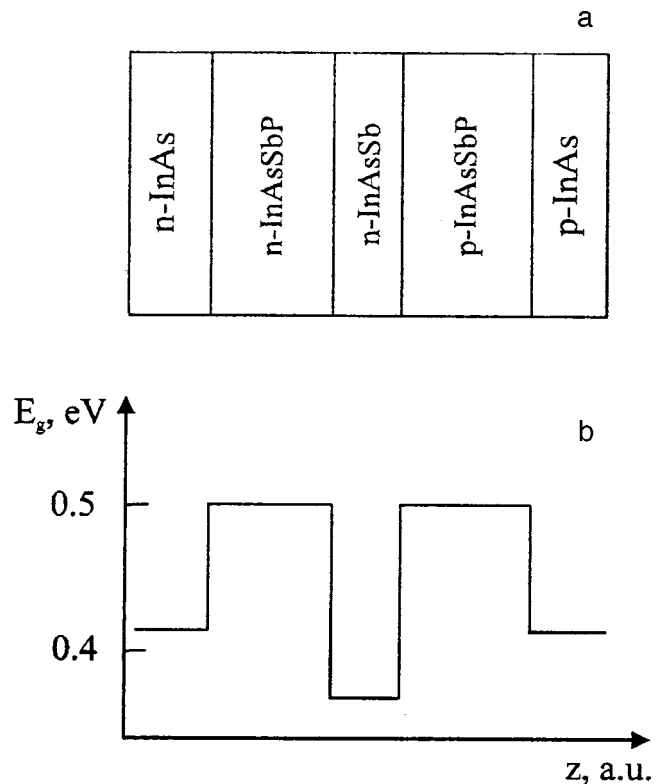

FIG. 1. Experimental laser structure: a — arrangement of the layers, b — energy diagram.
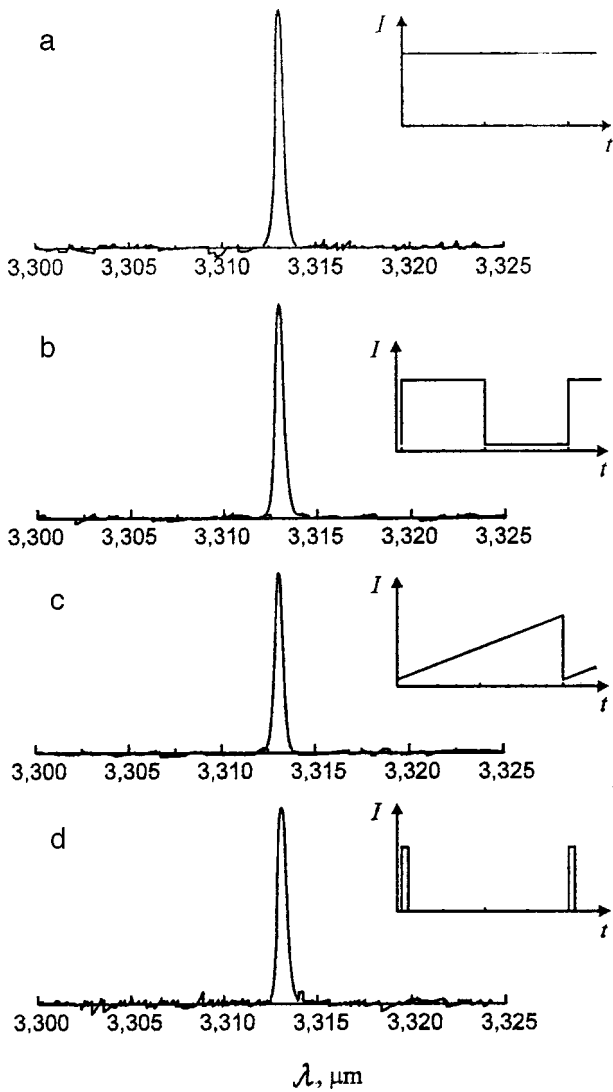
FIG. 2. Laser radiation spectra obtained with different methods of powering a V-12152-71 laser with $I = 1.1 I_{th}$: a — dc current, b — alternating square pulses, c — saw-tooth pulses, d — short pulses.
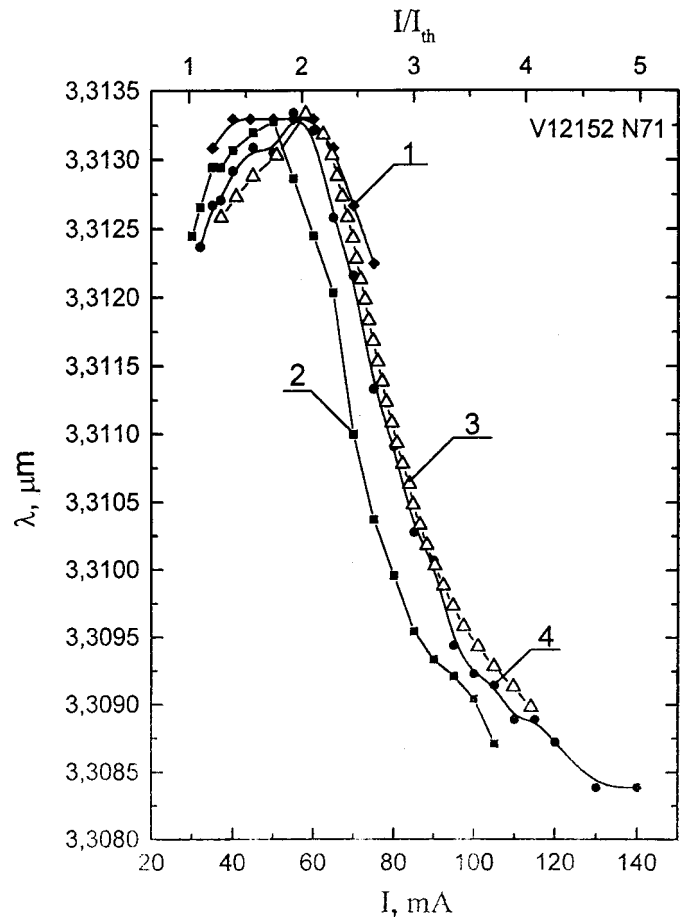

FIG. 3. Variation of the lasing wavelength of a V-12152-71 laser with the diode powered by a dc current (1), alternating square pulses with duty factor 2 (2), saw-tooth pulses (3), and short pulses (4).

studied on the diode laser structures. When the laser was powered by saw-tooth current pulses, the shift of the radiation mode was measured using a Fabry–Perot cavity.

3. The radiation spectrum of laser diodes near the lasing threshold with various pumping methods is displayed in Fig. 2. One mode is present with all currents irrespective of the pumping method. For currents of about $3 I_{th}$, shorter wavelength modes appear, making up to 10% of the contribution to the total intensity of the radiation. As the pump current increases from $3 I_{th}$ to $5 I_{th}$, the intensity of the short-wavelength modes increases more strongly than the intensity of the previously observed mode, and for $I > 3.5 I_{th}$ the intensity of the previously predominating mode is less than the sum of the intensities of all other modes. The regime is no longer a single-mode regime.

As the current increased, just as in previous work,[1–7] we observed a smooth shift of the lasing wavelength into the short- and long-wavelength regions of the spectrum (Fig. 3). For low currents ($I < 1.8 I_{th}$) the radiation wavelength shifted in the direction of larger values by approximating 10 Å . As

the current increased further, the mode shifted smoothly into the short-wavelength region. For currents near $3.5 I_{th}$, the change in wavelength with current slows down, and the spectrum is no longer a single-mode spectrum. The total short-wavelength shift of the initial radiation mode in the one-mode regime in the current range $(1.8 – 3.5) I_{th}$ was 42 Å, i.e., 40% greater than in Ref. 4. In the current range $(3.5 – 4.5) I_{th}$ this mode shifted by another 8 Å . The total shift of the mode was 50 Å . In this series of samples the shift into the short-wavelength region of the spectrum occurred within the entire intermode spacing. Measurements of the radiation spectra uisng various methods to power the laser did not show any differences in character and magnitude of the change in the radiation wavelength with current. This shows that the crystal lattice of the active-region material is not heated when the laser structure is powered by different methods.

In summary, the experimental results obtained indicate that the substantial short-wavelength tuning of the lasing wavelength is due to not heating but rather radiation generation processes.

4. The initial increase in the radiation wavelength with current increasing to $1.8 I_{th}$ has already been attributed[1,6,7] to self-focusing of the radiation with uniform injection. For currents near $1.8 I_{th}$ the differential resistance of the *p–n* junc-

tion in the investigated lasers becomes less than the substrate resistance. For this reason, the substrate starts to affect the spread of the current over the width of the stripe. Since the width of the substrate is much greater than that of the stripe, the current density at the edges of the stripe becomes greater than at the center of the stripe. This difference increases with the current, resulting in a decrease of the permittivity and, correspondingly, a decrease of the radiation wavelength. It should be noted that this effect has a stronger influence on the radiation wavelength than self-focusing, i.e., nonuniform injection from the substrate results in a much larger increase in the nonequilibrium charge-carrier density at the stripe edges than the absence of laser radiation here.

The density of the nonequilibrium charge carriers is controlled by their lifetime, which is 10^{-9}–10^{-8} s, much shorter than the durations of the pump pulses employed. For this reason, the current-dependence of the radiation wavelength was the same with different forms of pumping.

In summary, a shift of the radiation wavelength by 50 Å in the short-wavelength direction was obtained on InAsSb/InAsSbP double heterostructures. Analysis of the lasing spectra and the shifts of the mode positions in a wide current range with various methods of pumping the nonequilibrium charge carriers showed that the pumping method does not influence the character of the shift of the radiation line. The short-wavelength shift is due not to the heating of the crystal lattice of the active-region material but rather to the nonuniform distribution of the nonequilibrium charge-carrier density over the width of the stripe.

[1] T. N. Danilova, O. I. Evseenko, A. N. Imenkov, N. M. Kolchanova, M. V. Stepanov, V. V. Sherstnev, and Yu. P. Yakovlev, Pis'ma Zh. Tekh. Fiz. **22**(7) (1966) [Sov. Tech. Phys. Lett. **22**, 645 (1966)].

[2] T. N. Danilova, O. I. Evseenko, A. N. Imenkov, N. M. Kolchanova, M. V. Stepanov, V. V. Sherstnev, and Yu. P. Yakovlev, Fiz. Tekh. Poluprovodn. **31**, 662 (1997) [Semiconductors **31**, 563 (1997)].

[3] T. N. Danilova, A. P. Danilova, E. G. Ershov, A. N. Imenkov, N. M. Kolchanova, M. V. Stepanov, V. V. Sherstnev, and Yu. P. Yakovlev, Fiz. Tekh. Poluprovodn. **31**, 976 (1997) [Semiconductors **31**, 831 (1997)].

[4] T. N. Danilova, A. P. Danilova, O. G. Ershov, A. N. Imenkov, V. V. Sherstnev, and Yu. P. Yakovlev, Fiz. Tekh. Poluprovodn. **32**, 373 (1998) [Semiconductors **32**, 339 (1998)].

[5] T. N. Danilova, A. P. Danilova, O. G. Ershov, A. N. Imenkov, V. V. Sherstnev, and Yu. P. Yakovlev, Fiz. Tekh. Poluprovodn. **32**, 373 (1998) [Semiconductors **32**, 339 (1998)].

[6] T. N. Danilova, O. I. Evseenko, A. N. Imenkov, N. M. Kolchanova, M. V. Stepanov, V. V. Sherstnev, and Yu. P. Yakovlev, Pis'ma Zh. Tekh. Fiz. **24**(6), 77 (1998) [Tech. Phys. Lett. **24**, 239 (1998)].

[7] T. N. Danilova, A. P. Danilova, A. N. Imenkov, N. M. Kolchanova, M. V. Stepanov, V. V. Sherstnev, and Yu. P. Yakovlev, Fiz. Tekh. Poluprovodn. (1999), in press.

Translated by M. E. Alferieff

The effect of internal reflections of the field on the parameters of a superradiant pulse

Yu. A. Avetisyan

Institute of Precision Mechanics and Control, Russian Academy of Sciences, Saratov
(Submitted February 24, 1999)
Pis'ma Zh. Tekh. Fiz. **25**, 24–31 (October 12, 1999)

Superadiation (SR) of an inverted two-level medium, described by one-dimensional Maxwell–Bloch equations without assuming that the amplitudes of the electric field vary smoothly along the sample, is studied. It is shown that as the initial inversion density increases, a transition is observed from the so-called ''lethargic'' field amplification regime, characteristic for the initial stage of SR, to a regime close to the ordinary exponential law. This accelerates the process and can lead to synchronization of counterpropagating SR pulses. Estimates are obtained for the average value of the delays of the oppositely propagating pulses and for their correlation criterion, which depends strongly on the ratio of the sample length and the half-wavelength of the resonance radiation. The possibility of realizing SR under conditions of strong phase relaxation of the active medium is discussed. © *1999 American Institute of Physics.* [S1063-7850(99)00510-8]

Spontaneous cooperative radiation or superradiance (SR) is of interest as a mechanism for generating short pulses of coherent radiation with peak intensity proportional to the squared density of inverted centers (atoms) N_0.

One aspect of SR for large values of N_0 has been examined in detail previously: the appearance of synchronization of oppositely propagating pulses emitted from the opposite ends of an inverted region (sample) of elongated form. This effect, observed, for example, experimentally in Ref. 1, has been investigated theoretically in Ref. 2, based on the linear approximation, which is applicable in the initial stage of the process. In Refs. 3 and 4 one-dimensional models of SR were studied with the electric field initially split into oppositely propagating waves, for which the approximation of smoothly varying amplitudes (SVAA) was used and nonresonance reflection coefficients were introduced phenomenologically.

However, a strict description of reasonance reflection from the sample boundaries can be obtained only by solving the Maxwell–Bloch equations without using the SVAA.[5] In so doing, we automatically take into account the secondary effect of $\lambda/2$ modulation of inversion (λ is the wavelength of the resonance radiation), arising because of the formation of standing waves in the sample,[6,7] In Ref. 8, which is based on such an approach, the following features were noted.

1. The correlation coefficients of the delays of the oppositely propagating pulses depend strongly on the ratio of the sample length L and $\lambda/2$ (the correlation is maximum for L an odd multiple of $\lambda/4$, and the correlation is essentially zero for L an even multiple of $\lambda/2$).

2. The observed acceleration of the process (the average delay time is proportional to the logarithm of the number of initially inverted atoms ($\ln N$) and not ($\ln N)^2$, as happened in the ordinary approach neglecting reflections).

However, the range of applicability of these results (obtained by a numerical method for comparatively short samples with $L \sim 4 - 22\lambda$) and their physical essence re-

mained largely unexplained. We note that these features were not reported in the simplified models.[2–4]

In the present letter, using numerical and approximate analytic solutions of the Maxwell–Bloch equations (without the SVAA), the physical meaning is determined and the previously obtained results are corrected with respect to synchronization of the oppositely propagating SR pulses. The accelerated pulse development due to reflections and the prospects of using it to obtain SR are discussed when the phase relaxation of the active medium is substantial.

We shall consider an extended, pencil-shaped sample (the cross-sectional area is $S_\perp$, the length $L > \sqrt{S_\perp} > \lambda$), consisting of N two-level atoms. Just as in Refs. 5–8, we employ the semiclassical Maxwell–Bloch equations for the slowly varying (over the period of oscillations of the field $\sim 1/\omega_0$, where ω_0 is the frequency of an optical transition of the atoms) complex amplitudes of the electric field $E(x,t)$ and the off-diagonal density matrix element of the atoms $P(x,t)$

$$\left(\frac{\partial^2}{\partial x^2} + k_0^2 \right) E(x,t) = -4\pi = k_0^2 d N_0 P(x,t),$$

$$\frac{\partial P(x,t)}{\partial t} = -\gamma P(x,t) + \frac{id}{\hbar} E(x,t) Z(x,t), \qquad (1)$$

as well as the population difference (inversion) $Z(x,t)$

$$\frac{\partial Z(x,t)}{\partial t} = -\frac{id}{2\hbar} E(x,t) P^*(x,t) + c.c. \qquad (2)$$

Here $k_0 = \omega_0/c = 2\pi/\lambda$ is the resonant wave number, c is the speed of light, d and $N_0 = N/(S_\perp L)$ are, respectively, the transient dipole moment and density of the atoms, γ is the phase relaxation constant, and $\hbar$ is Planck's constant. The equations (1) and (2) correspond to the one-dimensional approximation (suitable for Fresnel member $F = S_\perp/(\lambda L) \sim 1$; see Refs. 9–11) and ignoring of the delay in the slowly vary-
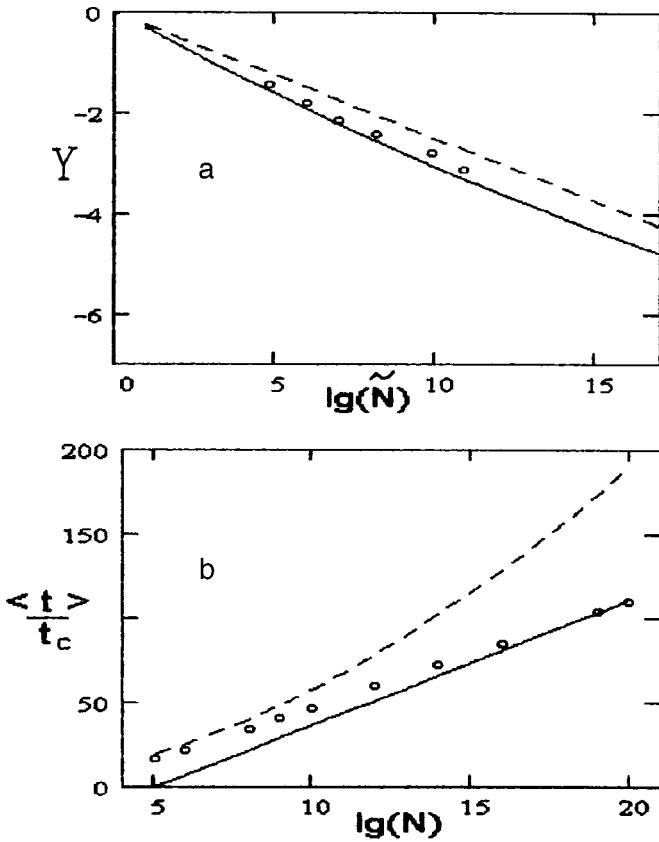
FIG. 1. Criterion for synchronization of oppositely propagating SR pulses (a) and dependence of the average delay time $\langle t \rangle$ on the number of atoms N for a sample of length $L = 100.25\lambda$ (b).

ing amplitudes (which is valid if the transit time L/c of light through the sample is shorter than the characteristic time scale of the pulse $t_c = \hbar / [2\pi d^2 N_0 k_0 L]$; see Refs. 6 and 8–11). Here we do not use the SVAA.

Equations (1) and (2) were solved numerically using a tested[6-8] computational algorithm that ensures continuity of the field and its spatial derivative at the ends of the sample ($x = \pm L/2$). Taking as the initial conditions total inversion $Z(x,0) = 1$ and stochastic polarization, an ensemble of realizations of the SR pulse and the correlation coefficient K_t of the delay times of the left-hand t_L and right-hand t_R pulses (i.e., the moments of the maxima of the radiation intensity at the left-hand $[E(-L/2, t)]^2$ and right-hand $[E(L/2, t)]^2$ ends of the sample, respectively; see Ref. 8) were calculated.

The criterion for synchronization of the oppositely propagating pulses was determined as follows. For each value of L considered, a series of calculations was performed for various values of N and the number of atoms $\tilde{N}(L)$ for which the correlation coefficient for the delays was close to 0.5 was found: $|K_t - 0.5| < \sigma$, where σ was chosen to be small (0.05–0.1). This definition using the $K_t = 0.5$ level (where the slope of the curve of K_t versus N is large; see Ref. 8) decreases the effect of computational errors.

The computational results for the corresponding values of $\tilde{N}$ for samples of length $L/\lambda = 4.25, 10.25, 21.75, 42.25, 100.25,$ and 220.25 in the absence of phase relaxation ($\gamma = 0$) are shown in Fig. 1a (circles) in the form of a curve of

$\log[1/(2k_0 L)]$ versus $\log \tilde{N}$. The solid curve in the same figure shows a plot of $\log \delta$ versus $\log \tilde{N}$ taken from Ref. 4; here δ is the threshold value of the phenomenological reflection coefficient for the field for which synchronization of the oppositely propagating SR pulses appears for a given number of atoms $\tilde{N}$. Therefore one can see that taking account of resonance reflection of the field from the ends of the sample strictly and the approximate approach give close results if the phenomenological reflection coefficient δ is chosen from the condition $\delta = (2k_0 L)^{-1}$. We also note that both dependences can be fit by a straight line with slope $-1/4$ (dashed line in Fig. 1a).

Figure 1b shows the average delay time $\langle t \rangle$ versus the number of atoms N calculated for a sample with $L/\lambda = 100.25$ and $\gamma = 0$ (circles). It is evident that the dependence of $\langle t \rangle$ on $\log N$ is indeed close to linear and not quadratic. We shall discuss below the equations for the dashed curve and the straight line.

To clarify the physical essence of the features noted above, we analyzed the solution, obtained using a Laplace transform in the time variable t, of the corresponding linearized problem (describing the initial stage of the process) when we can set $Z(x,t) = 1$:

$$E(-L/2, t) \approx \exp(-\gamma t) \sum_{n=1}^{\infty} E^{(2n)}(t),$$

$$E(L/2, t) \approx \exp(-\gamma t) \sum_{n=1}^{\infty} E^{(2n-1)}(t), \tag{3}$$

$$E^{(n)}(t) \approx \frac{A}{\sqrt{\pi n N}} \left[\frac{i\exp(-ik_0 L)}{2k_0 L} \right]^{n-1} \left[\frac{\tau}{n} \right]^{\frac{n}{2} - \frac{5}{4}}$$
$$\times \exp(2\sqrt{n\tau}), \quad n = 1,2,3,\ldots . \tag{4}$$

Here we have presented the result in the most interesting region $\tau \equiv t/t_c \gg 1$ and, just as in Ref. 4, for simplicity we gave the initial polarizability in the form of a wave with amplitude $2/\sqrt{N}$ propagating with wave number k_0 from left to right along the sample, $A \equiv \hbar / [i d t_c \exp(ik_0 L)]$. To avoid misunderstandings we recall that the relations (3) and (4) were obtained by ignoring the delay in the slowly varying amplitudes and are suitable for finding $E^{(n)}(t)$ provided that $t \gg nL/c$.

It follows from Eqs. (3) and (4) that in the approximations adopted the presence of phase relaxation γ reduces to simple multiplication of the corresponding solution in the absence of phase relaxation ($\gamma = 0$) by the factor $\exp(-\gamma t)$.

The quantity $E^{(1)}(t)$ agrees with the results obtained previously on the basis of the SVAA neglecting reflections, i.e., it corresponds to the single-pass field amplification regime.[4,9] The amplitudes $E^{(m)}(t)$ correspond to the field formed in m passes through the sample (due to the appropriate number of reflections from the ends of the sample). For a sample length $L/\lambda = n/2 + 1/4$, the next terms $E^{(m)}(t)$ and $E^{(m+2)}(t)$ in Eq. (3) have the same (opposite) signs. This means, correspondingly, that the sign of the complex ampli-

tude of the field is preserved (changes) after a pair of additional passes through the sample and two reflections from its ends.

It is also evident that the rate of growth of the amplitude $E^{(m)}(t)$, determined primarily by the exponential factor $\exp(2\sqrt{m\tau})$, increases with m. As a result, it turns out that the regime observed at the start of the process, the so-called ''lethargic'' intensification of the field ($E(L/2,t)$ $\sim \exp(2\sqrt{\tau})$ later goes over to a regime close to an ordinary exponential law $E(\pm L/2,t) \sim \exp(a\tau)$, where $a \sim 1/\ln(k_0 L)$. For a large number of atoms N, specifically, $N \gtrsim \tilde{N}$, where

$$\tilde{N} \sim (k_0 L)^b, \quad b \approx 4, \tag{5}$$

this leads to appreciable acceleration of the process. In the absence of phase relaxation ($\gamma = 0$), the average delay time can be estimated as

$$\langle t \rangle \approx \frac{t_c}{16}\left[\ln\left(\frac{\pi N}{8}\right)\right]^2 (1+\theta), \quad N < \tilde{N},$$

$$\langle t \rangle \sim t_c \left\{\frac{1}{2}\ln(k_0 L)\ln(N) - [\ln(k_0 L)]^2\right\}, \quad N > \tilde{N}, \tag{6}$$

where the correction is $\theta = 3(B - 3/2)^{-1}\ln(B)$ and $B = 0.5$ $[\ln(\pi N/8)]$. The dashed line and the solid straight line in Fig. 1b correspond to the upper and lower dependences in Eq. (6). Comparing with the results of numerical calculations (circles) shows that the estimate (6) is satisfactory.

The condition (5) gives at the same time an estimate for the number of atoms N leading to synchronization of the oppositely propagating SR pulses (for $N \gtrsim \tilde{N}$ and sample length L), i.e., it determines the synchronization criterion approximately.

We stress here the fundamental difference between our results and those obtained previously.[2-4] We recall that we obtained the criterion (5) for samples whose length assumes a discrete series of values: $L = (2m+1)\lambda/4$, where m is an integer. Analysis shows that for an approximate SVAAA description of Fresnel reflection of the field from the ends of a sample of arbitrary length, the phenomenological reflection coefficient must be chosen as $\delta = i/[2k_0 L \exp(ik_0 L)]$. The above-discussed change in sign of the complex amplitude of the field after a pair of additional passes through a sample of length $L = m\lambda/2$ is the reason why the delays of the oppositely propagating SR pulses are uncorrelated in this case. It is obviously important to take this circumstance into account in experiments, since for $N > \tilde{N}$ the results of observation of the synchronization of counterpropagating SR pulses could

turn out to be directly opposite if the lengths of the samples differ by $\lambda/4$ under otherwise equal conditions. It is also obvious that a change in the profile of the initial inversion (compared with the Π-shaped profile which we are considering) can strongly affect the results of such experiments.

In practice it is also important to use acceleration of the growth of an SR pulse as a result of field reflections. Under typical experimental conditions, when $k_0 L \gtrsim 10^5$, in view of the smallness of the equivalent reflection coefficient $\sim 1/(k_0 L)$, this decrease of the delay is comparatively small. However, this effect can be intensified by stimulating reflections of the field (for example, placing the active medium into a cavity; see Ref. 12). Our preliminary calculations showed that the parameters of the SR pulse in a cavity depend strongly on the modulus and phase of the reflection coefficient of the mirrors as well as on the ratio of the sample length and $\lambda/2$, which we plan to report in detail in an accompanying publication. It turns out that even small changes in the system length ($\Delta L \sim \lambda/10$) can radically change the efficiency of SR generation in a cavity: They can greatly decrease the delay and increase the peak intensity of a pulse. This makes it possible to use a cavity with optimal parameters to obtain SR, as proposed in Ref. 9, under conditions of strong phase relaxation of an active medium (when without the use of a cavity the SR pulse is virtually completely suppressed).

[1] A. Schiller, L. O. Schwan, and D. Schmid, J. Lumin. **38**, 23 (1987).

[2] M. Lewenstein and K. Rzazewski, Phys. Rev. A **26**, 1510 (1982).

[3] F. Haake, M. I. Kolobov, and H. Steudel, Opt. Commun. **92**, 385 (1992).

[4] E. N. Kaneva and E. D. Trifonov, Opt. Spectrosc. 79, 293 (1995) [Opt. Spectrosc. **79**, 270 (1995)].

[5] M. G. Benedict and E. D. Trifonov, Phys. Rev. A **38**, 2854 (1988).

[6] V. A. Malyshev, E. D. Trifonov, and L. O. Shvan, Opt. Spectrosk. **76**, 524 (1994) [Opt. Spectrosc. **76**, 470 (1994)].

[7] E. D. Trifonov, Opt. Spectrosk. **77**, 61 (1994) [Opt. Spectrosc. **77**, 51 (1994)].

[8] Yu. A. Avetisyan and E. D. Trifonov, Opt. Spectrosk. **82**, 357 (1997) [Opt. Spectrosc. **82**, 323 (1997)].

[9] V. V. Zheleznyakov, V. V. Kocharovskiĭ, and Vl. V. Kocharovskiĭ, Usp. Fiz. Nauk **159** (2), 193 (1989) [Sov. Phys. Usp. **32**, 835 (1989)].

[10] Yu. A. Avetisyan, A. I. Zaĭtsev, V. A. Malyshev, and E. D. Trifonov, Zh. Éksp. Teor. Fiz. **95**, 1541 (1989) [Sov. Phys. JETP **68**, 891 (1989)].

[11] Yu. A. Avetisyan, Opt. Spectrosk. **79**, 471 (1995) [Opt. Spectrosc. **79**, 435 (1995)].

[12] S. N. Andrianov, V. V. Eremenko, P. N. Zinoviev *et al.*, Laser Phys. **1**, 366 (1991).

Translated by M. E. Alferieff

Electronic energy spectrum of the sheath of an asymmetric low-pressure capacitive rf discharge

A. F. Aleksandrov, A. A. Rukhadze, V. P. Savinov, and I. F. Singaevskiĭ

M. V. Lomonosov Moscow State University
(Submitted September 4, 1999)
Pis'ma Zh. Tekh. Fiz. **25**, 32–39 (October 12, 1999)

The high-energy part of the electron energy spectrum of the plasma of an asymmetric capacitive low-pressure rf discharge in air associated with electron beams near the electrodes is studied experimentally. It is found that the energy distributions obtained under different conditions contain a beam peak, both quasimonoenergetic and substantially broadened in energy. It is established on the basis of quantitative estimates that the substantial damping of the electron beam is due to the excitation of collisionally dissipative and collisionless beam–plasma instabilities. © *1999 American Institute of Physics.* [S1063-7850(99)00610-2]

As is well known, electron beams with energies (in eV) of order the amplitude of the applied rf voltage $V_\sim$ arise near the electrodes in a capacitive low-pressure rf discharge.[1] These beams should enrich the electronic energy spectrum of the plasma with high-energy electrons and, if the appropriate conditions are satisfied, excite beam–plasma instabilities,[2] accompanied by the generation of microwave fields and additional heating of the plasma electrons.

The parameters and the role of electron beams and beam–plasma instabilities in the physical mechanism of an rf discharge, for all practical purposes, have not yet been investigated. It is obvious that electron beams and these instabilities can strongly influence the physical properties of the discharge under study.

The energy distribution of plasma electrons in the central regions of a low-pressure rf discharge have been determined experimentally.[3,4] In these works the probe method was used to determine the electron energy distribution function $f_e(\varepsilon)$ near 40 eV. The high-energy part of the energy distribution was not investigated satisfactorily, because the density of high-energy electrons is low and high probe voltages are inadmissible. The small enrichment of the ''tail'' of the distribution function $f_e(\varepsilon)$ by ''fast'' electrons was explained by the oscillation of the boundary of the cathode space-charge layer.[4] Previously, the electron energy spectrum of the sheath plasma of a capacitive rf discharge was investigated using a flat probe with variable orientation, and an electron beam with energies $\varepsilon_e > 180$ eV was detected.[5]

Exceptionally,[6–9] the high-energy parts of the energy distribution of electrons with energy $\varepsilon_e > 1$ keV in an rf discharge plasma have been detected with energy analyzers.

Our aim in the present work was to study experimentally the high-energy part of the electron energy spectrum of the sheath plasma of an asymmetric capacitive rf discharge and to search for manifestations of beam–plasma instabilities and their effect on the character of the electron energy distribution.

An rf discharge in air at pressures $p = 5 \times 10^{-2} - 5 \times 10^{-1}$ torr and field frequency $f = 1$ MHz was investigated. The diameter of the active electrode was $D_a = 0.58$ cm, the diameter of the grounded electrode was $D_g = 5.8$ cm, and the interelectrode distance was $d = 6$ cm. The use of an asymmetric rf discharge made it possible to increase the beam electron density n_{eb} from the active electrode by 1–2 orders of magnitude compared with the densities n_{eb} in an rf discharge with flat symmetric electrodes. The electron energy spectrum of the plasma was measured with a three-electrode energy analyzer, placed behind the grounded electrode, with a decelerating electrostatic field.

The general form of the electron energy spectrum (EES) of the plasma of the discharge investigated consisted of a narrow group of ''slow'' electrons with 1–1.5 orders of magnitude higher density than the density of the other parts of the electron energy distribution, a very wide (hundreds of eV) central part of the spectrum, and a group of the ''fastest'' electrons near the beam peak.

Typical quasistationary plasma electron distributions obtained are displayed in Fig. 1 for $V_\sim = 600$ and 750 V.

The character of the evolution of the electron energy spectrum of the plasma with a monotonic increase in the rf voltage is shown in Fig. 2. We note that the maximum electron beam energy $\varepsilon_{eb\,\mathrm{max}}$ observed in the distributions obtained is essentially the same as that predicted theoretically for an asymmetric rf discharge:[10] $\varepsilon_{eb\,\mathrm{max}} \approx 2\sqrt{2}\,V_\sim$ (eV), where $V_\sim$ is the effective applied rf voltage.

There is a fundamental difference between the energy distributions presented in Fig. 1. The electron distribution function for $V_\sim = 600$ V contains a quasimonoenergetic beam peak. Its half-width is about 30 eV. An energy variance close to this value occurs with electron emission from an electrode.[11] Thus, it can be assumed that in the present case an electron beam is scattered very weakly in collisions of beam electrons with neutral gas particles. The average mean free path of beam electrons is longer than the distance between the electrodes. However, the amplitude of the beam peak is several times greater than the amplitude of the central part of the energy spectrum.

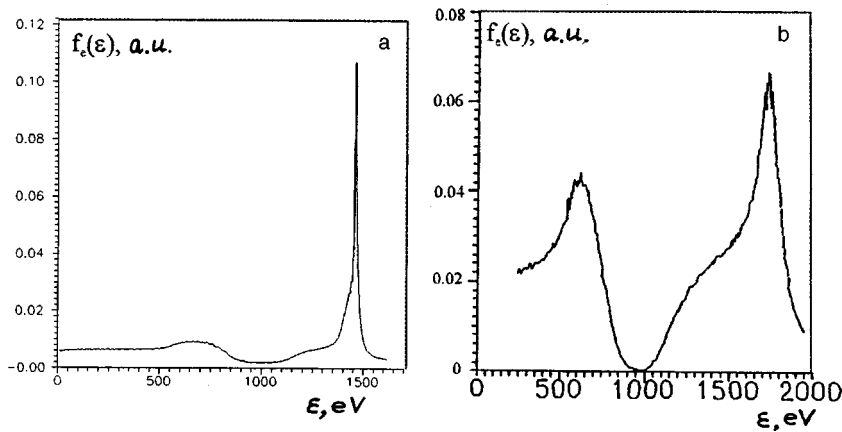In a discharge with $V_\sim = 750$ V the beam peak is already

FIG. 1. High-energy part of the electron energy distribution in the sheath in an rf discharge in air at pressure $p = 0.1$ torr with field frequency $f = 1$ MHz and rf voltage $V_\sim = 600$ V (a) and 750 V (b).

strongly broadened in energy: its half-width is more than an order of magnitude greater than the corresponding value at $V_\sim = 600$ V. Despite the expected decrease in the electron–neutral collision cross section with increasing beam-particle energy, the energy spread of the beam increased sharply. Here the amplitude of the beam peak is now comparable to the amplitudes of the secondary peaks in the central part of the energy distribution. This shows that a more efficient beam-scattering mechanism has appeared.

It is well known that the energy to which electrons emitted from an electrode are accelerated depends on the electron distribution over the emission phases and the form of the voltage in the sheath.[9,12] In principle, this should cause broadening of the observed quasistationary energy spectrum

of the near-electrode electron beams, as has been observed for rf voltages $V_\sim \ll 1$ kV under the conditions of potential ion–electron emission from electrodes.[5,13]

However, the results obtained in the present work show that when the voltage drop in the sheath is greater than 1 kV, electron energy spectra with quasimonoenergetic and with a substantially broadened peak near the maximum energies are observed in the sheath depending on the regime (Fig. 1a and 1c).

This experimental fact can be explained by a number of factors giving rise to narrowing of the beam peak of a quasistationary EES. In the first place, at definite phases of the rf field the voltage accelerating the ions in the layer is much greater than 1 kV. This gives rise to a transition from poten-
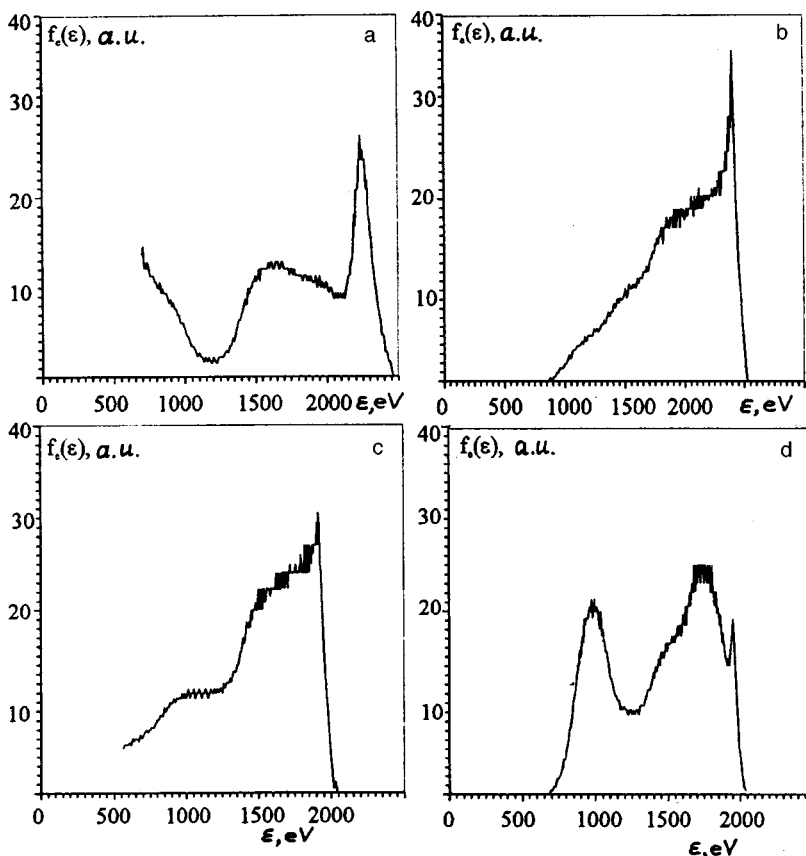

FIG. 2. High-energy part of the electron energy distribution in the sheath versus the rf voltage in an rf discharge in air at pressure $p = 0.07$ torr and field frequency $f = 1$ MHz: a — $V_\sim = 850$ V, b — 900 V, c — 950 V, and d — 1000 V.

tial to kinetic ion–electron emission with an appreciable increase in the surface ionization coefficient γ.[14] Second, since a relatively low rf frequency $f = \omega/2\pi = 1$ MHz ws used, the condition $\omega_{pi} > \omega$ (ω_{pi} is the ion plasma frequency) is satisfied in the experiment and the flux $J_i = n_i v_i$ of ions bombarding the electrode should increase in phases with maximum voltages in the sheath. Third, under the conditions investigated, the density of excited neutrals and the plasma radiation intensity increase in these phases; this increases the effective electron emission coefficient of an electrode, $\gamma_{\text{eff}} \gg \gamma$.[15] This factors increase the electron density in the beam in phases corresponding to the maximum energies acquired by them. As a fourth factor, it should be noted that low-energy electrons in corresponding phases of the field undergo stronger elastic scattering and it is more difficult for them to reach the energy analyzer. The tendency for the quasistationary EES to be enriched with maximum-energy electrons is also seen in the experimental results of Ref. 9 under conditions which are less favorable for this.

On this basis, the contribution of beam electrons to the investigated quasistationary ESS in phases with maximum accelerating voltages should be determining, leading to the formation of a quasimonoenergetic beam peak. In addition, as the rf voltage increases, the monokinetization of the high-energy part of the EES should increase.

The most likely explanation of the intensification beam scattering is development of beam–plasma instabilities: collisionally-dissipative Cherenkov instability with growth rate δ_1 and collisionless Cherenkov instability with growth rate δ_2. The corresponding expressions are[2]

$$\delta_1 = \omega_p \left(\frac{n_{eb}}{n_e} \frac{\omega_p}{\nu_e} \right)^{1/2} \quad \text{and} \quad \delta_2 = \omega_p \left(\frac{n_{eb}}{2 n_e} \right)^{1/3},$$

where ω_p is the electron plasma frequency and ν_e is the electron–neutrals elastic collision frequency.

We shall now assess the possibility of excitation of beam–plasma instabilities for the physical conditions corresponding to the distribution functions obtained (Fig. 1).

Under the investigated conditions the necessary (but not sufficient) condition for the existence of plasma waves was always satisfied:[2]

$$\omega_p > \nu_e.$$

Under the conditions of a discharge with $V_{\sim} = 600$ V we have $\omega_p \sim 10^9$ s^{-1} and $\nu_e \sim 10^8$ s^{-1}; according to data from our measurements,[16] here $n_{eb}/n_e \sim 10^{-2}$. Hence we obtain $\delta_1 > 3 \times 10^8$ s^{-1} and $\delta_2 > 2 \times 10^8$ s^{-1}. Therefore

$$\delta_1 \approx \delta_2 \approx \nu_e,$$

which means that the conditions for the development of both types of beam–plasma instabilities are unfavorable and corresponds to the unbroadened beam peak in Fig. 1a.

For a discharge with $V_{\sim} = 750$ V, we have correspondingly $\omega_p \lesssim 10^{10}$ s^{-1}, $n_{eb}/n_e \sim 10^{-2}$, $\nu_e \sim 10^8$ s^{-1}, $\delta_1 \sim 10^{10}$ s^{-1}, and $\delta_2 \sim 10^9$ s^{-1}. Therefore $\delta_1 \gg \nu_e$ and $\delta_2 > \nu_e$. Thus the collisionless Cherenkov instability should be efficiently excited, leading to substantial heating of the beam electrons,

i.e., a sharp decrease of the monoenergetic nature of the beam. The latter corresponds to the form of the distribution obtained (Fig. 1b).

Let us consider the evolution of the electronic energy spectrum with increasing $V_{\sim}$ in Fig. 2. This series of measurements was performed for higher values of $V_{\sim}$ and lower gas pressure ($p = 0.07$ torr) than under the conditions considered above.

As one can see from Fig. 2, as $V_{\sim}$ increases, the beam peak spreads in energy even more, and the ratio of the amplitude of the beam peak to the peak amplitudes of electrons from the central part of the distribution decreases monotonically to values less than 1.

Therefore, under the specified conditions with increasing $V_{\sim}$, as a result of collisionless Cherenkov instability the decay of the near-electrode electron beam increased monotonically and the behavior of the high-energy part of the distribution underwent changes substantially.

[1] V. L. Kovalevskiĭ and V. P. Savinov, Fiz. Plazmy **20**, 322 (1994) [Plasma Phys. Rep. **20**, 292 (1994)].

[2] A. F. Alexandrov, L. S. Bogdankevich, and A. A. Rukhadze, *The Principles of Plasma Electrodyamics* (Springer, New York, 1984; Vyssh. shkola, Moscow, 1984).

[3] G. Dilecce, M. Capitelli, and S. J. De Benedictis, J. J. Appl. Phys. **69**, 121 (1991).

[4] V. A. Godyak, R. B. Piejak, and B. M. Alexandrovich, Plasma Sources Sci. Technol. **1**, 36 (1992).

[5] A. A. Kuzovnikov and V. P. Savinov, in *Problems of the Physics of Low-Temperature Plasma*, edited by M. A. El'yashevich (Nauka i tekhnika, Minsk, 1970), pp. 162–165.

[6] H. R. Koenig and L. I. Maissel, IBM J. Res. Dev. **14**, 168 (1970).

[7] A. S. Smirnov, K. S. Frolov, and A. Yu. Ustavshchikov, in *Proceedings of the Conference on Low-Temperature Plasma Physics,* Petrozavodsk (1995), Part 2, pp. 178–180.

[8] A. F. Aleksandrov, V. L. Kovalevskiĭ, V. P. Savinov, and I. F. Singaevskiĭ, in *Abstracts of Reports at the 8th Conference on the Physics of Gas Discharges,* Ryazan' (1996), Part 2, pp. 48–89.

[9] K. E. Orlov and A. S. Smirnov, in *Proceedings of the Conference on Plasma Physics and Plasma Technology*, Minsk (1997), Vol. 1, p. 142.

[10] Yu. P. Raĭzer and M. N. Shneĭder, Fiz. Plazmy **18**(9), 1476 (1992).

[11] H. D. Hagstrum, Phys. Rev. **10**, 672 (1956).

[12] A. A. Kuzovnikov and V. P. Savinov, Vestn. Mosk. Univ., Ser. Fizika, Astronomiya, No. 2, 215 (1973).

[13] B. D. Medved and Y. E. Strausser, Advanc. Electron. Electron. Phys. **21**, 101 (1965).

[14] B. A. Brusilovskiĭ, *Kinetics of Ion-Electron Emission* (Énergoatomizdat, Moscow, 1990).

[15] A. S. Smirnov, A. Yu. Ustavshchikov, and K. S. Frolov, Zh. Tekh. Fiz. **65**(8), 38 (1995) [Tech. Phys. **40**, 768 (1995)].

[16] V. L. Kovalevskiĭ, V. P. Savinov, I. F. Singaevskiĭ, and V. G. Yakunin, in *Abstracts of Reports and the 9th Conference on the Physics of Gas Discharges,* Ryazan' (1998), Part 1, pp. 102–103.

Translated by M. E. Alferieff

Lasing characteristics of lasers with a vertical cavity based on In$_{0.2}$Ga$_{0.8}$As quantum wells

V. A. Gaĭsler, A. I. Toropov, A. K. Bakarov, A. K. Kalagin, N. T. Moshegov, D. A. Ténné, M. M. Kachanova, O. R. Kopp, L. A. Nenasheva, and A. S. Medvedev

Institute of Semiconductor Physics, Siberian Branch of the Russian Academy of Sciences, Novosibirsk
(Submitted May 12, 1999)
Pis'ma Zh. Tekh. Fiz. **25**, 40–44 (October 12, 1999)

Semiconductor lasers with a vertical cavity with a high external quantum efficiency and high radiation power have been developed and constructed. Powers up to 10 W at $T = 300$ K and 20 W at $T = 250$ K have been obtained for 500 μm aperture lasers operating in the pulsed regime. © *1999 American Institute of Physics.* [S1063-7850(99)00710-7]

In the last few years, progress in the development of semiconductor lasers has largely been determined by the development and construction of lasers with a vertical cavity (LVC). The record results for the threshold current, current-modulation frequency, and radiation divergence obtained for LVCs[1–5] substantially expand our understanding of the possibilities of semiconductor emitters and stimulate further investigations in this field. In the present letter we report the results of an investigation of the lasing characteristics of LVCs, whose structure has been optimized in order to achieve high external quantum efficiency and high radiation powers.

The initial laser structures were grown by molecular-beam epitaxy on n^+ (001) GaAs substrates. The laser structures contain undoped active regions of width λ, which include three 8-nm In$_{0.2}$Ga$_{0.8}$As quantum wells and mirror regions with p- and n-type doping, forming a Fabry–Perot interferometer and consisting of multiply repeated GaAs and Al$_{0.9}$Ga$_{0.1}$As $\lambda/4$ layers (20 and 22.5 periods for the p and n mirrors, respectively). Carrier injection into the action region is done through the p and n mirrors. The GaAs and Al$_{0.9}$Ga$_{0.1}$As layers of the mirrors were doped to 1×10^{18} cm^{-3}. To decrease the ohmic resistance of the mirror regions, the GaAs–Al$_{0.9}$Ga$_{0.1}$As interfaces contain 15-nm in-serts with an Al composition gradient and high degree of doping (Be or Si: 5×10^{18} cm^{-3}). The top p mirror is terminated with an additional 47-nm heavily doped (Be: 1×10^{19} cm^{-3}) GaAs layer, which functions as the contact region and ensures phase matching of the light reflected from the Ti (2 nm)/Au (120 nm) metallic coating and the semiconductor heteroboundaries. The layout of the LVC is displayed in Fig. 1a. The aperture (A) of the LVC is determined by the inner diameter of a Al$_x$O$_y$ ring, obtained by selective oxidation of the AlAs layers.[6] For this purpose, a 66-nm AlAs layer, located near the active region, is provided. The parameter A was varied over a wide range from 2 to 1000 μm. The radiation of the LVC is extracted through a GaAs substrate with an antireflection coating.

Figure 1b shows the reflection (R) spectra of the laser structure, the electroluminescence spectrum (E), and the emission spectrum (G) of the LVC. The measured reflection spectrum (thick line) agrees well with the calculated spectrum (fine line) and contains a resonance of the Fabry–Perot interferometer near 965 nm, whose position is the same as that of the maximum of the electroluminescence spectrum. The lasing wavelength of the LVC corresponds to the position of the resonance of the interferometer.

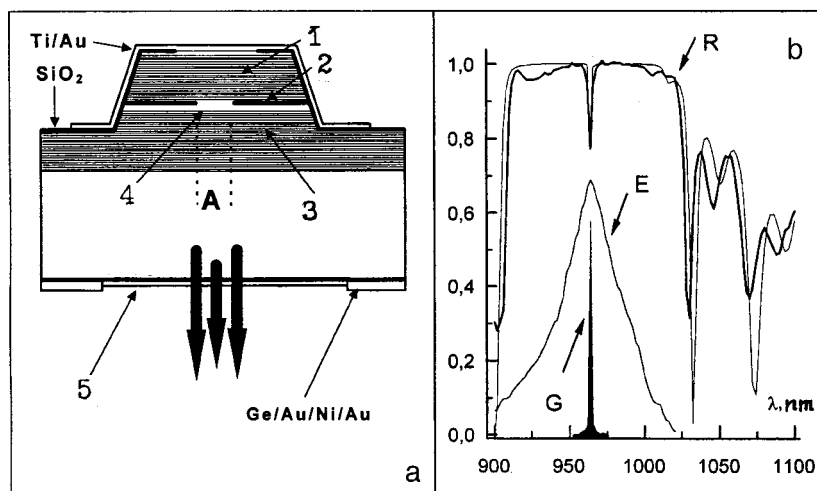The high external differential quantum efficiency η_e of

FIG. 1. a — Diagram of a vertical-cavity laser: *1* — *p* mirror, *2* — Al$_x$O$_y$ ring, *3* — *n* mirror, *4* — *n*-GaAs active region, *5* — antireflection coating. b — Reflection, electroluminescence, and lasing spectra of the LVC.
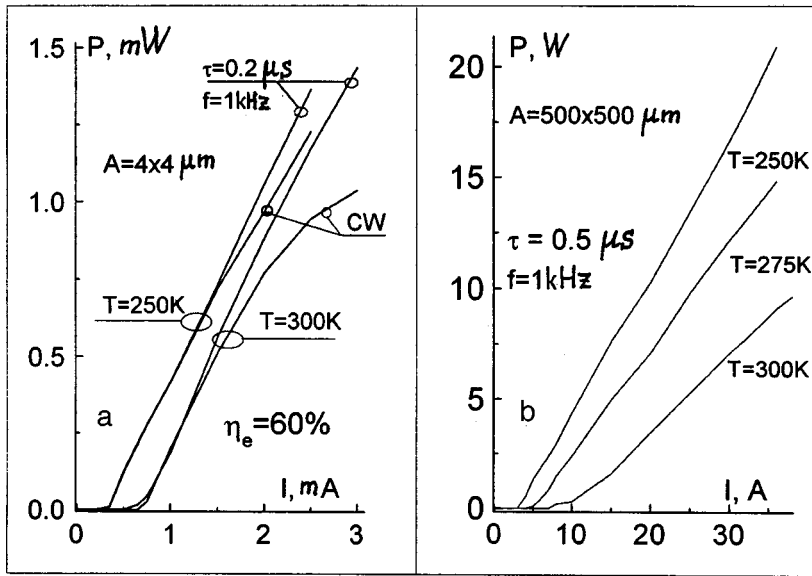
FIG. 2. Power–current characteristics of vertical-cavity lasers: a — for a laser with $A = 4$ μm, b — for a laser with $A = 500$ μm.

the LVC which we developed results from the high internal quantum efficiency $\eta_i > 0.9$ and the optimal ratio of the reflection coefficients of the mirrors: the top mirror is characterized by a very high value of the reflection coefficient R_t, close to 1, and the bottom (exit) window is characterized by a relatively low coefficient $R_b = 0.99$.

When R_t is close to 1 and the inequality $(1 - R_t) \ll (1 - R_b)$ is satisfied, the parameter η_e of the LVC is given by the expression[7]

$$\eta_e = \eta_i (1 - R_b)(\alpha L + 1 - R_b)^{-1}, \qquad (1)$$

where αL describes the optical losses in the cavity, α is the absorption coefficient, and L is the cavity length. In accordance with Eq. (1), for η_i close to 1 and $R_b = 0.99$ a value $\eta_e > 80\%$ can be attained. The reflection coefficient of the exit mirror $R_b = 0.99$, from our standpoint, is optimal for achieving high η_e, since a further decrease of R_b increases the threshold value of the gain to a level unattainable in practice.

In our structures the reflection coefficients of the mirrors are close to the indicated optimum: the calculated reflection coefficient is $R_t = 0.9999$ for the top mirror (neglecting absorption on the free carriers) and $R_t = 0.9916$ for the bottom (exit) mirror.

We obtained the maximum external differential quantum efficiency η_e at the 60% level for an LVC with $A = 4$ μm. The current–power characteristics of this laser are displayed in Fig. 2a. The decrease of the experimentally achieved value of η_e compared with the 80% level noted above is due to absorption of about 20% of the radiation in the 350 μm n-GaAs substrate.

Figure 2b shows the current–power characteristics for a laser with a large aperture $A = 500$ μm, for which a record high output power was obtained for the LVC (up to 10 W at $T = 300$ K and 20 W for $T = 250$ K, pulsed regime).

The radiation from all the LVCs we investigated is characterized by a narrow directional pattern. For LVC with aperture $A = 3$ μm, the divergence of the laser radiation at the half-power level (the half-width at half-height) is $\Gamma = 4.7°$,

and for a larger-aperture LVC this parameter does not exceed $3°$. It is interesting that the radiation of large-aperture lasers operating in a high-power mode is also characterized by a narrow directional pattern. Figure 3 shows the angular distribution of the power of the LVC with $A = 500$ μm with output power $P = 5$ W; the divergence of the radiation is $\Gamma = 2.75°$.

In summary, the experimental results presented in this letter demonstrate the possibility of building an LVC with high external quantum efficiency and high radiation power. This opens up new prospects for applications of lasers of this type.
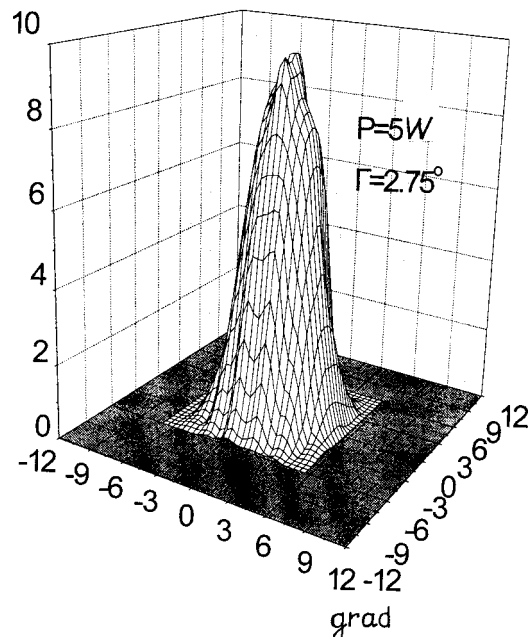

FIG. 3. Angular distribution of the power of an LVC with $A = 500$ μm.

[1] D. L. Huffaker, L. A. Graham, and H. Deng, IEEE Photonics Technol. Lett. **8**, 974 (1996).

[2] D. L. Huffaker and D. G. Deppe, Appl. Phys. Lett. **71**, 1449 (1997).

[3] B. J. Thibeault, K. Bertilsson, and E. R. Hegblom, IEEE Photonics Technol. Lett. **9**, 11 (1997).

[4] M. Grabherr, M. Miller, R. Jager, and K. J. Ebeling, Electron. Lett. **34**, 1227 (1998).

[5] R. A. Morgan, K. Kojima, and M. T. Asom, Electron. Lett. **29**, 206 (1993).

[6] G. M. Yang, D. H. Lim, J. H. Kim *et al.*, Jpn. J. Appl. Phys. **37**, 1391 (1998).

[7] R. S. Geels, S. W. Corzine, and L. A. Coldren, IEEE J. Quantum Electron. **27**, 1359 (1991).

Light scattering in water solutions of fullerene-containing polymers: Part 2. Effect of the molecular weight of the carrier polymer

M. L. Sushko, S. I. Klenin, M. A. Dumpis, L. I. Pozdnyakova, and L. B. Piotrovskiĭ

Institute of High-Molecular Compounds, Russian Academy of Sciences, St. Petersburg;
Institute of Experimental Medicine, Russian Academy of Medical Sciences, St. Petersburg
(Submitted June 8, 1999)
Pis'ma Zh. Tekh. Fiz. **25**, 45–49 (October 12, 1999)

The effect of the molecular mass M_{PVP} of linear polyvinylpyrrolidone macromolecules on the structures of domains formed in water solutions of PVP/fullerene (C_{60}) complexes is investigated. For constant C_{60} concentration in a complex, the values of M_{dom}, starting at $M_{PVP} = 20 \times 10^3$, increase as $M_{PVP}^{1.7}$, attesting to the formation of a fluctuation network whose nodes are C_{60} molecules. © *1999 American Institute of Physics.* [S1063-7850(99)00810-1]

In a previous publication[1] it was shown by the light-scattering method that in dilute solutions of complexes of polyvinylpyrrolidone (PVP) with fullerene (C_{60}) the concentration dependence of the reciprocal of the scattering intensity cH/I (where I is the excess scattering intensity, H is an optical constant, and c is the solution concentration) is nonlinear: up to the critical concentration $c_c = 1.45 \times 10^{-3}$ g/cm³ of the complex, the scattering intensity is independent of the concentration and satisfies $cH/I \to 0$ as $c \to 0$ or $M_w \to \infty$ as $c \to 0$, while for $c < c_c$ extrapolating cH/I to zero concentration gives a finite value of M_w, which, however, is two orders of magnitude greater than M_w of the PVP appearing in the complex. We interpreted the observed phenomenon as the presence in the solution of PVP/C_{60} complexes with a single ordered structure for $c > c_c$, which decays into domains with ordered structure for $c < c_c$ to which the extrapolated value of M_w pertains (which we denote below by M_{dom}). In Ref. 1 it was shown that M_{dom} depends strongly on the fullerene concentration in a complex: for the same molecular weight of the carrier polymer M_{dom} increases with the C_{60} concentration. To understand more clearly the structure of solutions of the complexes PVP/C_{60} and to determine the factors that stabilize long-range order in them, it is very important to investigate the role of the second component of the complex, specifically, the carrier polymer. Our objective in the present work is to investigate the effect of the molecular weight of the carrier polymer on the properties of solutions of the complexes PVP/C_{60}.

The PVP/C_{60} complexes were obtained by the method described in Ref. 2, which we modified. Specifically, benzene was used as the solvent of C_{60} instead of toluene; this makes it possible to separate the complex under less stringent conditions. As the carrier polymer we used PVP with the following molecular masses: *1* — 10000 (Sigma), *2* — 25000 (Merck), *3* — 35000, *4* — 40000 (Sigma). The molecular weights of PVP were determined independently by the light-scattering method and were found to be: *1* — 10000, *2* — 20000, *3* — 35000, *4* — 40000 with the usual error (10%) for this method. The fullerene content in the complexes, determined spectrophotometrically, was (0.78 ± 0.03)% for all samples.

Figure 1 displays cH/I versus the concentration of PVP/C_{60} complexes. As one can see from the figure, the concentration dependence of the reciprocal of the light-scattering intensity for different molecular weights of the carrier polymer is of the same character. Two sections can be distinguished on each curve: *1* — for $c > c_c$, where the scattering intensity is independent of the concentration ($CH/I \to 0$ as $c \to 0$ or $M_w \to \infty$ as $c \to 0$) and *2* — for $c < c_c$, where extrapolation to zero concentration gives a finite value of M_w, which pertains to domains with ordered structure. It should be emphasized that, just as in Ref. 1, the scattering asymmetry $z = I_{45}/I_{135}$ (where I_{45} and I_{135} are excess scattering intensities at angles 45 and 135°, respectively) in solutions of the complexes PVP/C_{60} is only negligibly greater than the scattering asymmetry of PVP and is 1.5–2.0. This shows that in solutions of the complexes PVP/C_{60} there is virtually no intramolecular interference of the light scattered by domains, as is characteristic for light
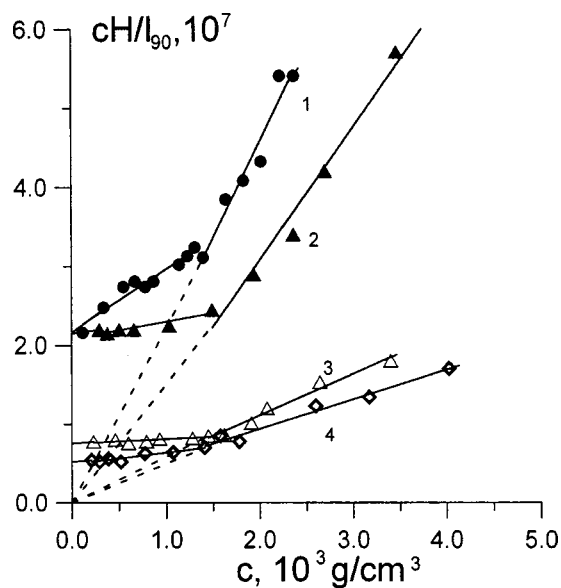

FIG. 1. $(cH/I)_{90}$ versus the concentration of water solutions of PVP/C_{60} molecules for various molecular weights of the carrier polymer: *1* — 10000, *2* — 20000, *3* — 35000, *4* — 40000.
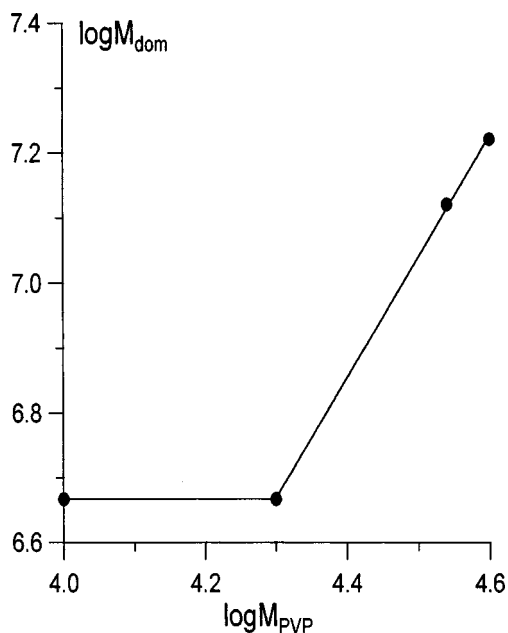
FIG. 2. Molecular weight of domains in water solutions of the complexes PVP/C_{60} versus the molecular weight of the carrier polymer.

TABLE I.

M_{PVP}, 10^{-3}	L, Å	M_{dom}, 10^{-6}
10	225	4.65
20	450	4.65
35	800	13.2
40	900	16.7

the fullerene molecules on average is $R_c = 450\text{--}550$ Å and does not depend on the total concentration of the complex PVP/C_{60} in solution or the molecular weight of PVP or the ratio of PVP and C_{60} in a complex. PVP plays a larger role for $c < c_c$, i.e., when a single ordered structure of the solution no longer can be preserved and the solution decomposes into large, very stable (second virial coefficient $A_2 \geq 0$) domains, where long-range ordering seems to be preserved. As one can see from Fig. 2, the molecular weight of domains does not depend on the molecular weight of the carrier polymer (M_{PVP}) for $M_{PVP} \leq 2 \times 10^4$ and a strong dependence $M_{dom} = (M_{PVP})^{1.56}$ is observed for $M_{PVP} > 2 \times 10^4$. To explain the experimental results we used the computed data. It is evident from Table I that the contour length L of PVP for $M_{PVP} > 2 \times 10^4$ is greater than R_c, i.e., formation of a fluctuation network is possible in principle, and this means that an additional type of interaction can appear—interaction between C_{60} as a constituent of one complex and PVP as a constituent of neighboring molecules—stabilizing the ordered structure of the solution. It is obvious that the larger L of the carrier polymer, the more stabilizing the action of the polymer is, i.e., the larger the domains are. Interactions of this form are not manifested (or only very weakly) in solutions of complexes on short chains of PVP, and the domain sizes do not depend on M_{PVP}, as is observed experimentally (Fig. 2).

In summary, the experimental data taken together attest to the presence of an ordered structure, which depends on the fullerene concentration, in the solutions of the complexes PVP/C_{60}. In addition, fullerene plays the main role in creating the long-range order, while the carrier polymer has an additional stabilizing effect if its molecular weight exceeds 2×10^4.

scattering by large molecules exceeding $\lambda/20$ in size (λ is the wavelength of the light), resulting in a lower scattering intensity of the solution at angle 135° than I_{45} (according to the theory of light scattering in solutions of large molecules $I_{\theta'} < I_\theta$ holds for all scattering angles $\theta' > \theta$). In turn, this unequivocally attests to the fact that the elementary oscillators (which the complexes PVP/C_{60} are) are located in domains at distances from one another comparable to the wavelength of the light. For this reason, the scattering asymmetry in solutions of the complexes PVP/C_{60} does not characterize the size (radius of inertia) of the domains, but it indicates the absence (or a very insignificant number) of intermolecular contacts of PVP/C_{60} complexes in the solution.

As already mentioned above, for $c > c_c$ it is observed that $I \sim \overline{(\Delta c)^2}$, where $\overline{(\Delta c)^2}$ is the mean-square fluctuation of the concentration, remains constant on dilution, i.e., in this concentration range the fluctuations in solutions are not independent, which attests to the formation of an ordered structure in solutions of the complexes PVP/C_{60}. Apparently, fullerene plays the main role in the creation of the long-range order, since in all investigated solutions of complexes with the same C_{60} content the concentration is essentially the same 1.45×10^{-3} g/cm³, i.e., the distance between

[1] S. I. Klenin, M. L. Sushko, M. A. Dumpis, L. I. Pozdnyakova, and L. B. Piotrovskiĭ, Zh. Tekh. Fiz. (1999) [Tech. Phys.], in press.
[2] Y. N. Yamakoshi, T. Yagami, L. Fukuhara *et al.*, J. Chem. Soc. Chem. Commun. 517 (1994).

Translated by M. E. Alferieff

Component composition and strain of barium–strontium titanate ferroelectric films

S. F. Karmanenko, A. I. Dedyk, N. N. Isakov, V. I. Sakharov, A. A. Semenov, I. T. Serenkov, and L. T. Ter-Martirosyan

Electricotechnical University, St. Petersburg;
A. F. Ioffe Physicotechnical Institute, Russian Academy of Sciences, St. Petersburg
(Submitted May 14, 1999)
Pis'ma Zh. Tekh. Fiz. **25**, 50–60 (October 12, 1999)

The effect of the ratios of the cationic components and internal strains on the critical temperature T_c and the dielectric characteristics of BSTO ferroelectric films grown on α-Al_2O_3 [$10\underline{1}2$] and $LaAlO_3$ substrates were investigated. Ion backscattering diagnostics revealed a barium deficiency in the surface layer of the films and showed that the films differ in structural quality. © *1999 American Institute of Physics.* [S1063-7850(99)00910-6]

Ferroelectric films (FEFs) are promising objects as a basis for radioelectronic devices, such as tunable band-pass filters, modulators, and delay lines[1,2] as well as devices in which the microwave signal velocity and phase can be controlled.[3,4] FEF-based devices have a number of advantages over their ferrite and semiconductor analogs—a higher rate of conversion of the microwave signal, higher phase regulation accuracy, smaller size, and lower cost.[3,4]

For applications of FEFs in the microwave range, the films must possess high permittivity ε and capacitance control coefficient $K = C(0)/C(U_{max})$ and a low dielectric loss angle tangent $\tan \delta$, and their capacitance–voltage characteristics (CVCs) must not show any hysteresis. This requires a material that undergoes a phase transition from the paraelectric into the ferroelectric state at a temperature somewhat below the operating temperature. In this variant spontaneous polarization still does not appear, but ε approaches its maximum value. The material best meeting these requirements is the solid solution $Ba_xSr_{1-x}TiO_3$ (BSTO). According to the phase diagram,[5] the BSTO composition with $x = 0.5$–0.7 must be chosen for operation at room temperature.

In the present work, we investigated the effect of the component content and strains in the structure of BSTO films, grown on leucosapphire (α–Al_2O_3 [$10\underline{1}2$]–α) and lanthanum aluminate ($LaAlO_3$—LAO)) substrates, on the CVC and the temperature dependence of the dielectric properties.

A URM 3.279 technological setup and a VCHD-2.5 rf generator operating at 13.56 MHz were used to grow the BSTO films. In the cathodic sputtering regime, the rf discharge power was ~ 500 W and the discharge current density was 3–5 mA/cm^2. A target (diameter ~ 125 mm) consisting of a powder of a ferroelectric material was placed on the cathode sputtering unit, lying below the substrate holder. The substrates were heated with a resistive heater in combination with the plasma of an rf glow discharge. The substrate temperature during deposition was regulated in the range 950–1100 K. The pressure of the argon + oxygen gas mixture was $p \sim 10$–20 Pa. The growth rate of the films was varied in the range 1.5–2 nm/min. The formation of a film in situ was concluded with prolonged heating of the samples in oxygen

gas. In addition, some BSTO films were annealed in oxygen at ~ 1200 K.

X-ray diffraction analysis (XDA) and medium-energy ion scattering (MEIS) were used to investigate the structure and composition of the films obtained.[6,7] Figure 1 shows the x-ray diffraction patterns of two films grown in a single technological process on LAO and α substrates. The textured BSTO films did not contain impurities of competing phases and showed only (k00) reflections. The position of the reflections indicates that the internal strains in the films are different.

It is well known that in the series of BSTO solid solutions the lattice constant varies linearly from 0.3905 ($x = 0$) to 0.4040 nm ($x = 1$).[8,9] The substrates used differ strongly with respect to their structure and physicochemical properties. Lanthanum aluminate possesses perovskite structure with lattice constant 0.535 nm at temperatures above 435 °C.[10] Rotation of the basal plane by 45° changes the effective lattice parameter of LAO to ~ 0.3800 nm. A transition from the cubic into the orthorhombic phase at the indicated temperature is accompanied by strong twinning, but the change in the lattice parameter a_0 is negligible.

The α substrate possesses hexagonal crystal structure, but in the [$1\underline{1}02$] cut a rhombus with an edge ~ 0.5140 nm forms at the surface of the plate.[11] This edge length can be compared with the lattice constant ~ 0.3670 nm for a rotation of the basal plane by 45°. Thus, for both substrate materials compression stresses are present in the BSTO films grown. The lattice mismatch parameter $\xi = 2(a_1 - a_2)/(a_1 + a_2)$, where a_1 and a_2 are the unit cell parameters of the substrate and film materials, for the compound $Ba_{0.6}Sr_{0.4}TiO_3$ ($a_2 \approx 0.3965$ nm) is $\xi(\alpha) \approx -7.7\%$ and $\xi(LAO) \approx -3.7\%$. The rhombic distortions on a leucosapphire surface increase the mismatch with the film of the perovskite compound. It is also necessary to take account of the thermal expansion coefficients of the materials (β) and their chemical activity at the interface. The coefficient β of the materials decreases in the following order: BSTO $\sim 9 \times 10^{-6}$ K^{-1}, $\alpha \sim 6 \times 10^{-6}$ K^{-1}, LAO $\sim 1.25 \times 10^{-6}$ K^{-1}. The BSTO/LAO structure is characterized by a strong
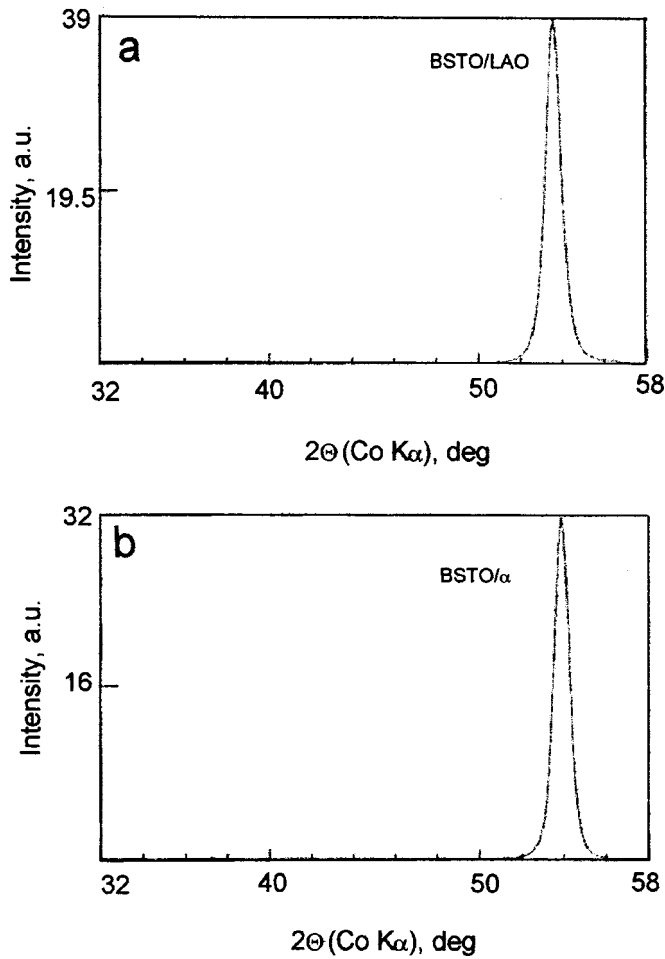
FIG. 1. X-Ray diffraction patterns of BSTO films ((200) reflections). a — $LaAlO_3$ substrate, b — α-Al_2O_3.

TABLE I. Characteristics of BSTO films.

Code/ substrate	1821/ LAO	1815/ α	2251/ LAO	2232/ α	2231/ α	0752/ LAO	0751/ α
Film thickness, nm	950	950	750	750	750	400	400
Annealing	+	+	+	+	−	−	−
Target composition x	0.50	0.50	0.55	0.55	0.55	0.60	0.60
Lattice constant, a_0, nm	0.3972	0.3948	0.3982	0.3960	0.3954	−	−
Relative minimum yield, $\chi(E)$, %	80	100	60	100	100	35	100
Temperature of the maximum ε, T_m, K	160	230	245	260	278	260	330
ε (300 K)	1874	2605	3245	2391	1545	2213	3147
$\tan\delta$ (300 K, 0 V)	0.010	0.004	0.005	0.002	0.011	0.002	0.005
K (300 K)	1.20	1.62	1.40	1.49	2.1	1.45	1.9

difference—more than a factor of 7—in the expansion coefficients compared with the BSTO/α structure, where the factor is 1.5. Therefore the capability of preserving strain in the BSTO/α structure is much higher, while the BSTO/LAO structure tends to form dimensional defects in the film. As a result of the high density of twinning boundaries on the LAO substrate and the large difference of the thermal coefficients, the mismatch stresses in the film find sinks in the planar boundaries, three-dimensional dislocations, and block boundaries. In BSTO films grown on α substrates, on account of the matching of the temperature coefficients, the conditions for preserving the structural strains inside crystallites are controlled better. In BSTO/LAO structures, even a change in the sign of the strain — from negative for small LAO film thicknesses to positive ($\Delta a_0 = a_{01} - a_{00} \approx 0.017$ nm see Table I) — is observed.

X-ray diffraction analysis of the films did not show any deviations in the orientation of the crystallites from the [100] direction or differences in the structural orientation of the films. At the same time, MEIS diagnostics[6,7] revealed differences in the structural perfection of the samples. We investigated the energy distributions of ions scattered by an angle Θ after the primary beam of H^+, He^+, or N^+ ions with initial energy 180–230 keV interacted with the surface. Either an electrostatic analyzer (ESA) with resolution $\Delta E/E$

$= 0.005$ and $\Theta = 120°$ or a semiconductor detector with $\Delta E = 4$ keV and $\Theta = 150°$ was used for analysis. Two orientations of the ion beam relative to the low-index direction in the crystal were used. The ion yield $Y_r(E)$ in an unoriented beam and the yield $Y_c(E)$ obtained with ion channeling along the [100] axis were measured. For these regimes, the energy spectra and the ratio $\chi(E) = Y_c(E)/Y_r(E)$, called the relative ion yield, whose minimum value for a surface layer characterized the perfection of the crystal lattice of the samples, were measured.

The investigations showed that in the initial stage of film growth on LAO substrates a highly oriented structure is formed, in which ion channeling appears. BSTO/LAO structures with film thickness ~ 300 nm possess the highest degree of orientation of the crystallites ($\chi \sim 30\%$). Figure 2a shows the MEIS spectrum of a ~ 400 nm thick 0752/LAO sample (see Table I), where the parameter $\chi \sim 35\%$. As the film thickness increased, the parameter χ increased monotonically, and $\chi \sim 60\%$ on a ~ 750 nm thick film (2251/LAO). For ~ 2000 nm thick BSTO/LAO films, ion channeling was completely absent in a ~ 400 nm surface layer.

Copper films with thickness ~ 0.5 μm, deposited on a BSTO surface in the process of magnetron sputtering, were used as electrodes. Planar capacitors were prepared, using photolithography and chemical etching, to measure the dielectric characteristics of the FEFs. An E7-12 meter at 1 MHz was used to measure the dielectric characteristics of the capacitors. The geometric dimensions of the planar capacitors were determined under a microscope: the gap width w was 7–15 μm and the length was $l = 100$–1000 μm. The measurements of the temperature dependence of the capacitance and $\tan\delta$ were performed in the range 77–400 K. A
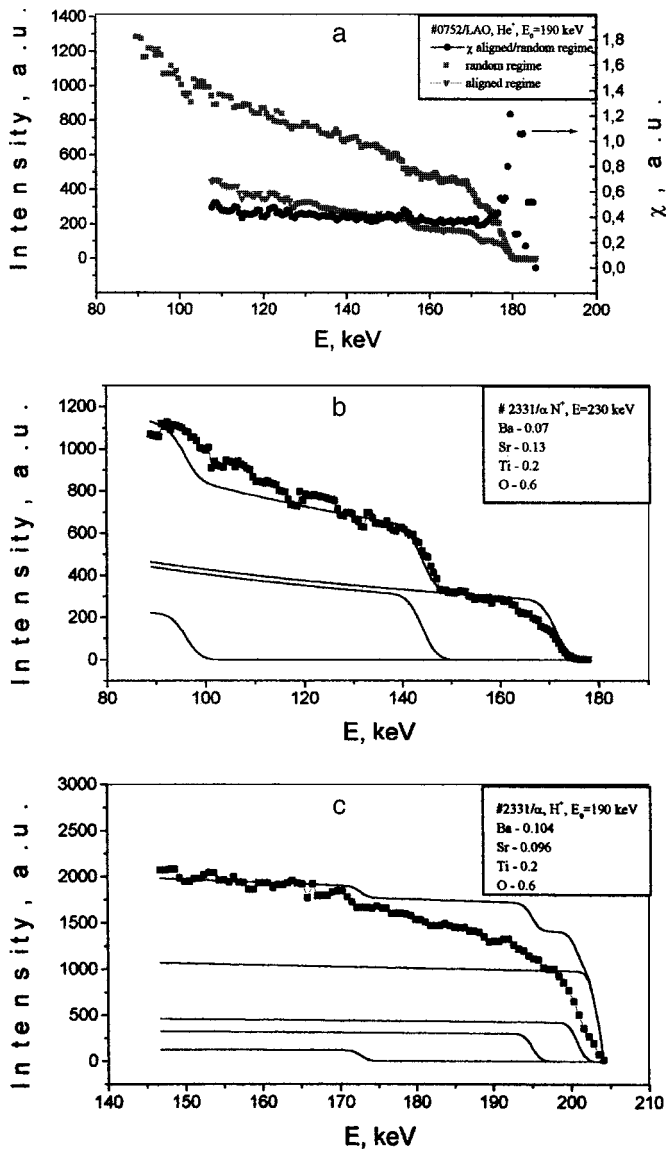
FIG. 2. MEIS spectra: a — Random, channeled measurement regime and relative ion yield (sample 0752), b — spectrum of sample 2231 in the random regime with irradiation with 230-keV N^+ ions, c — spectrum of sample 2231 with irradiation with 190-keV H^+ ions.

FIG. 3. Capacitance–voltage characteristic and tan δ versus the applied voltage for a planar capacitor.

bias voltage ranging from $+200$ to -200 V was applied to the capacitor. The relative resolution with respect to the capacitance and voltage was 5×10^{-3}, and tan δ was measured with accuracy 5×10^{-4}. The formula presented in Refs. 9 and 12 was used to calculate the permittivity. The characteristics of a number of the BSTO films investigated are given in Table I.

The ratio of the components on the surface of the films was determined on the basis of the MEIS spectra measured by irradiating a sample with ~ 230 keV N^+ ions. The formula ratio was determined to within ~ 10 at.%. The spectrum for the $2231/\alpha$ film (see Table I) is presented in Fig. 2b. It was established on the basis of the spectrum presented that the content of the components in a surface layer no more than 10 nm thick gives an optimal fit with the working model Ba:Sr:Ti:O$=0.07:0.13:0.20:0.60$, i.e., $x\approx 0.35$. Analysis of the MEIS spectra showed that the content of the components
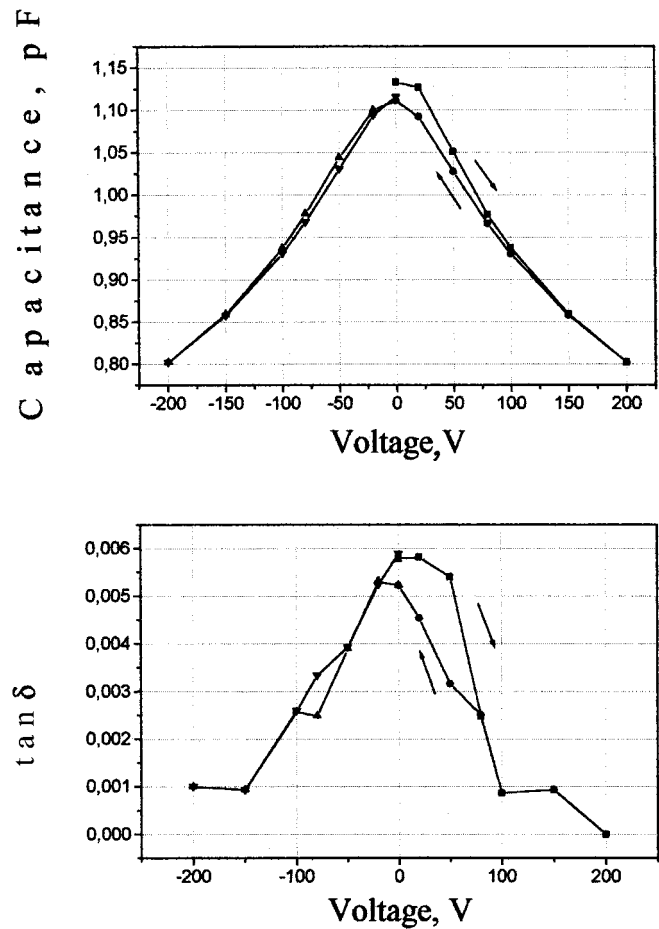
on the surface was different from that in the interior volume of the BSTO films. In the same $2231/\alpha$ sample the coefficient $x\approx 0.52$ in the interior of the film (~ 400 nm into the interior of the sample from the surface) was determined using H^+ ions (~ 190 keV) and reference samples. Figure 2c shows the MEIS spectrum of sample $2231/\alpha$, on the basis of which the composition in the volume of the sample was determined and found to correspond, on the whole, to the initial composition of the target (see Table I).

The fairly diffuse leading edge of the experimental MEIS spectra should be noted. This could attest to development of surface relief and variable content of the components in the surface layer. Thin films grown on smooth α substrates (relief height not more than 10 nm) were distinguished by good agreement between the computed and experimental spectra. As a result of the annealing of the films, the MEIS spectrum was "smeared" and the barium content decreased monotonically toward the surface compared with the unannealed samples. LAO substrates were distinguished by strong surface relief (~ 50 nm). However, the MEIS spectra of thin unannealed BSTO/LAO films did not differ much from the analogous spectra for BSTO/α structures.

Table I gives the temperature T_m corresponding to the critical temperature T_c of the transition from the paraelectric into the ferroelectric state. In the composition range considered ($x=0.5-0.6$), T_m varies from 160 K (1821/LAO) to

330 K ($0751/\alpha$). Annealing of BSTO/α films decreases T_m by 15–20 K. This effect is accompanied by an increase in the lattice parameter and is probably due to a decrease of the internal strains in the film.

Figure 3 shows as an example the CVC and tan δ versus the applied bias voltage U for a planar capacitor based on the sample 2251/LAO. The capacitor control coefficient K was determined from the measured CVCs, and its values are presented in Table I. On the whole, the dielectric characteristics achieved for the films in the present work completely satisfy the requirements of radioelectronics.

As conclusions of this work, we note the following results. The surface of the BSTO film is barium-deficient compared with the interior volume of the sample, as indicated by the MEIS spectra. Monotonic equalization of the surface and volume levels of Ba occurs in a ~ 50 nm thick layer. High-temperature annealing of the films decreases the barium content on the surface of BSTO films, which can be explained by the high volatility of BaO complexes. A similar decrease of the surface barium concentration has been observed in magnetron sputtering and deposition of YBaCuO films on a substrate subjected to intense action of glow-discharge plasma.[13]

Distinguishing the physical mechanisms affecting the value of T_m is a complicated research problem, requiring the use of combinations of diagnostic methods. Probably the following basic factors influence the parameter T_m in textured BSTO films: the ratio of the cationic components Ba/Sr (the value of x); the oxygen content (the concentration of oxygen vacancies in the perovskite structure); and the internal strains due to a mismatch of the film and substrate structures.

It was established that the value of T_m in films with the same composition but grown on different substrates can differ by tens of degrees. The lattice constant a_0 in the perovskite structure, and not the ratio Ba/Sr, has a stronger effect on the parameter T_m. Partial relaxation of internal strains in the BSTO/α films as a result of annealing in oxygen can change a_0 and T_m by 15–20 K. This effect was not observed on BSTO/LAO films, since sufficient conditions for creating strong strains (mismatch of the structure and difference of the thermal coefficients) are not produced in this structure.

In summary, when choosing the composition of the target in technological processes for growing BSTO films for applications in radioelectronic devices at room temperature, the internal strains must be taken into account and a corresponding correction must be made. For the α substrates, a target with $x \approx 0.55$ must be chosen, while LAO substrates require an approximate composition with $x \approx 0.60 - 0.65$.

[1] A. T. Findikoglu, Q. A. Jia, and I. H. Campbell, Appl. Phys. Lett. **66**, 3674 (1995).

[2] E. Carlson and S. Gevorgian, Electron. Lett. **33**, 145 (1997).

[3] O. G. Vendik, I. G. Mironenko, and L. T. Ter-Martirosyan, Microwaves RF **33**, 67 (1994).

[4] L. C. Sengupta and S. Sengupta, Ferroelectricity Newsletters, No. 1–4, 4 (1996).

[5] V. V. Lemanov, E. P. Smirnov, and E. A. Tarakanov, Fiz. Tverd. Tela (St. Petersburg) **37**, 2476 (1995) [Phys. Solid State **37**, 1356 (1995)].

[6] S. F. Karmanenko, M. V. Belousov, and V. Ju. Davydov, Supercond. Sci. Technol. **6**, 23 (1993).

[7] V. V. Afrosimov, R. N. Il'in, S. F. Karmanenko, V. I. Sakharov, I. T. Serenkov, A. A. Semenov, and D. V. Yanovskiǐ, Fiz. Tverd. Tela (St. Petersburg) **41**(4), 588 (1999) [Phys. Solid State **41**, 527 (1999)].

[8] O. G. Vendik, L. S. Il'inskiǐ, A. D. Smirnov, and G. S. Khizha, Zh. Tekh. Fiz. **54**, 772 (1984) [Sov. Phys. Tech. Phys. **29**, 455 (1984)].

[9] *Ferroelectric Materials in Microwave Technology*, edited by O. G. Vendik (Sov. Radio, Moscow, 1979).

[10] S. Geller and V. B. Bala, Acta Crystallogr. **9**, 1019 (1956).

[11] *Acoustic Crystals*, edited by M. P. Shaskol'skiǐ (Nauka, Moscow, 1982).

[12] A. I. Dedyk, S. F. Karmanenko, S. Leppavuori *et al.*, J. Phys. IV **8**, Pr9-217 (1998).

[13] S. F. Karmanenko, A. P. Mitrofanov, K. F. Nyakshev, and R. A. Chakalov, Zh. Tekh. Fiz. **65**(1), 64 (1995) [Tech. Phys. **40**, 34 (1995)].

Translated by M. E. Alferieff

Effect of dynamic surface tension on the growth rate of the Tonks–Frenkel instability

S. O. Shiryaeva and O. A. Grigor'ev

P. G. Demidov State University, Yaroslavl'

By means of a numerical analysis of the dispersion equation for capillary motions of a liquid
with a charged flat free surface subjected to relaxation of the surface tension, it is shown
that the growth rate of the instability of the free surface of the liquid decreases as the characteristic
relaxation time of the surface tension increases and the Tonks–Frenkel parameter decreases.
The instability itself occurs in a limited range of wave numbers whose width is also determined by
the value of the Tonks–Frenkel parameter. © *1999 American Institute of Physics.*
[S1063-7850(99)01010-1]

The dynamic surface tension effect (relaxation of the surface tension), occurring at the surface of many electrically conducting liquids because of the presence of an electric double layer with a finite formation time and manifested as a dependence of the surface tension on the characteristic time (frequency) of the external perturbation, is of great interest in connection with numerous applications in technology and engineering.[1–5]

Previous analysis[1–5] of the influence of surface tension relaxation on the realization of capillary motion of a liquid with a charged free surface is mainly qualitative, since it was performed using asymptotic and numerical methods oriented toward obtaining qualitative dependences. In the numerical analysis of mathematical models of physical phenomena, the degree of detail of the information obtained depends substantially on the method used to render the mathematical–physical expressions dimensionless before numerical calculations are performed. In the numerical analysis performed in Refs. 2–5, the frequency, growth rates, and damping decrements of capillary motions of the liquid were scaled either to the frequency of the wave motions of a charged free surface of an ideal liquid or the characteristic damping decrement of capillary waves. A dimensionless parameter depending additively on the capillary pressure and electric-field pressure on the free surface of the liquid and through them on the physical characteristics of the liquid (density, capillary constant, surface tension, viscosity, surface electric charge density, and wave number) was taken the variable argument of the desired complex frequencies of capillary and relaxation motions of the liquid. This made it difficult to determine in the numerical analysis[2–5] the specific dependences of the characteristics of the capillary motion of the liquid on quantities such as the wave number k and the Tonks–Frenkel parameter W characterizing the stability of a charged free surface of a liquid. In the present letter, purposefully rendering all expressions dimensionless, we shall investigate the question of the specific effect of the wave number k, the parameter W, and the characteristic relaxation time τ_0 of the surface tension on the growth rate of the Tonks–Frenkel instability.

We shall consider the problem of calculating the spectrum of capillary motions in an ideally conducting liquid of infinite depth, subjected to surface-tension relaxation, in the field of gravity **g** and an electrostatic field **E**, oriented in a direction normal to the free surface and inducing on the flat free surface of the liquid a surface charge uniformly distributed with surface density $\varkappa$. Let the liquid have density ρ, kinematic viscosity ν, and surface tension σ, which is a relaxational function of time[1]

$$\sigma(t) = \sigma_0 + \sigma_* \exp(-t/\tau_0), \quad \sigma_* = \sigma_\infty - \sigma_0, \tag{1}$$

σ_0 is the surface tension at zero frequency (i.e., the equilibrium surface of the liquid), σ_∞ is the surface tension at high frequencies ($\omega\tau \gg 1$), τ_0 is the characteristic relaxation time of the surface tension (the characteristic formation time of an electric double layer at the surface of the liquid), and ω is the complex frequency of capillary motions of the liquid.

Fourier transforming the expression (1) and substituting into the dispersion equation obtained for the capillary motions of a viscous liquid with a charged free surface[6] relatively easily by the standard methods of hydrodynamics[6–8] gives a dispersion equation for capillary motions of a liquid with a charged free surface, subjected to surface tension relaxation, in the dimensional form[2–5]

$$\left(\frac{\omega a^2}{\nu} + 2ik^2 a^2\right)^2 + 4k^4 a^4 \sqrt{1 - \frac{i\omega a^2}{\nu k^2 a^2}}$$

$$= \frac{ka^4}{\rho\nu^2}\left(g\rho + \left(\sigma_0 - \frac{i\omega\tau_0\sigma_*}{1-i\omega\tau_0}\right)k^2 - 4\pi\varkappa^2 k\right).$$

Introducing the dimensionless variables

$$x = ka, \quad a = \sqrt{\sigma_0/\rho g}, \quad y = \frac{\omega a^2}{\nu},$$

$$\tau = \frac{\tau_0\nu}{a^2}, \quad \beta = \frac{\sigma_0 a}{\rho\nu^2}, \quad \beta_0 = \frac{\sigma_*}{\sigma_0}, \quad W = \frac{4\pi\varkappa^2 a}{\sigma_0},$$
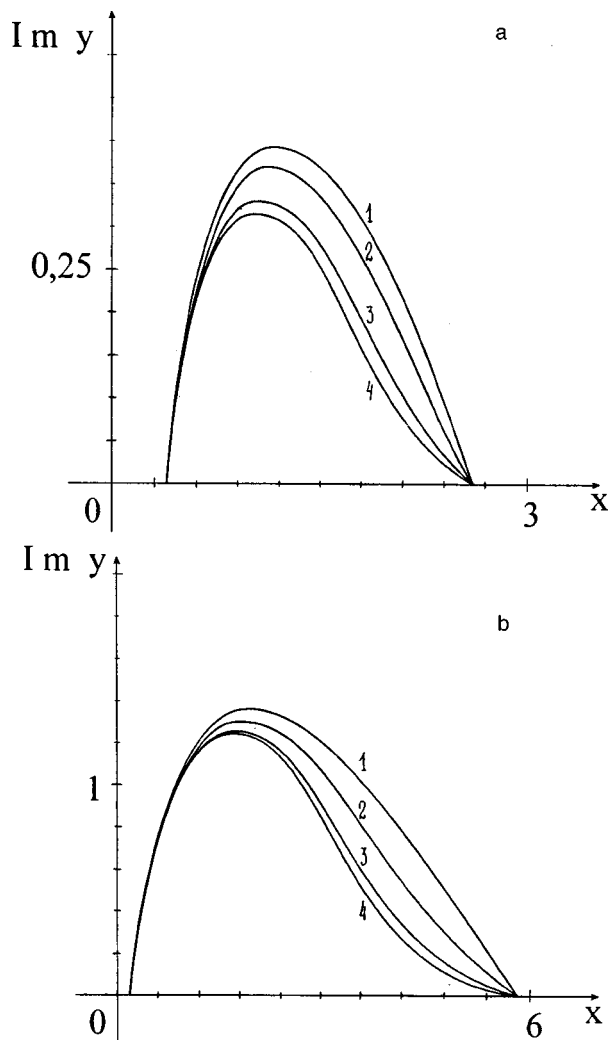
we obtain

FIG. 1. The dimensionless growth rate of the instability of a charged free surface of a liquid subjected to surface tension relaxation as a function of the dimensionless wave number. The dependence was calculated for a — $W = 3$, b — $W = 6$, $\beta = 1$, $\beta_0 = 0.3$, and various values of the characteristic dimensionless relaxation time of the surface tension: 1 — $\tau = 0.2$, 2 — $\tau = 1$; 3 — $\tau = 5$; 4 — $\tau = 10$.

$$[y + 2ix^2]^2 + 4x^4 \sqrt{1 - \frac{iy}{x^2}}$$

$$= \beta x \left(1 + x^2 - Wx - \frac{iy\tau x^2}{1 - iy\tau}\beta_0 \right). \quad (2)$$

The dispersion equation (2), made dimensionless in this manner, in contrast to previous methods used for this purpose (see Refs. 2–5), contains the parameters W, τ, and the wave number x explicitly, and it is not obtained indirectly in terms of more complicated parameters, making it possible to investigate the dependence of the growth rate of the instability of the free surface of the liquid on them directly.

The dependence of the instability growth rate determined by the imaginary positive component of the dimensionless frequency on the dimensionless wave number x, which was calculated according to Eq. (2) with $\beta = 1$, $\beta_0 = 0.3$, and for various values of the characteristic relaxation time τ of the surface tension, is presented in Fig. 1a (for $W = 3$) and Fig. 1b (for $W = 6$). It is evident that as the characteristic relaxation time τ increases, the instability growth rate decreases (approximately by 30% for τ varying by a factor of 50, from 0.2 to 10), but the spectrum of the waves drawn into the unstable motion with a fixed surface charge density on the free surface of the liquid ($W = $ const), does not change. As the surface charge density increases (W increases), the range of unstable wavelengths expands in the direction of capillary waves (in the direction of large values of the wave numbers) and in the direction of gravity waves (in the direction of small values of the wave numbers).

[1] Yu. A. Bykovskiĭ, É. A. Manykin, P. P. Poluéktov et al., Zh. Tekh. Fiz. **46**, 2211 (1976) [Sov. Phys. Tech. Phys. **21**, 1302 (1976)].

[2] O. A. Grigor'ev, Pis'ma Zh. Tekh. Fiz. **20**(24), 7 (1994) [Tech. Phys. Lett. **20**, 974 (1994)].

[3] S. O. Shiryaeva and O. A. Grigor'ev, Pis'ma Zh. Tekh. Fiz. **21**(9), 67 (1995) [Tech. Phys. Lett. **21**, 346 (1995)].

[4] O. A. Grigor'ev and S. O. Shiryaeva, Izv. Ross. Akad. Nauk, Mekh. Zhid. i Gaza, No. 1, 98 (1996).

[5] S. O. Shiryaeva, O. A. Grigor'ev, and A. I. Grigor'ev, Zh. Tekh. Fiz. **66**(10), 31 (1996) [Tech. Phys. **41**, 989 (1996)].

[6] A. I. Grigor'ev, O. A. Grigor'ev, and S. O. Shiryaeva, Zh. Tekh. Fiz. **62**(9), 12 (1992) [Sov. Phys. Tech. Phys. **37**, 904 (1992)].

[7] V. G. Levich, *Physicochemical Hydrodynamics* (Prentice–Hall, Englewood Cliffs, NJ, 1962; Fizmatgiz, Moscow, 1959).

[8] I. N. Aliev and A. V. Filippov, Magn. Gidrodin. No. 4, p. 94 (1989).

Conversion of $F \rightleftarrows F^+$ centers in anion−defective corundum crystals

V. S. Kurtov, I. I. Mil'man, and A. I. Slesarev

Ural State Technical University, Ekaterinburg
(Submitted May 20, 1999)
Pis'ma Zh. Tekh. Fiz. **25**, 66–70 (October 12, 1999)

The method of photostimulated electron emission is used to investigate the processes responsible for redistributing charges formed by photoionization of F centers in anion-defective corundum single crystals in an external electric field. It is shown that the observed features of the excitation spectra are due to conversion transitions between F and F^+ centers, whose probability in the surface layer of the crystal is much higher than in the interior because of the high excitation density and the presence of an electric field. The results obtained could be of interest for studying radiation-stimulated phenomena in dielectric materials. © *1999 American Institute of Physics.* [S1063-7850(99)01110-6]

Here we describe studies of how an electric current flowing under the action of an external electric field during ionization of F centers affects the ratio of the densities of F and F^+ centers created in advance in α-Al_2O_3 crystals by thermochemical treatment.[1] To this end the excitation spectra of photostimulated electron emission (PSEE) were measured in an electric field.[2] The PSEE current, being part of the current of delocalized electrons in the interior of the crystal, carries information about processes occurring in layers up to $\sim 10^2$ nm thick near the surface of a dielectric,[3] and therefore can be used to investigate bulk trapping centers.

The measurements were performed at a pressure $\sim 10^{-5}$ Pa at room temperature. The electron emission current was measured with a secondary electron multiplier (SEM). The intensity of the electric field between the sample and the entrance window of the SEM was ~ 700 V/cm. An LD-1 deuterium lamp served as the light source. An MSD-2 monochromator was used to measure the PSEE spectrum in the photon energy range 6.2–4.1 eV.

In the course of the experiments it was found that in the process of detecting PSEE (i.e., under conditions of extraction of an electron current) the surface of the samples becomes positively charged, which leads first to slow and then rapid decrease of the emission current (Fig. 1). From these measurements we determined the critical excitation period (~ 10 min) for the samples in a field during which the charge effects can be disregarded.

The PSEE excitation spectra of anion-defective corundum crystals are presented in Fig. 2. The emission excitation spectrum of the initial sample has a maximum near the optical absorption of F centers at 205 nm (curve *1*). This shows that the electrons detected are formed as a result of the photoionization of F centers.[2,4] The excitation of samples by radiation with wavelength 205 nm, corresponding to the maximum of the excitation spectrum of electron emission realized with current extraction in 5 min shifts the excitation spectrum, whose maximum is recorded at 230 nm, corresponding to the position of the absorption peak of F^+ centers (curve *2*). The data represented by curves *1* and *2* illustrate

the decrease in the concentration of F centers and increase in the concentration of F^+ centers. However, in ~ 30 min the PSEE spectrum is transformed into the initial spectrum (curves *3–5*). The excitation of the samples by 205 nm radiation without current extraction, i.e., without applying a field, does not change the form of the PSEE excitation spectrum (curve *1* in Fig. 2).

The experimentally observed differences in the excitation spectra of α-Al_2O_3 can be explained by the action of the electric field on the motion of electrons in layers of the crystal near the surface. The excitation radiation ionizes F centers according to the scheme $F + h\nu \Rightarrow F^+ + e$. In an electric field free electrons migrate toward the surface of the crystal. Some of them can be trapped by shallow traps, including
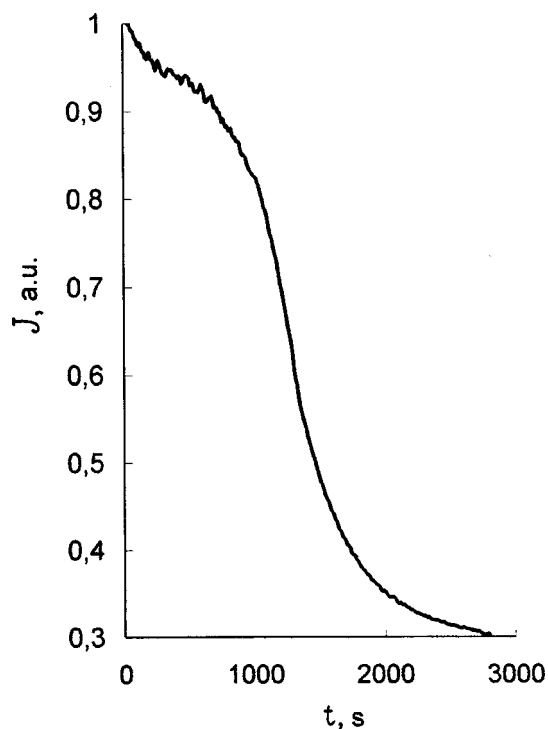

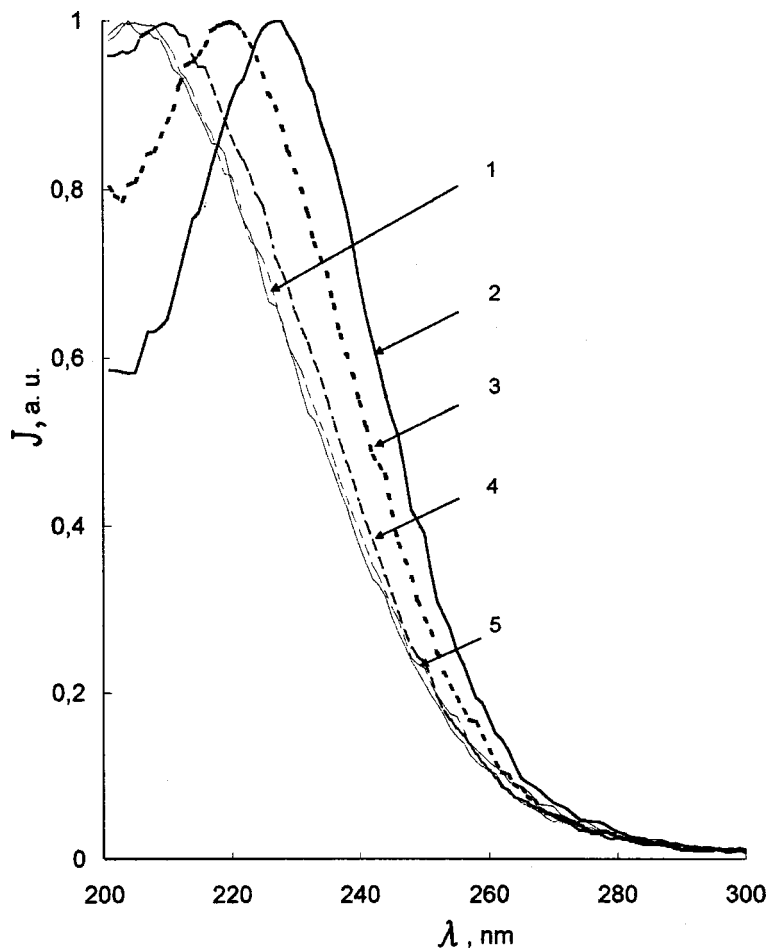FIG. 1. Decay of the PSEE of an aluminum oxide single crystal.

FIG. 2. PSEE excitation spectra of aluminum oxide: *1* — after irradiation with light (200 nm, 300 s, in a field); *2–4* — 600, 1200, and 1800 s after holding in the dark, respectively; *5* — initial sample.

empty anionic vacancies, while the rest are emitted from the surface of the crystal, forming the PSEE current. As a result of $F \Rightarrow F^+$ conversion, the concentration of F centers decreases and that of F^+ centers increases, and the PSEE excitation spectrum shifts into the region of ionization of F^+ centers. The state with excess F^+ centers is unstable with respect to the equilibrium state. After the field is switched off, the trapped electrons with time escape from the traps and are trapped by F^+ centers, which are converted into F centers. The calculations show that the areas under the curves *1* and *2* are approximately the same, i.e., the concentration of F centers is restored to the initial level.

In the absence of a field, the free electrons appearing as a result of ionization of F centers under the action of the excitation radiation cannot leave the ionized centers genetically related with them and are retrapped by them. Since the concentration of F centers in the initial state is much higher than that of F^- centers, subsequent measurements of the PSEE spectrum show that the spectrum does not change and corresponds to the ionization spectrum of F centers.

Note that the processes described occur in a layer of the α-Al_2O_3 crystal with a thickness of the order of the wavelength used to excite the PSEE radiation. A high excitation density is realized in thin emission-active surface layers. This makes it possible to increase substantially the $F \Rightarrow F^+$ conversion efficiency in an electric field. To observe it in the interior of a crystal, in Ref. 4 pulsed excitation had to used,

while in Ref. 5 the corundum crystals had to be irradiated with UV radiation for 30 h. The effect of an electric field was not considered in these works.

The effect of an electric field on the generation of F^+ centers in corundum crystals was established previously. According to the data presented in Ref. 6, in α-Al_2O_3 samples irradiated with 2-MeV electrons the efficiency of the formation of F^+ centers in a field was six times higher than for F centers.

The results obtained, confirming that the conversion process $F \Rightarrow F^+$ is highly efficient in corundum crystals, are of interest in themselves, but they can also be used to explain radiation-induced electric degradation. For example, an investigation of the radiation-induced conductivity of α-Al_2O_3 established that the application of an electric field at the moment of irradiation strongly influences the formation of defects in the lattice of the crystal. Samples irradiated in a field possessed higher conductivity than samples irradiated without a field.[6] It can be inferred that during irradiation of corundum crystals, when oxygen vacancies are formed and the centers created by them become excited at the same time, $F \Rightarrow F^+$ transitions can occur for a certain period of time after irradiation in an electric field. In this case, a high density of charge defects will exist, which will degrade the dielectric properties of a crystal.

[1] M. S. Aksel'rod, V. S. Kortov, and I. I. Mil'man, Izv. Akad. Nauk SSSR, Ser. Fiz. **52**, 1363 (1988).

[2] B. D. Evans and M. Stapelbroek, Phys. Rev. B **18**, 7089 (1978).

[3] A. B. Aleksandrov, É. D. Aluker, I. A. Vasil'ev, S. A. Nechaev, and S. A. Chernov, *Introduction to the Radiation Physics and Chemistry of the Alkali-Halide Crystal Surfaces* (Zinatne, Riga, 1989).

[4] K. H. Lee and J. N. Crawford, Jr., Phys. Rev. B **19**, 3217 (1979).

[5] R. R. Atabekyan, R. K. Ezoyn, V. A. Gevorkyan, and V. L. Vinetskii, Phys. Status Solidi B **129**, 321 (1985).

[6] E. R. Hodgson, in *12th International Conference on Defects in Insulating Materials* (Schloss Nordkirchen, 1992), Vol. 1., pp. 332–341.

Nature of the transitional region during the deposition of titanium boride and nitride films on gallium arsenide

I. B. Ermolovich, R. V. Konakova, V. V. Milenin, and A. I. Senkevich

Institute of Semiconductor Physics, Ukrainian National Academy of Sciences, Kiev
(Submitted January 12, 1999)
Pis'ma Zh. Tekh. Fiz. **25**, 71–76 (October 12, 1999)

Photoluminescence and x-ray photoelectron spectroscopy methods were used to analyze the compositions of the near-junction regions of titanium boride (nitride)–gallium arsenide heterostructures. Data have been obtained for the first time on the formation of $Ga_xB_{1-x}As$ and $GaAs_xN_{1-x}$ solid solutions, which play an important role in the formation of the properties and the thermal stability of the experimental structures on the interphase boundary of these structures. © *1999 American Institute of Physics.* [S1063-7850(99)01210-0]

Titanium borides and nitrides (TiB_x and TiN_x) find wide application as antidiffusion layers in metal–GaAs junctions with multilayer metallization. Considering the high chemical stability of the compounds TiB_x and TiN_x and the possibility of varying their structure-phase composition,[1] it is of interest to use such films not only as stabilizing layers but also as active components of metal–semiconductor (MS) hetero-pairs. In this case, the thermodynamic and kinetic degradation factors of the MS junctions become substantially weaker and so the junction becomes more resistant to extremal perturbations.

In the present work photoluminescence (PL) and x-ray photoelectron spectroscopy (XPES), combined with ion etching with Ar, showed that in the process of formation of TiB_x (TiN_x)–GaAs structures, thin layers of the solid solutions $Ga_xB_{1-x}As$ and $GaAs_xN_{1-x}$, which play an important role in the formation of the electrophysical parameters of the interface and the thermal stability of the MS junctions, arise at the interface.

Figure 1 shows the photoluminescence (PL) spectra of TiB_x–GaAs structures and the dependence of their intensities on the annealing temperature. Analogous PL spectra have also been observed for TiN_x–GaAs structures. The basic PL features of the experimental structures are as follows. Five wide, overlapping bands with $h\nu_{max}=1.54$ (1.57 for TiN_x), 1.33, 1.20, 1.01, and 0.765 eV can be distinguished in the spectra. In the initial state of the structures the strongest band is the 1.01 eV band, which in the literature[2] is attributed to radiative capture of a free electron on an isolated Cu_{Ga} acceptor center. Copper seems to be an uncontrollable impurity in the structures studied. A different PL band with $h\nu_{max}=1.33$ eV which we observed is also attributed to copper. Its centers are the complexes $Cu_{Ga}+D$, where D is an intrinsic (V_{As}) or impurity (Te, Sn, Si) donor.[3]

Annealing at 400 °C redistributes the PL band intensities in favor of the 1.20 eV band and to intensifies the bands, especially in the TiB_x–GaAs structures. This shows that the TiN_x–GaAs structures are more resistant than TiB_x–GaAs to thermal perturbations with respect to the structuring of the spectrum of the defect states. The intensification of the PL in

the entire spectral interval in TiB_x–GaAs structures seems to be due to an improvement of the structural perfection near the junction region and the associated weakening of the non-radiative recombination channel.

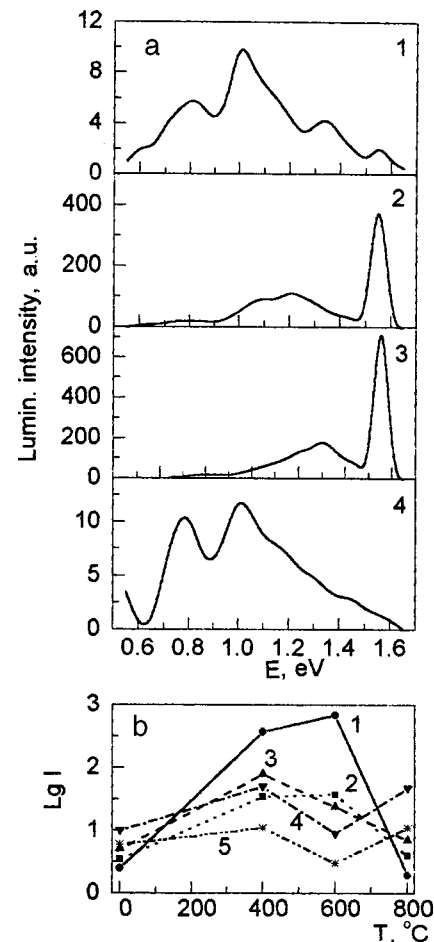The centers of luminescence of the 1.20 eV band, which

FIG. 1. a — PL spectra of the near-junction layers of TiB_x–GaAs structures: initially (1) and after anneals at 400 (2), 600 (3), and 800 °C (4). b — Intensities of PL bands with $h\nu_{max}=1.54$ (1), 1.33 (2), 1.20 (3), 1.01 (4), and 0.765 ev (5) versus the annealing temperature. $T=77$ K.
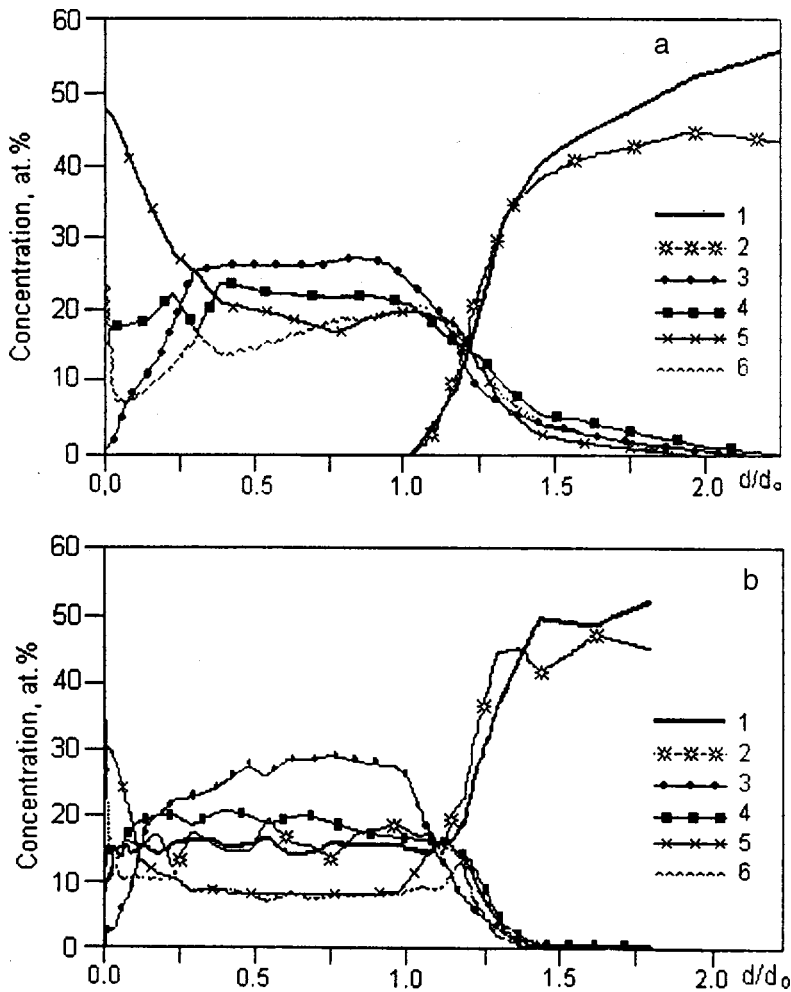
FIG. 2. Atomic profiles of the components of a TiB_x–GaAs junction before (a) and after (b) annealing at 800 °C for 60 s.

becomes the strongest band among the impurity-defect bands after annealing at 400 °C, are V_{Ga}+ D complexes.[4] This may be caused by enrichment of the near-junction region with gallium vacancies because in the presence of interphase interactions of the metallization layers with the semiconductor gallium from the near-junction region, and possibly from the interior, diffuses into the metallization layer. Considering the isoelectronic similarity of B and Ga, it can also be inferred that the solid solution $B_xGa_{1-x}As$ (see below) can form in the presence of excess Ga vacancies at the early stages of boride film growth.

At 600 °C the intensities of all impurity–defect bands in TiB_x–GaAs structures decrease, with the exception of the 1.33-eV band, whose intensity seems to increase somewhat because of the formation of the $Cu_{Ga}+V_{As}$ complexes. This is because at these temperatures the arsenic atoms start to interact effectively with Ti from the metallization layer, forming the compound Ti–As,[5] and the semiconductor becomes enriched with V_{As}. However, the 1.01 eV band becomes weaker because some of its luminescence centers participate in the formation of the complexes mentioned. Such antiphase behavior of the 1.01 and 1.33 eV band intensities during heat treatments is also observed for TiN_x–GaAs structures.

Annealing at 800 °C causes decomposition of the complex centers of the 1.20 and 1.33 eV bands, and the intensi-

ties of these bands decrease (the intensity of the 1.01 eV band increases) and are found to be essentially the same as in the initial state.

The principal feature of the PL spectra of the near-junction regions of the experimental structures is the presence of an emission band of a free exciton with $h\nu_{max}$ =1.54 eV in the TiB_x–GaAs structure and 1.57 eV in the TiN_x–GaAs structure, while the band gap in GaAs at 77 K is 1.51 eV.[6] This is direct evidence of the formation of the corresponding structures of thin layers of the solid solutions $B_xGa_{1-x}As$ and GaN_xAS_{1-x}, respectively, on the interphase boundary. The sharp intensification of the exciton band in the experimental structures as a result of anneals at 400 and 600 °C suggests that at these temperatures further formation of layers of the solid solutions of high crystalline perfection occurs. The sharp quenching of the excitonic band as a result of annealing at 800 °C, just as the other bands, attests to the appearance of a large number of additional nonradiative recombination centers.

The formation of solid solutions on the interphase boundary of the experimental structures was confirmed by independent studies of the chemical composition of the near-junction TiB_x–GaAs layers using XPES. Figure 2 displays the atomic profiles, and Table I gives the binding energies E of the junction components before and after annealing at 600 °C, obtained by layer-by-layer etching of the junction.

TABLE I. Core electron binding energies of the components of a TiB_x–GaAs junction.

Etch time, min	E, eV							
	B 1s		Ga 3d		Ga 2p		As 3d	
	initial	600 °C	initial	600 °C	initial	600 °C	initial	600 °C
0	187.2	187.2	–	–	–	–	–	–
35	187.8	188.0	19.1	19.1	1117.1	1117.1	41.0	–
45	188.0	188.3	19.0	19.2	1117.1	1117.2	41.0	41.2
55	188.0	188.1	19.0	19.3	1117.0	1117.2	41.0	41.2

Based on the data in Fig. 2 and Table I, and the known values of the binding energies of the core levels in the B, Ga, and As compounds,[7] it can be concluded that:

— the deposited titanium boride layers are single-phase with component ratio 2:1;

— anneals at 600 °C do not radically change the chemical structure of the films; and

— the observed shift in the binding energy of the 1s electrons of boron compared with the corresponding value in the interior volume of the film indicates that its chemical coordination changes at the interphase boundary, the most likely reason being that a solid solution $B_xGa_{1-x}As$ is formed. The positions of the maxima of the spectral lines of Ga and As, characteristic for compounds of Ga with As and solid solutions based on them, support this conclusion.

[1] H. Holleck, J. Vac. Sci. Technol. A **4**, 2662 (1986).
[2] T. N. Morgan, M. Pilkuhn, and H. Rupprecht, Phys. Rev. **138**, 1551 (1965).
[3] N. S. Averkiev, T. K. Ashirov, and A. A. Gutkin, Fiz. Tekh. Poluprovodn. **15**, 1970 (1981) [Sov. Phys. Semicond. **15**, 1145 (1981)].
[4] E. W. Williams, Phys. Rev. **168**, 922 (1968).
[5] C. E. McCants, T. Kindelevicz, and P. H. Mahovald, J. Vac. Sci. Technol. A **6**, 1466 (1988).
[6] E. Grilli, M. Guzzi, and R. Zamboni, Phys. Rev. B **45**, 1638 (1992).
[7] V. I. Nefedov, *Handbook of X-Ray Electronic Spectroscopy of Chemical Compounds* (Khimiya, Moscow, 1984).

Translated by M. E. Alferieff

Use of lead as a neutral solvent for obtaining solid $Ga_{1-x}In_xAs_ySb_{1-y}$ solutions

I. A. Andreev, E. V. Kunitsyna, and Yu. V. Solov'ev

A. F. Ioffe Physicotechnical Institute, Russian Academy of Sciences, St. Petersburg

The first results of an experimental investigation of the phase diagram of melting of the system Ga–In–As–Sb–Pb at temperatures 560 and 600 °C are presented. The solid solutions $Ga_{0.86}In_{0.14}As_{0.12}Sb_{0.88}$ at $T = 600$ °C and $Ga_{0.81}In_{0.19}As_{0.16}Sb_{0.84}$ at $T = 560$ °C, which are isoperiodic with the GaSb(100) substrate, are obtained from fluxed lead solutions. The experimental data are compared with theoretical calculations. © *1999 American Institute of Physics.* [S1063-7850(99)01310-5]

In order to exploit solid $Ga_{1-x}In_xAs_ySb_{1-y}$ solutions for very efficient fast photodiodes with low dark reverse currents it is necessary to use epitaxial layers in the active region with a low carrier density. Without deliberate doping gallium antimonide (GaSb) and solid $Ga_{1-x}In_xAs_ySb_{1-y}$ solutions with similar composition, obtained by liquid-phase epitaxy (LPE) at temperatures $T = 500$–600 °C, are always p-type. It is assumed that this is due to the high density of natural acceptors, V_{Ga} and Ga_{Sb} defects and their complexes.[1] Various methods exist for decreasing the concentration of natural acceptors and residual impurities: doping with a donor impurity, use of rare-earth elements, growing from antimony-enriched melts. It has been shown[2–4] that when binary solid solutions GaSb are obtained from Pb–Ga–Sb melts, the ratio of the molar fractions of the components in the liquid phase strongly influences the character and demsity of structural defects. At the same time, lead (Pb) is a neutral solvent, i.e., it does not form compounds with any components of the melt, it is not incorporated into the solid phase, and therefore it does not influence the electrophysical characteristics of the material directly. This method allowed the density of characteristic defects in GaSb epitaxial layers to be reduced substantially—from 2.7×10^{17} to 2×10^{15} cm³.[4] In individual cases, even a change in the type of conductivity (p to n type) in the undoped layers was observed. Since the basic properties of the solid solutions $Ga_{1-x}In_xAs_ySb_{1-y}$ based on

GaSb are largely determined by the properties of GaSb, the use of lead in obtaining such solid solutions by the LPE method is promising from the standpoint of decreasing the carrier density in the epitaxial layers without doping with a donor impurity.

The present letter reports the first results of an experimental investigation of phase equilibria in the system Ga–In–As–Sb–Pb at temperatures 560 and 600 °C for the purpose of obtaining $Ga_{1-x}In_xAs_ySb_{1-y}$ solid solutions which are isoperiodic to GaSb.

Epitaxial layers of the solid solutions $Ga_{1-x}In_xAs_ySb_{1-y}$ were grown by LPE with cooling of Ga–In–As–Sb–Pb fluxed solutions at rates of 0.3–0.6 grad/min. Single-crystal n- and p-type GaSb wafers, oriented in the (100) crystallographic plane, were used as the substrates. The charge contained the binary compounds GaSb, InAs, and In with purity 99.999 wt.%, Sb with purity 99.999 wt.%, and Pb with purity 99.9999 wt.%. The layers were not deliberately doped. The chemical composition of the solid solutions obtained was determined by the method of quantitative x-ray spectral analysis using a JXA-5 CAMEBAX x-ray microanalyzer. The mismatch $\Delta a_\perp /a$ of the lattice parameters of the epitaxial layer and the substrate was measured by two-crystal x-ray diffractometry using a TRS-1 diffractometer. The thickness of the epitaxial layers was determined using a MIK-1 microscope on the transverse cleavage surfaces of the structures.
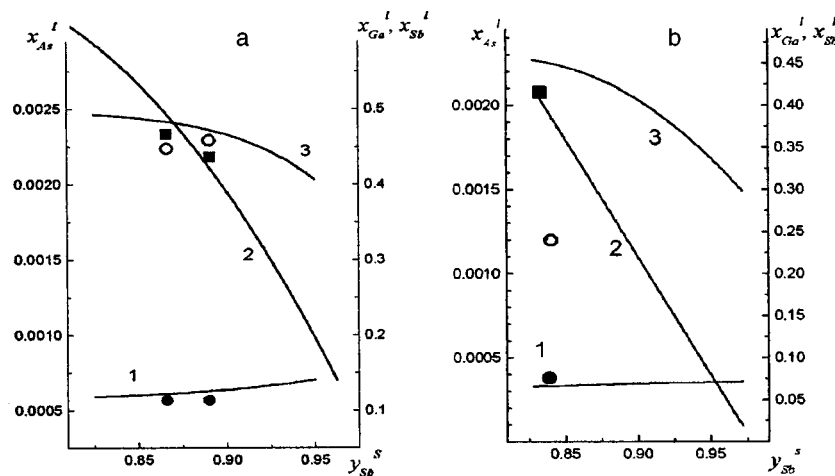

FIG. 1. Compositions of coexisting liquid and solid phases on a GaSb substrate in the heterogeneous system Ga–In–As–Sb–Pb at $T = 600$ °C (a) and $T = 560$ °C (b): solid lines — calculation using the IFLPKP model; y_{Sb}^s — molar fraction of Sb in the solid phase, 1 — molar fraction of Ga in the liquid phase (x_{Ga}^l), 2 — molar fraction of As in the liquid phase (x_{As}^l), 3 — molar fraction of Sb in the liquid phase (x_{Sb}^l), dots — our experimental data.

TABLE I. Parameters of epitaxial layers of $Ga_{1-x}In_xAs_ySb_{1-y}$.

Preparation temperature T, °C	GaInAsSb −3				Molar fraction of Pb in the liquid phase	Carrier density p, cm
	theory		experiment			
	x	y	x	y	x_{Pb}^l	
600	0.119	0.100	0.143	0.116	0.079	$(1-2)\times10^{17}$
560	0.124	0.105	0.190	0.163	0.175	$(1-2)\times10^{16}$

To reveal the interphase, the cleavage surface of the structure was first subjected to electrochemical oxidation in an electrolytic solution with $I=50$ mA and $U=100$ V or treated in the etchant $HF : HNO_3 : H_2O = 1 : 3 : 3$ at room temperature for 3 s. The carrier density in the epitaxial layers was determined by the C–V method according to the capacitance–voltage characteristics of the structures.

The equilibrium values of the molar fractions of the components in the liquid and solid phases with fixed temperature ($T=560$, $600\,°C$) and supercooling ($\Delta T=3$ $-8\,°C$) were calculated by the dynamic method proposed in Refs. 5 and 6. To obtain $Ga_{1-x}In_xAs_ySb_{1-y}$ solid solutions isoperiodic to the substrate, the composition of the liquid phase, determined using a theoretical calculation, was determined more accurately experimentally. For this, first the gallium (Ga) content in the liquid phase was determined at intervals of 0.001 molar fractions, and then the arsenic (As) content was determined at intervals of 0.0001 molar fractions. As a result of the experiments, at $T=600\,°C$ with supercooling by $\Delta T=3\,°C$, we obtained epitaxial layers of the solid solutions $Ga_{1-x}In_xAs_ySb_{1-y}$ ($x=0.143$, $y=0.116$) which were isoperiodic with the GaSb(100) substrate. The rate of growth, calculated as the ratio of the layer thickness to the growth time, was 0.8 ± 0.1 μm/s, which is much higher than the rate of growth of epitaxial layers with the same composition obtained under the same conditions from fluxed indium solutions without using lead. According to x-ray diffractometry data, all samples showed a positive lattice mismatch between the layer and the substrate $\Delta a_\perp/a=(8-9)$ $\cdot10^{-4}$, at room temperature. The half-widths of the diffraction reflection curves were $16-20''$ for the layers and $10''$ for the substrate, indicating high structural perfection of the epitaxial layers and planarity of the substrate–layer interface. At $T=560\,°C$ and $\Delta T=8\,°C$ supercooling, epitaxial layers of the solid solutions $Ga_{1-x}In_xAs_ySb_{1-y}$ ($x=0.190$, $y=0.163$) isoperiodic with the GaSb(100) substrate were obtained. The growth rate was 0.6 ± 0.1 μm/min, which is higher than the growth rate of epitaxial layers of the same composition which were obtained at $T=560\,°C$ from fluxed indium solutions without using lead. The mismatch for all samples produced was $\Delta a_\perp/a=(9-11)\times10^{-4}$ at room temperature. The half-widths of the diffraction reflection curves were in the range $10-12''$ for the substrate in all samples and $19-26''$ for the layers, which is somewhat larger than for the structures which we obtained at $T=600\,°C$.

The results of the theoretical calculation of the compositions of the coexising liquid phase and solid phase isoperi-odic with GaSb at $T=560\,°C$ and $T=600\,°C$ in the heterogeneous Ga–In–As–Sb- -Pb system, and the experimental data obtained are presented in Fig. 1. The theoretically calculated indium and arsenic concentrations in the solid phase of the isoperiodic solid $Ga_{1-x}In_xAs_ySb_{1-y}$ solutions in all samples were less than the experimentally established values by the amounts $\Delta x=0.024\pm0.005$ and $\Delta y=0.016\pm0.005$ for growth temperature $T=600\,°C$ and $\Delta x=0.066\pm0.005$ and $\Delta y=0.058\pm0.005$ for growth temperature $T=560\,°C$ (see Table I).

According to x-ray spectral analysis data, lead was not observed by this method in the solid phase in any samples, though it was present in the liquid phase at the level 0.08 molar fractions at $T=600\,°C$ and 0.175 molar fractions at $T=560\,°C$. This confirms that this solvent is neutral.

The carrier density in the epitaxial layers of the solid solution p-$Ga_{0.86}In_{0.14}As_{0.12}Sb_{0.88}$, determined from the capacitance–voltage characteristics, was $p=(1-2)\times10^{17}$ cm^{-3}. This value is no lower than the typical value for undoped $Ga_{1-x}In_xAs_ySb_{1-y}$ layers with the same composition, grown under the same conditions from fluxed indium solutions without using Pb on GaSb substrates without an intermediate layer.[4] This can be explained by the fact that the Pb content in the liquid phase in this case is still insufficient for a large effect ($x_{Pb}\sim0.08$). In p-$Ga_{0.81}In_{0.19}As_{0.16}Sb_{0.84}$ layers obtained from the liquid phase with lead content 0.18 molar fractions, the hole density is an order of magnitude lower, $p=(1-2)\times10^{16}$ cm^{-3}.

For more detailed conclusions about the electrophysical properties of $Ga_{1-x}In_xAs_ySb_{1-y}$ solid solutions obtained using lead, the galvanomagnetic properties of the grown epitaxial layers must be investigated in detail.

[1] P. S. Dutta, H. L. Bhat, and V. Kumar, J. Appl. Phys. **81**, 5821 (1997).
[2] A. N. Baranov, A. M. Litvak, and V. V. Sherstnev, Izv. Akad. Nauk SSSR, Neorg. Mater. **25**, 922 (1989).
[3] A. N. Baranov, T. I. Voronina, T. S. Lagunova, I. N. Timchenko, Z. I. Chugueva, V. V. Sherstnev, and Yu. P. Yakovlev, Fiz. Tekh. Poluprovodn. **23**, 780 (1989) [Sov. Phys. Semicond. **23**, 490 (1989)].
[4] T. I. Voronina, B. E. Dzhurtanov, T. S. Lagunova, M. A. Sipovskaya, V. V. Sherstnev, and Yu. P. Yakovlev, Fiz. Tekh. Poluprovodn. **32**, 278 (1998) [Sov. Phys. Solid State **32**, 250 (1998)].
[5] A. M. Litvak and N. A. Charykov, Zh. Fiz. Khim. **64**, 2331 (1990).
[6] A. M. Litvak and N. A. Charykov, Izv. Akad. Nauk SSSR, Neorg. Mater. **27**, 225 (1991).

Kinetics of free radicals in the plasma of a spark discharge in methane

A. V. Kirikov, V. V. Ryzhov, and A. I. Suslov

Institute of High-Current Electronics, Siberian Branch of the Russian Academy of Sciences, Tomsk
(Submitted June 3, 1999)
Pis'ma Zh. Tekh. Fiz. **25**, 82–86 (October 12, 1999)

The kinetics of reactions in the plasma of a spark discharge in methane at atmospheric pressure
is analyzed using numerical simulation, taking account of the gas-dynamic expansion of
the channel. The processes leading to the formation and annihilation of CH_x radicals are
investigated and the conditions under which their maximum concentration is reached
are determined. The results obtained are of interest for plasma chemical technologies for
processing natural gas. © *1999 American Institute of Physics.* [S1063-7850(99)01410-X]

The investigation of processes leading to the decomposition of methane in a gas-discharge plasma is of interest for producing new technologies for utilizing natural gas. Specifically, a gas-discharge plasma is the basis of plasma-chemical technologies for synthesizing acetylene and obtaining polymer and diamond-like coatings on surfaces consisting of various materials. An important aspect of these technologies is the question of producing a plasma with a high degree of dissociation of CH_4.

Experimental and theoretical investigations of the kinetics of the decomposition of CH_4 in arc, barrier, corona, rf, and microwave discharges, as a rule, at low gas pressures, have now been published.[1-3] In the present work we examine an atmospheric-pressure spark discharge in methane with energy inputs of $(1.0–4.0) \times 10^{-2}$ J. The objective of the present work is to investigate theoretically the conditions for obtaining the maximum yield of CH_x for developing effective plasma-chemical technologies based on a spark discharge.

A self-consistent model of a spark discharge includes the streamer propagation stage, the production of a spatial distribution of charged particles in the gap, and the transition of the discharge into the high-current stage, during which the main energy release and production of free radicals occur. The fraction of energy released at the first stage is low compared with the high-current discharge stage and is of interest mainly from the standpoint of producing the initial conductivity in the gap. In this connection, the kinetics of CH_4 dissociation has been investigated only during the main energy release in the gap.

The simulation of the spark discharge included simultaneous solution of the one-dimensional gas-dynamics equations, describing the density and temperature of the gas in the channel, the equations of particle kinetics in the gas-discharge plasma, and the equations of the electric power-supply circuit, which are required for calculating the intensity E of the electric field in the gap. To solve the kinetics equations and to determine E/N (N is the neutrals density) it was assumed that E/N, the gas temperature, and the densities of all particles are independent of the radius of the spark channel. To calculate the rate constants of the elementary processes involving electrons, the transport coefficients, and

the electron temperature, Boltzmann's equation was solved numerically for the electron energy distribution function. The plasma-chemical reactions included more than 50 processes involving charged and neutral particles.[4] It was assumed that CH_x radicals with one to three free bonds participate in the processes leading to the formation of an *a*-C:H film. Knowing the "attachment" coefficient α of these radicals to the substrate and the fraction δ of radicals reaching the surface of the substrate, the film growth rate can be estimated.

In gas discharges the formation of CH_x radicals is determined by the process leading to the dissociation of methane by direct electron impact:

$$CH_4 + e \rightarrow CH_4^* \rightarrow CH_3 + H,$$
$$\rightarrow CH_2 + H_2,$$
$$\rightarrow CH + H_2 + H,$$
$$\rightarrow C + 2H_2. \tag{1}$$
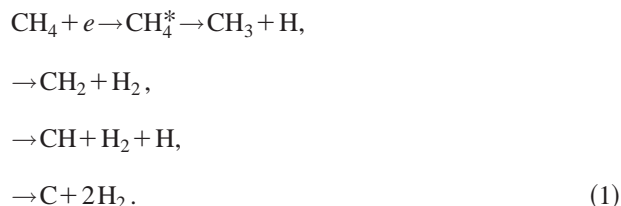
Of all channels of this reaction, the most likely is the first one (the probability for the appearance of products is 0.6–0.8).[1,3] Since the gas temperature in the channel is quite high, the rate constants of the gas-phase reactions with a high activation barrier increase and the rates of certain reverse processes, for example,

$$H + CH_3 + M \rightarrow CH_4 + M, \tag{2}$$

conversely, decrease.[1] As a result, the conditions for accumulation of methyl radicals arise in the spark channel. The decrease in the rate of the reaction (2) is also due to the decrease in the gas density as a result of the gas-dynamic expansion of the channel.

Figure 1 shows curves of the particle densities in the plasma at the end of the current pulse versus the energy input W, which were calculated for the experimental conditions of Ref. 5. It follows from the calculations that for a high degree of dissociation of methane $[CH_x]/[CH_4] > 1$, first CH_3 and then CH_2 accumulate. In the presence of a large amount of atomic hydrogen, this radical transforms very rapidly into CH:

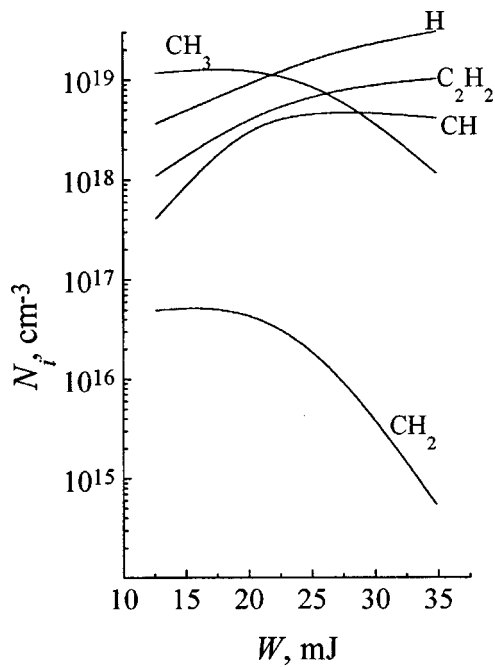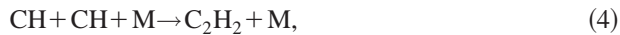FIG. 1. Densities N_i of certain components 30 ns after the start of the discharge as a function of the energy input W.

$$CH_2 + H \rightarrow CH + H_2. \tag{3}$$

Therefore, as $W > 20$ mJ increases, methane decomposes to CH, which leads to the synthesis of acetylene:

$$CH + CH + M \rightarrow C_2H_2 + M, \tag{4}$$

$$CH + CH_3 \rightarrow C_2H_2 + H. \tag{5}$$

According to the calculations, these processes can dominate in the range 20 mJ $< W <$ 40 mJ and appreciably decrease the total concentration of all carbon levels in the discharge. For still higher energy inputs, methane should decompose to atomic carbon and hydrogen.

To estimate the maximum growth rate ν of the coating on the dielectric surface, we shall assume that all radicals reaching the substrate surface participate in film formation ($\alpha = 1$). From simple geometric considerations, the coefficient δ for the experimental conditions of Ref. 5 is of order 0.4. The computed dependence of the growth rate W of the film for the chosen values of α and δ is presented in Fig. 2 (curve *2*). The experimental data on the deposition rate (curve *1*), which were obtained in Ref. 5, are also displayed in the figure. Both dependences have a maximum, and in the
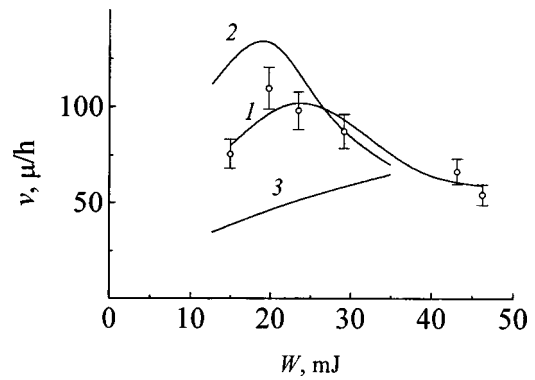

FIG. 2. Growth ν of an α-C:H film as a function of the energy input W: *1* — curve approximating the experimental points of Ref. 5; *2* — calculation for a spark discharge; *3* — calculation for conditions of a self-sustained volume discharge.

calculation it corresponds to the maximum CH_x yield. This confirms the assumption that these radicals are the initial material in the processes leading to the deposition of diamond-like films.

To investigate the effect of gas-dynamic expansion and heating of the gas in a spark channel on the generation of the radicals CH_x, calculations of $\nu(W)$ under typical conditions of a pulsed self-sustained volume discharge were performed (curve *3* in Fig. 2). Compared with a spark discharge, the coating deposition rate in a volume discharge for the energy inputs considered is much lower and increases monotonically with W. This is because when the gas in the bulk discharge is at atmospheric pressure and low temperature the rates of binding of free radicals are much higher, which decreases their yield.

In summary, regimes with high production rates of CH_x radicals can be obtained in an atmospheric-pressure discharge in methane. These regimes ae due to the low density and high temperature of the gas in the plasma channel, which makes such discharges promising for coating deposition technologies.

[1] J.-C. Legrand, A. M. Diamy, R. Hrach *et al.*, in *Proceedings of ISPC 12, Minneapolis, August 21–25, 1995*, pp. 601–606.
[2] L. E. Klein, W. D. Partlow, and W. E. Bies, J. Appl. Phys. **65**, 70 (1989).
[3] K. Tashiba, M. Nishida, and H. Harima, J. Phys. D **17**, 1727 (1984).
[4] Yu. N. Novoselov, V. V. Ryzhok, and A. I. Suslov, Pis'ma Zh. Tekh. Fiz. **24**(19), 40 (1998) [Tech. Phys. Lett. **24**, 764 (1998)].
[5] S. P. Bugaev, A. D. Korotaev, K. V. Oskomov *et al.*, *Surface and Coatings Technology 96* (1997), pp. 123–128.

Translated by M. E. Alferieff

Possible use of two-dimensional Bragg structures in an FEL amplifier powered by a sheet electron beam

N. S. Ginzburg, A. S. Sergeev, N. Yu. Peskov, A. V. Arzhannikov, and S. L. Sinitskiĭ

Institute of Applied Physics, Russian Academy of Sciences, Nizhniĭ Novgorod; Institute of Nuclear Physics, Siberian Branch of the Russian Academy of Sciences, Novosibirsk
(Submitted July 2, 1999)
Pis'ma Zh. Tekh. Fiz. **25**, 87–95 (October 12, 1999)

It is shown that two-dimensional doubly-periodic Bragg structures can be used effectively in the amplification schemes of free electron lasers powered by sheet relativistic electron beams. The presence of such a structure ensures spatial coherence of radiation from different parts of the electron beam when the input signal propagates across the electron flux. Theoretical analysis shows that the gain in the regenerative scheme can reach 50 dB. © *1999 American Institute of Physics.* [S1063-7850(99)01510-4]

High-power free electron lasers (FELs) powered by a sheet electron beam whose width can reach 1.4 m are being intensively studied theoretically and experimentally.[1,2] It has been suggested that the two-dimensional distributed feedback (DFB), realized using two-dimensional Bragg resonators,[3,4] be used to obtain spatial coherence of the radiation from different parts of the electron beam. Such a resonator consists of two flat plates on which doubly-periodic ripples are imposed. It is found that four partial electromagnetic waves are coupled and scatter one another on these ripples. Two of the waves propagate parallel and antiparallel to the translational motion of the electron beam, while the other two propagate in the transverse direction. It is possible in principle to obtain gigawatt millimeter-range radiation by using two-dimensional DFB and sheet electron beams produced in the U-2 accelerator (Institute of Nuclear Physics, Siberian Branch of the Russian Academy of Sciences). Normal operation of the new FEL scheme has been confirmed experimentally on a simulation beam up to 12 cm wide. One-hundred megawatt radiation has been obtained at a wavelength of 4 mm.[5]

In this connection, it is of great practical interest to develop an amplifier that uses powerful sheet relativistic electron beams (REBs). An important problem in realizing such an amplifier is the introduction of the input signal, giving amplification that has a controllable phase front and is uniform over the width of the electron beam. As shown in the present work, this problem can also be solved by using a two-dimensional Bragg structure. Two situations are possible depending on the region where the undulator field is switched on. If the undulator field and, correspondingly, the interaction of the electron flux with the radiation field is switched on after the electron beam has passed through the Bragg structure, then such a structure will play the role of an input device. However, if the undulator field is switched on before the beam passes through the indicated structure, then, taking account of the fact that part of the electromagnetic energy propagates antiparallel to the translational motion of the electrons, the electron–wave interaction inside the struc-

ture will make it possible to obtain regenerative amplification characterized by a high gain.

Let us assume that the input radiation is a quasioptical wave beam incident on the system in the direction transverse to the translational motion of the sheet beam (Fig. 1a). In the regenerative scheme, to ensure symmetry of the output radiation, it is desirable to introduce radiation from two sides. The field inside the Bragg structure can be represented as a set of four partial waves

$$\mathbf{E} = \mathbf{E}_0 \mathrm{Re}([\mathcal{A}_+ e^{-ihz} + \mathcal{A}_- e^{ihz} + \mathcal{B}_+ e^{-ihx} + \mathcal{B}_- e^{ihx}]e^{i\omega t}), \quad (1)$$

two of which ($\mathcal{A}_\pm$) propagate parallel and antiparallel to the direction of motion of the electron beam and two ($\mathcal{B}_\pm$) propagate in the transverse direction (Fig. 1b).

The mutual scattering of waves on a two-dimensional Bragg structure and their amplification by an electron flux can be described by the following system of equations,[6] where it is assumed that the electron beam can interact synchronously only with the wave $\mathcal{A}_+$:

$$\left(\frac{\partial}{\partial Z} + \beta_{\mathrm{gr}}^{-1} \frac{\partial}{\partial \tau} \right) A_+ + i\alpha(B_+ + B_-) = J,$$

$$J = \frac{1}{\pi} \int_0^{2\pi} e^{-i\theta} d\theta_0,$$

$$\left(\frac{\partial}{\partial Z} - \beta_{\mathrm{gr}}^{-1} \frac{\partial}{\partial \tau} \right) A_- + i\alpha(B_+ + B_-) = 0,$$

$$\left(\frac{\partial}{\partial X} \pm \beta_{\mathrm{gr}}^{-1} \frac{\partial}{\partial \tau} \right) B_\pm + i\alpha(A_+ + A_-) = 0,$$

$$\left(\frac{\partial}{\partial Z} + \beta_\parallel^{-1} \frac{\partial}{\partial \tau} \right)^2 \theta = \mathrm{Re}\,(A_+ e^{i\theta}). \quad (2)$$

Here the following normalized variables are used: $Z = zC\bar{\omega}/c$, $X = xC\bar{\omega}/c$, $\tau = tC\bar{\omega}$, $A_\pm = \mathcal{A}_\pm e\kappa\mu/\gamma mc\bar{\omega}C^2$, where $\kappa \approx \beta_\perp/\beta_\parallel$ is the electron–wave coupling parameter, $\mu \approx \gamma^{-2}$ is the inertial bunching parameter,[7] γ is
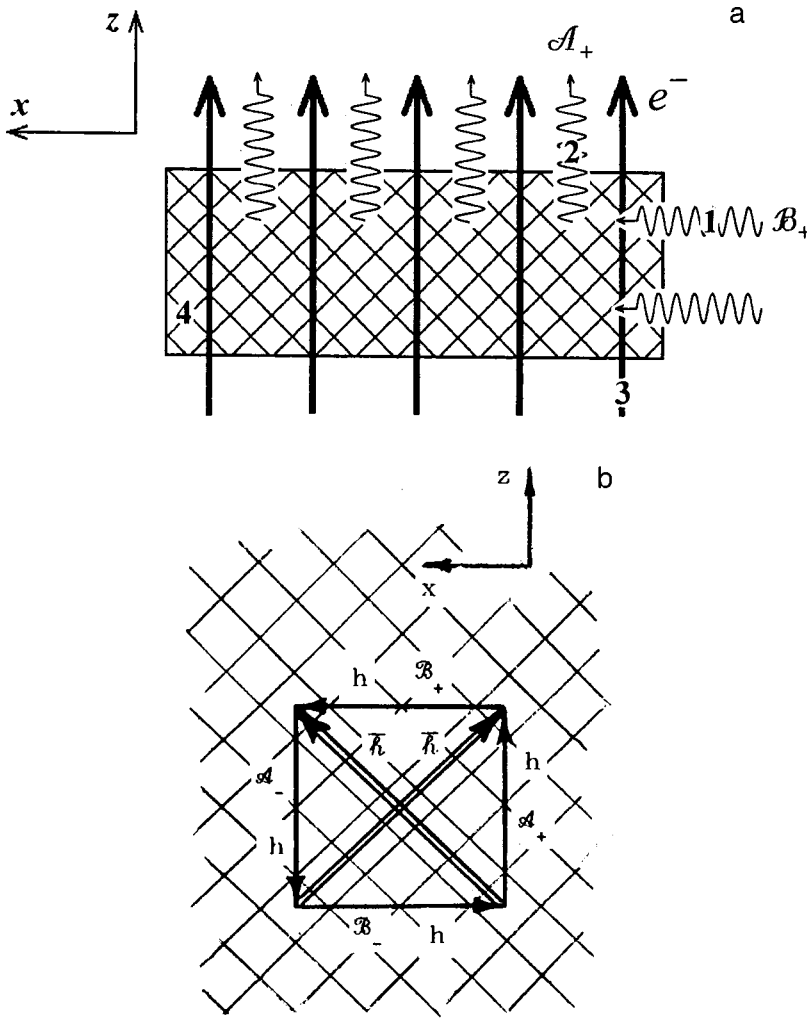
FIG. 1. a — Radiation input ($\mathcal{B}_+$(1) wave) and output ($\mathcal{A}_+$ (2) wave) schemes in an FEL amplifier with a sheet REB (3) and a two-dimensional Bragg structure (4). b — Diagram illustrating scattering of partial waves by a two-dimensional Bragg structure (**h** — wave vectors of the partial waves $\mathcal{A}_\pm$ and $\mathcal{B}_\pm$, $\bar{h}$ — translational lattice vectors).

the relativistic mass factor of the electrons, $\beta_\parallel$ is the translational velocity of the particles, β_{gr} is the group velocity of the waves,

$$C = \left(\frac{eI_0}{mc^3} \frac{\lambda^2 \mu \kappa^2}{8\pi \gamma SN} \right)^{1/3}$$

is the gain parameter (Pierce parameter), I_0 is the beam current, S is the cross-sectional area of the interaction space, N is the norm of the synchronous wave, and α is the coupling coefficient of the waves on Bragg structures and is proportional to the depth of the fluting.[8]

For an amplifier we have the following boundary conditions for the fields of the partial waves:

$$A_+(Z=0) = 0, \quad A_-(Z=L_z) = 0,$$

$$B_+(X=0) = B_+^0(Z)e^{i\delta\tau},$$

$$B_-(X=L_x) = B_-^0(Z)e^{i\delta\tau}. \tag{3}$$

Here $\delta = (\omega - \bar{\omega})/\bar{\omega}C$ characterizes the detuning of the frequency of the external signal from the carrying frequency, for which the Bragg frequency $\bar{\omega}$ is chosen. The boundary conditions for the electron flux in the absence of initial modulation have the form

$$\theta(Z=0) = \theta_0 \in [0; 2\pi),$$

$$\left(\frac{\partial}{\partial Z} + \beta_\parallel^{-1} \frac{\partial}{\partial \tau} \right) \theta(Z=0) = -\Delta, \tag{4}$$

where $\Delta = (\bar{\omega} - h(\bar{\omega})v_\parallel - \Omega_b)/\bar{\omega}C$ is the initial detuning of the synchronization of electrons with the wave and Ω_b is the bounce frequency of electron oscillations in the undulator field.

We shall consider first the problem in the absence of an interaction with the electron flux, i.e., we shall assume that the undulator field is switched on after the electrons pass through the Bragg structure. When the frequency of the incident wave B_+ is the same as the Bragg frequency $\delta = 0$, and $B_-^0 = 0$, we obtain from Eqs. (2) the following solution for the amplitudes of the scattered waves:

$$B_+ = B_+^0(Z) - GX, \quad B_- = G(X - L_x),$$

$$A_+ = i\alpha L_x GZ - i\alpha \int_0^Z B_+^0(z)\,dz,$$

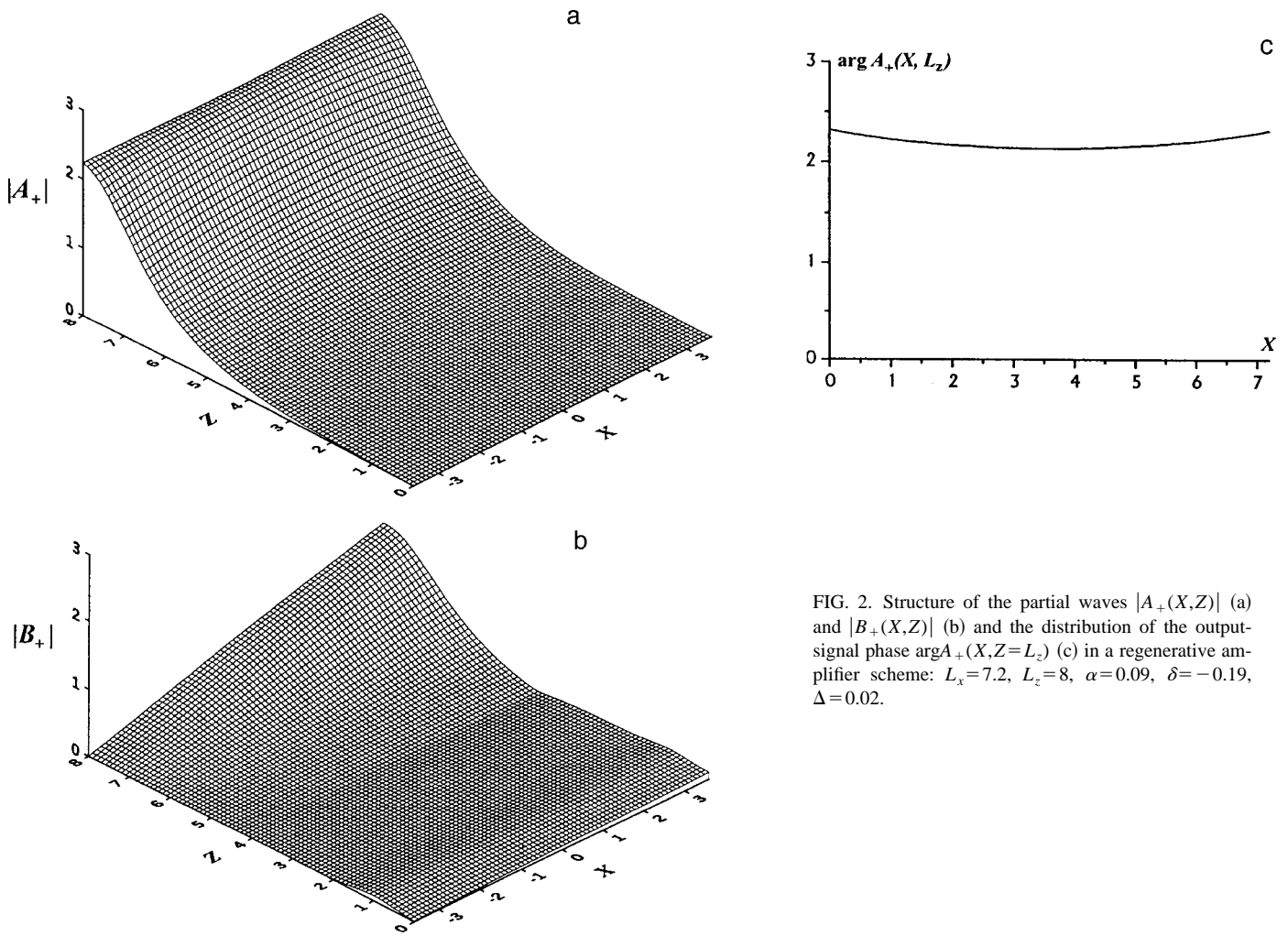$$A_- = -i\alpha L_x G(Z - L_z) + i\alpha \int_{L_x}^Z B_+^0(z)\,dz, \tag{5}$$

where

FIG. 2. Structure of the partial waves $|A_+(X,Z)|$ (a) and $|B_+(X,Z)|$ (b) and the distribution of the output-signal phase $\arg A_+(X,Z=L_z)$ (c) in a regenerative amplifier scheme: $L_x=7.2$, $L_z=8$, $\alpha=0.09$, $\delta=-0.19$, $\Delta=0.02$.

$$G = \frac{\alpha^2}{1+\alpha^2 L_z L_x} \int_0^{L_z} B_+^0(z)\,dz.$$

As follows from the relations (5), a two-dimensional Bragg structure makes it possible to excite a wave A_+ which is synchronous with the beam and has a constant amplitude along the coordinate x (i.e., along the transverse section of the electron flux) and a plane phase front $\partial A_+/\partial X=0$. The maximum efficiency for conversion of the incident power $B_+(X=0)$ into the power $A_+(Z=L_z)$ of the wave synchronous with the electrons is obtained for $\alpha^2 L_x L_z=1$ and reaches 25%.

To analyze the regenerative scheme, we shall determine below the gain as the ratio of the power of the incident wave to the output power amplified by the electron flux of the wave:

$$\Gamma = \int_0^{L_x} |A_+(X,Z=L_z)|^2 dX / \int_0^{L_z} (|B_+(X=0,Z)|^2$$

$$+ |B_-(X=L_x,Z)|^2)dZ. \tag{6}$$

It should be kept in mind that a part (relatively small, as will be shown below) of the output power will be associated with other partial waves. It is also important to emphasize that stationary one-frequency amplification regimes are investi-

gated in what follows. Nonetheless, Eqs. (2) include the time dependence of the wave amplitudes. Actually, simulation of transient processes is used here as an effective method for solving the nonlinear boundary-value problem, making it possible to determine at the same time the limits of self-excitation of the system.

Figure 2a shows the distribution of the amplitude of the amplified wave over the interaction space when the frequency of the external signal lies at the limit of the nontransmission band of a two-dimensional Bragg structure $\delta \approx \pm 2\alpha$. It was assumed that the input signal is a Gaussian beam. To ensure symmetry of the output radiation, this signal was introduced from two sides. As one can see from Fig. 2a, the amplitude of the field at the exit $Z=L_z$ is essentially constant, which implies that energy extraction is almost identical for all fractions of the electron flux along the coordinate X. The phase front of the radiation at the exit is close to planar (Fig. 2c). The gain is quite high, and for a normalized length of the interaction space $L_z \approx 8$ it exceeds 50 dB. The amplitudes of the partial waves different from A_+ are small at the exit from the resonator, and the integrated power associated with these waves is about 10% of the output power of the working wave (Fig. 2d). It should be noted that the present system with maximum gain ~ 50 dB is an extremely
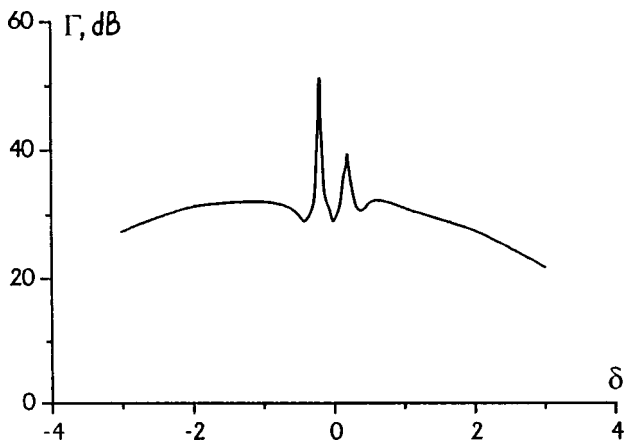
FIG. 3. Gain Γ versus the normalized detuning δ of Bragg resonance in a regenerative amplifier scheme: $L_x = 7.2$, $L_z = 8$, $\alpha = 0.09$, $\Delta = 0.02$.

narrow-band system (Fig. 3), while at a gain of 30 dB the bandwidth is $\Delta \delta \approx 4$, which with Pierce parameter 3×10^{-3} corresponds to $\sim 1 - 1.5\%$ in frequency.

In summary, the analysis performed above shows that there is promise in using two-dimensional Bragg structures in ordinary and regenerative schemes of FELs powered by sheet REBs. These schemes can obviously also be combined, in which case the interaction of the synchronous wave with the electron flux continues after the Bragg structure cuts off.

We conclude by estimating the parameters of a regenerative FEL amplifier with wavelength $\lambda = 4$ mm based on the U-2 accelerator, forming sheet REBs with transverse dimensions reaching 140 cm, current per unit length 300 A/cm, particle energy 1 MeV, and pulse duration of about 5 μs. Let the period of the undulator be 4 cm, the oscillator velocity of the particles $\beta_\perp \approx 0.15 - 0.2$, and $\mu \approx 0.1$. Then for a gap between the plates $a_0 = 1$ cm, the gain is $C \approx 0.003$. For these values, the parameters of the curves in Fig. 2 correspond to a Bragg structure 170 cm long and 150 cm wide, rippled with a period of 2.8 mm and a depth of 0.05 mm. When ~ 400 kW gyrotron radiation is used as the input signal,[9] the output signal level will reach 4 GW with an efficiency of about 10%.

[1] M. A. Agafonov, A. V. Arzhannikov, N. S. Ginzburg, N. Yu. Peskov, S. L. Sinitsky, A. V. Tarasov, in *Proceedings of the 11th International Conference on High-Power Particle Beams*, *Prague, Czech Republic, 1996,* Vol. 1, p. 213.

[2] M. A. Agafonov, A. V. Arzhannikov, N. S. Ginzburg, V. G. Ivanenko, P. V. Kalinin, S. A. Kuznetsov, N. Yu. Peskov, and S. L. Sinitsky, IEEE Trans. Plasma Sci. **26**, 531 (1998).

[3] N. S. Ginzburg, N. Yu. Peskov, and A. S. Sergeev, Pis'ma Zh. Tekh. Fiz. **18**(9), 23 (1992) [Sov. Tech. Phys. Lett. **18**, 285 (1992)].

[4] N. S. Ginzburg, N. Yu. Peskov, A. S. Sergeev, A. V. Arzhannikov, and S. L. Sinitsky, Nucl. Instrum. Methods Phys. Res. A **358**, 189 (1995).

[5] A. V. Arzhannikov, N. S. Ginzburg, N. Yu. Peskov, S. l. Sinitskiĭ, and A. S. Sergeev, in *Proceedings of the All-Russia Conference on Scientific Plans MNTP ''Microwave Physics,''* Nizhniĭ Novgorod (1999), p. 21.

[6] N. S. Ginzburg, N. Yu. Peskov, A. S. Sergeev, A. D. R. Phelps, and G. R. M. Robb, IEEE Trans. Plasma Sci. **24**, 770 (1996).

[7] V. L. Bratman, G. G. Denisov, N. S. Ginzburg, and M. I. Petelin, IEEE J. Quantum Electron. **QE-19**, 282 (1983).

[8] N. S. Ginzburg, N. Yu. Peskov, and A. S. Sergeev, Radiotekh. Elektron. **40**, 401 (1995).

[9] V. E. Myasnikov, S. V. Usachev, M. V. Agapova *et al.*, in *Digest of the 23rd Internationl Conference on Infrared and Millimeter Waves*, Colchester, UK (1998), p. 24.

Translated by M. E. Alferieff

Influence of phase hardening on transition broadening in a $(1-x)\text{NaNbO}_3-x\text{LiNbO}_3$ system

I. V. Pozdnyakova, L. A. Reznichenko, and V. G. Gavrilyachenko

Research Institute of Physics, Rostov State University
(Submitted May 12, 1999)
Pis'ma Zh. Tekh. Fiz. **25**, 1–4 (October 26, 1999)

Dielectric methods are used to study phase-transition broadening in a $(1-x)\text{NaNbO}_3-x\text{LiNbO}_3$ system. It is observed that the lowest values correspond to regions of transition between implanted solid solutions and substitutional solid solutions with $0.05 \leqslant x \leqslant 0.07$. It is shown that the degree of broadening of the phase transition may be varied by phase hardening. © *1999 American Institute of Physics.* [S1063-7850(99)01610-9]

It is well-known that some broadening of the phase transition is observed in any ferroelectric ceramic. One of the main factors responsible for this broadening are extended structural defects. The phase hardening effect, i.e., an irreversible buildup of crystal-structure defects as a result of cyclic phase transitions, may be used to influence the degree of broadening.

The samples used for our investigations were $(1-x)\text{NaNbO}_3-x\text{LiNbO}_3$ solid solutions with $0 \leqslant x \leqslant 0.14$. This system is interesting because its phase diagram for $0 \leqslant x \leqslant 0.14$ contains eleven phase states, including five morphotropic regions,[1] and many compositions based on this system have extensive practical applications.[2] Although many studies have been devoted to this system, no quantitative estimates have been made of the phase-transition broadening. The aim of the present study is to determine the degree of phase-transition broadening and the possibility of varying this by phase hardening.

Ceramic samples of $(1-x)\text{NaNbO}_3-x\text{LiNbO}_3$ were prepared by solid-phase synthesis followed by hot pressing. We studied the dielectric characteristics of 44 compositions in the range $0 \leqslant x \leqslant 0.145$ with an average step $\Delta x \approx 0.003$. Ten compositions with an average interval $\Delta x \approx 0.015$ underwent thermal cycling (up to twenty successive phase-transition cycles). The samples used for the measurements were disks between 8 and 10 mm in diameter and 1 mm thick. Electrodes were deposited by brazing silver paste. The experimental setup could be used to obtain curves of $\varepsilon(T)$ by a bridge method ($f=20$ kHz, $E_\sim=10$ V/cm) in the temperature range 20–600°. The phase-transition broadening D was determined by a method described in Ref. 3 using the profile of the $\varepsilon(T)$ curves. This method was chosen because these compositions have weakly broadened phase transitions [at temperatures above T_C the behavior of the permittivity obeys the Curie–Weiss law with the constant $C_W=(2-3.5) \times 10^5$ °C] which made it difficult to use other methods of estimating the broadening, such as those described by Gridnev and Popov.[4]

The results are plotted in Figs. 1 and 2. Figure 1 shows typical curves of the phase-transition broadening D as a function of the number of cycles n for samples with various

n. For all these compositions the curves of $D(n)$ have a minimum for $n_{\min}=3-8$. As n increases, the phase-transition broadening increases continuously, saturating at $n=20$. Figure 2 gives the phase-transition broadening after the first cycle and the number of the cycle with the minimum broadening as a function of the LiNbO₃ concentration, $D_1(x)$ and $n_{\min}(x)$, respectively. It can be seen that these dependences correlate with the minima of $D_1(x)$ and $n_{\min}(x)$ being observed in the range $0.05 \leqslant x \leqslant 0.07$. Although the broadening behavior is qualitatively similar for all compositions, the minimum of $D(n)$ for $0.05 \leqslant x \leqslant 0.07$ is less sharp and (like the minimum of T_C) is achieved for small $n_{\min}$ ($n_{\min}=3-4$).

These effects may be attributed to interaction between various types of defects: between intrinsic (determined by the cation–anion composition) and biographical defects (associated with the ceramic preparation process), forming the initial defect matrix, and defects formed as a result of mechanical stresses accompanying the phase transition, i.e., phase hardening defects.

Since the minimum values of D_1 and $n_{\min}$ are observed for $0.05 \leqslant x \leqslant 0.07$, in the region of transition from implanted to substitutional solid solutions,[1] and D_1 then remains low, we can postulate that these solid solutions have a higher
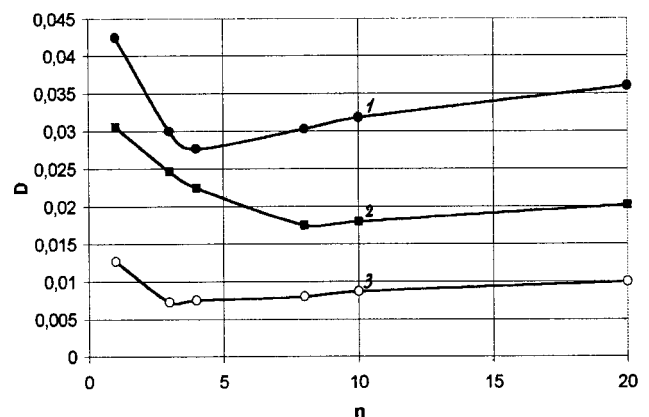

FIG. 1. Phase-transition broadening D as a function of the number of cycles n for various x: *1* — $x=0.03$, *2* — $x=0.1175$, and *3* — $x=0.07$.
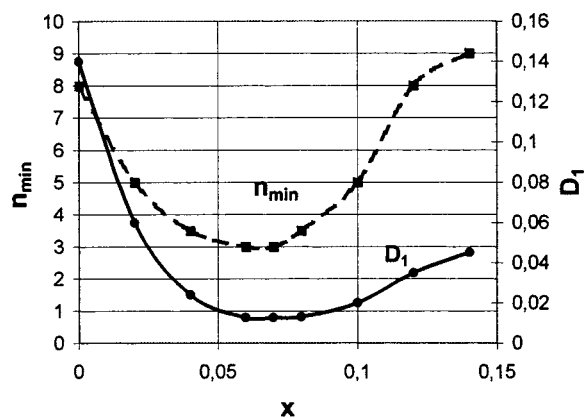
FIG. 2. Phase-transition broadening after the first cycle D_1 and cycle number n_{min} for which the minimum broadening is achieved as a function of the concentration x in a $(1-x)\text{NaNbO}_3-x\text{LiNbO}_3$ system.

degree of structural perfection (a lower dislocation and/or point defect density) and they also have fairly high sintering temperatures compared with the other compositions whereas low sintering temperatures are typical of highly defective samples. The slight increase in D_1 for $x \geqslant 0.06$ is caused by an increase in the difference between the effective sizes of the (Na, Li) cations and Na cations as the LiNbO_3 content

increases[5] and also by the similarity of the morphotropic transition for $x \sim 0.1$ (Ref. 1).

It therefore follows that the phase-transition broadening in $(1-x)\text{NaNbO}_3-x\text{LiNbO}_3$ ceramic samples depends on the ratio of the components. For compositions with $0.05 \leqslant x \leqslant 0.07$ the broadening increases monotonically after three or four cycles whereas for all the others it increases after 6–8 cycles. Despite being highly sensitive to external influences as a result of the small ionic radii of the cations, the system largely demonstrated highly stable dielectric properties under such a strong influence as thermal cycling: no significant phase-transition broadening occurred even after the twentieth cycle.

[1] L. A. Shilkina, I. V. Pozdnyakova, and L. A. Reznitchenko, in *Book of Abstracts of IMFS-8*, Rostov-on-Don, 1998, pp. 190–191.
[2] L. A. Reznichenko and L. A. Shilkina, Izv. Akad. Nauk SSSR, Ser. Fiz. **39**, 1118 (1975).
[3] J. Dudek, M. F. Kupriyanov, and G. N. Konstantinov, Ferroelectrics **81**, 249 (1988).
[4] S. A. Gridnev and S. V. Popov, Izv. Ross. Akad. Nauk Ser. Fiz. No. 2, 61 (1997).
[5] A. A. Bokov, Zh. Éksp. Teor. Fiz. **111**, 994 (1997) [JETP **84**, 1817 (1997)].

Translated by R. M. Durham

Stable pinch in the SPEED 2 plasma focus

W. Kies, G. Decker, U. Berntien, Yu. V. Sidel'nikov, D. A. Glushkov, K. N. Koshelev,
D. M. Simanovskiĭ, and S. V. Bobashev

Institut für Experimentalphysik, Heinrich-Heine-Universität, Düsseldorf, Germany;
Institute of Spectroscopy, Russian Academy of Sciences, Troitsk;
A. F. Ioffe Physicotechnical Institute, Russian Academy of Sciences, St. Petersburg

Conditions of discharge generation in deuterium doped with heavy argon and xenon gases were investigated in experiments in the SPEED 2 plasma focus in the micropinch plasma compression mode and in the stable plasma formation regime. An extensive arsenal of diagnostic techniques, including spectral techniques in the soft- x-ray range with temporal, spatial, and energy resolution was used to achieve a controlled transition from one regime to another. The experimental data are consistent with the assumption that the discharge is stabilized by a gyromagnetic deuteron acceleration mechanism. © *1999 American Institute of Physics.*
[S1063-7850(99)01710-3]

Studies of pinching regimes in the SPEED 2 plasma focus have shown that when heavy impurities (Ar, Kr) are added to the working gas (deuterium), the so-called "micropinch plasma compression mode" (MPM) occurs most frequently.[1–3] This regime is characterized by the formation of short-lived (having subnanosecond lifetimes) plasma structures emitting intensely in the x-ray range, having dimensions between ten and several tens of micrometers. It was shown[2,3] that micropinching is the result of the buildup of necking instabilities under conditions of strong radiative losses to line radiation from multiply charged ions of heavy elements (radiative collapse model).[4] This effect appeared to be fairly general and is observed in various types of axial discharges (vacuum spark, Z pinch, exploding wires, and so on).[5]

However, in some experiments with added neon and also at low argon concentrations, time-integrated images of the plasma revealed a spatially continuous pattern without any breakdown into micropinches.[6,7] Figure 1 shows an example of two different types of pinching, with the formation of micropinches and with a continuous plasma column. Given the absence of time-resolved techniques in these experiments, the question as to whether the observed homogeneous plasma column is the result of its simultaneous stabilization over a fairly considerable length along the discharge axis remained unresolved. A homogeneous image could also appear as a result of a fairly trivial effect, involving the time integration of a moving discharge "focus," i.e., the site of successive convergence of plasma sheaths on the axis, known as the "zippering" effect.

Quite clearly, an operating regime in which a homogeneous stabilized pinch is formed is of considerable interest and may have various practical applications. The present paper examines the choice of these two possibilities and reports a detailed study of the stable column mode (SCM). A study of the possibility of achieving a controlled transition from one pinching regime to another was of particular interest.

The SPEED 2 plasma focus was described in detail in an earlier study.[8] The total discharge energy is up to 70 kJ, the voltage 180 kV, and the current 1.5 MA. The plasma discharge is initiated at the surface of an insulator and then evolves in a deuterium atmosphere with a density of $10^{17}\,\mathrm{cm}^{-3}$. A fast valve is used to inject heavy gas (neon or argon) through a hole in the anode, synchronized with the deuterium discharge. The gas is injected several milliseconds before the beginning of the discharge and forms a conical gas jet along the Z axis, perpendicular to the surface of the anode. The injected jet has a diameter of around 1 cm at the anode surface and a linear density of the order of $10^{17}\,\mathrm{cm}^{-1}$ which decreases slowly along the Z axis. The axisymmetric ionized deuterium plasma sheath usually reaches the heavy neutral gas formed at the center of the jet around 50 ns before complete compression on the discharge axis. The plasma compression time on the discharge axis depends on the linear density of the heavy gas jet which is determined by the initial below-valve pressure p and the time delay τ between opening the gas-injection valve and the discharge initiation time in the deuterium. It was observed that the SCM regime tends to appear when τ and p decrease to $\tau \approx 5-6$ ms and $p \approx 3-4$ bar. The MPM regime appears when the delays increase to 7–12 ms and the below-valve pressure increases to 8–10 bar.

A characteristic feature of these investigations is the extensive arsenal of plasma diagnostic techniques used. In addition to recording the conventional plasma electrotechnical parameters such as the current derivative and the pinch voltage, we also recorded the neutron flux in the energy range between 2.2 and 2.8 MeV with a time resolution of at least 10 ns. The plasma radiation was investigated using various x-ray diagnostic techniques. A pinhole camera with apertures between 20 and 100 μm in diameter and an array of various filters was used to obtain an image of the plasma over a wide energy range between 1 and 10 keV with a spatial resolution of 10 μm on Kodak DEF2 x-ray film. Figure 1 shows an
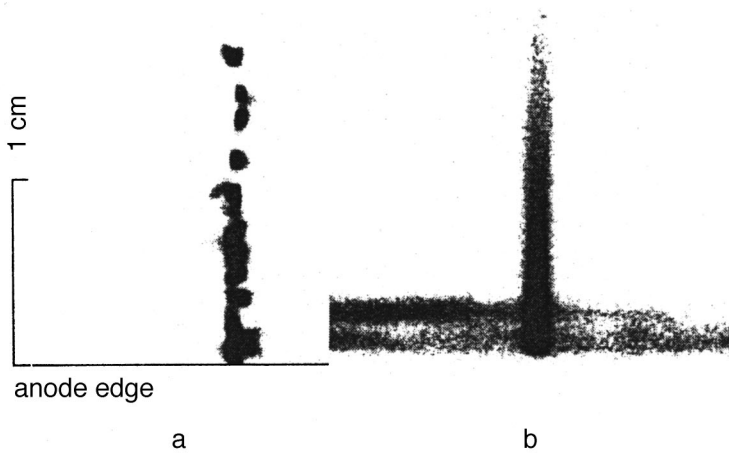
FIG. 1. Time-integrated images of the plasma from its self-radiation in the range $\lambda < 1$ nm: a — MPM micropinch discharge mode in deuterium–argon plasma (typical micropinch size 10 μm), b — stable SCM discharge mode in deuterium–neon plasma (pinch radius 1 mm).

image of the pinch integrated over the discharge time at wavelengths shorter than 1 nm, which illustrates the two plasma compression regimes: MPM in argon (a) and SCM in neon (b).

The plasma radiation spectra were recorded using a compact CAP-crystal x-ray focusing spectrograph at wavelengths between 0.8 and 1.5 nm with the spectral resolution $\lambda/\Delta\lambda = 2 \times 10^4$. By inserting an additional slit and suitably aligning the spectrograph, it was possible to record the spectra with a spatial resolution of 1 mm. A time resolution of 10 ns was achieved by recording the spectra using microchannel image detectors. Figure 2 shows an example of the discharge plasma spectrum in neon for the SCM regime in the range 0.8–1.5 nm for the plasma on the discharge axis. The spectra containing Lyman-series transitions of hydrogen-like neon NeX and the corresponding recombination continuum can be used to estimate the main plasma parameters, the temperature T_e and the electron density N_e. The plasma density on the discharge axis $N_e = 2 \times 10^{20}$ cm^{-3} was obtained from the Stark broadening of the high transitions in the hydrogen-like neon series. The plasma temperature $T_e \approx 250$ eV was estimated from the decay of the recombination hydrogen continuum ($\lambda < 0.9$ nm). A similar temperature was obtained in-

dependently from the intensity ratio of the resonant Ly$_a$ transition of $1s-2p$ H-like neon and the $1s2p(^1P_1)-2p^2(^1D_2)$ dielectronic satellite. The most convincing demonstration of the existence of a stable pinch regime was obtained using a multiframe pinhole camera based on a multichannel plate (MCP) detector. Figure 3 shows an image of a neon plasma column from its self-radiation in the SCM regime in the spectral range $\lambda < 2$ nm. The exposure time for each frame was 5 ns and the time delay between the frames was 5 ns. Additional information was obtained using a Kentech x-ray streak camera with a time resolution of 100 ps which can record the discharge dynamics along the radius or along the Z axis in the spectral range of the plasma radiation $\lambda < 1$ nm. Both methods yield estimates of the plasma lifetime in the SCM mode $t > 30$ ns. A spectrally resolved, frame-by-frame image of the plasma in the SCM mode was obtained by using an x-ray optical objective with a cylindrical multilayer x-ray mirror (W/Sc) having the period $d = 1.18$ nm (MLM objective) and the spectral resolution $\lambda/\Delta\lambda = 100$. This device incorporated a temporal MCP detector with 3 ns time resolution. These experiments showed that the zone of emission at the wavelength of the resonant
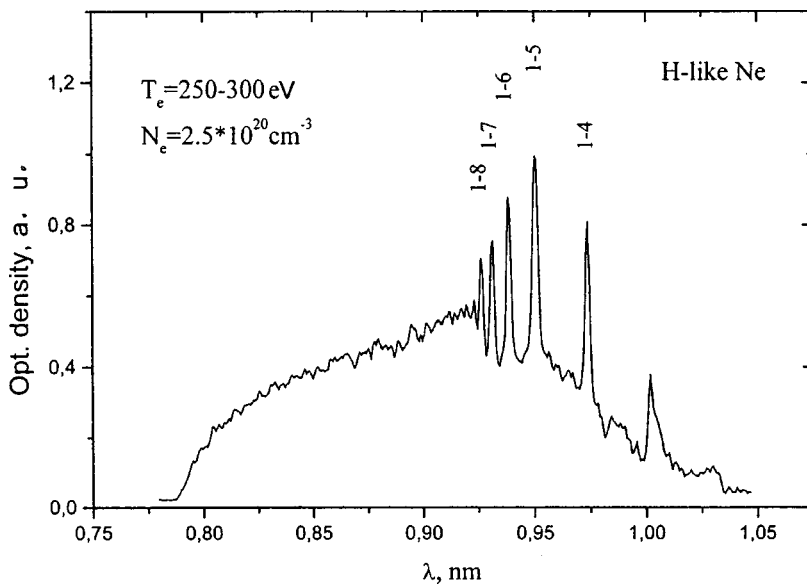

FIG. 2. Plasma radiation spectrum on axis of neon discharge for the SCM regime between 20 and 10 ns before maximum compression. Exposure time 10 ns.
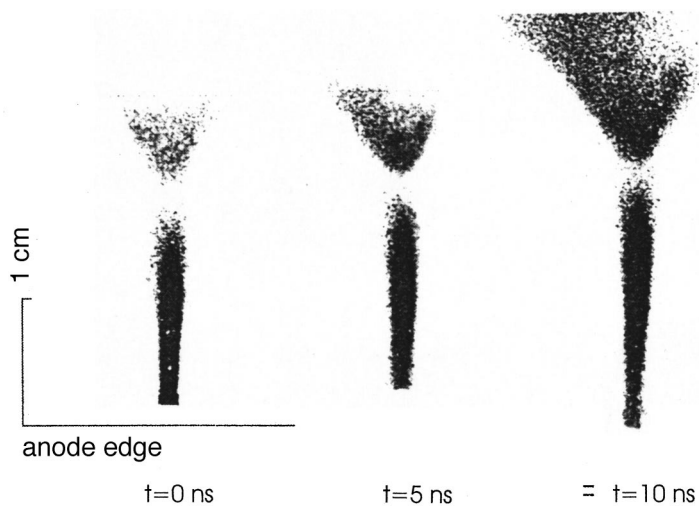
FIG. 3. Plasma images in stable SCM discharge mode in neon at $\lambda < 2$ nm obtained using a time-resolved multiframe pinhole camera with an MCP detector. The time $T = 0$ corresponds to maximum compression of the plasma. The delay between the frames is 5 ns and the exposure of each frame is 5 ns.

line of the hydrogen-like neon line NeX ($\lambda = 1.21$ nm) was stable for more than 30 ns. A substantial difference for these two compression regimes (MPM and SCM) was also observed on oscilloscope traces of the derivative of the discharge current (dI/dt) and on curves of the neutron yield as the discharge develops. In the SCM regime the singularity on the dI/dt curve at the instant of convergence of the discharge plasma on the axis is considerably stronger than that for the MPM regime. For the SCM mode, a higher (between two and ten times) neutron yield is observed, the neutron pulse has a large half-width, and the curve giving the time dependence of the neutron yield shows considerably less structuring.

Thus, these experimental results confirm that when heavy neon and argon gases were injected in a fast dynamic discharge in SPEED 2 at 1.5 MA, a stable homogeneous pinch of length 10–20 mm and radius $\leqslant 1$ mm was observed for the first time. Its lifetime was several tens of nanoseconds which is longer than the magnetic confinement time of the plasma (several nanoseconds) and also exceeds the time taken for propagation of the pinching focus along the discharge axis (~ 10 ns) at a moderate zippering velocity of the order of 10^8 cm/s.

From an analysis of the conditions for the formation of the SCM regime we concluded that a necessary condition is the creation of a high plasma energy density in the fast deuterium current sheath. For SPEED 2 these conditions can be established by reducing the initial deuterium pressure in the chamber and also by reducing the number of injected neon or argon gas particles by varying the below-valve pressure and the valve opening time. Linear Z pinches in a plasma generally tend to develop macroinstability ($m = 0$ mode) in the plasma column which, under conditions of high radiative losses to multiply charged ions, leads to the formation of micropinches (MPM discharge regime). It was shown by Deutsch and Kies[9,10] that in dynamic pinches with a compressible current sheath, the formation of neckings can be avoided as a result of the generation of fast accelerated deuterium ions (''runaway deuterons'') formed by interaction between deuterons and the magnetic piston of the sheath, known as the gyromagnetic acceleration mechanism. The presence of accelerated deuterons in the peripheral zone of the sheath can stabilize the formation of a plasma column having a lifetime of up to several tens of nanoseconds, leading to a stable SCM discharge regime. Calculations show that in this case, the evolution of the SCM mode should be characterized by high energy density, high compression velocity, and low radiative losses in the current sheath plasma. These conditions of plasma column stabilization are achieved in high-current, low-pressure discharges using a light working gas such as deuterium. Conversely, discharges having a comparatively low energy density in the plasma sheath, low compression velocity, and high energy losses to heavy-ion line radiation tend to develop the micropinch MPM mode.

Summarizing these results, we note that for a fast dynamic pinch (SPEED 2) the discharge can develop in two regimes: in the micropinch mode (MPM), when the initial deuterium pressure is comparatively high and a large number of neon or argon atoms are injected, and the stabilization mechanism is suppressed by rapid thermalization of the accelerated ions, and in the stable SCM pinch regime when the initial deuterium pressure is low and few particles are injected, and the mechanism of stabilization by accelerated ions is effective. The experimental observation of an increased neutron yield and the change in the time structure of the neutron pulse, and also the nature of the singularity on the curve of the current derivative are consistent with the assumption that the pinch is stabilized by the gyromagnetic acceleration of deuterons.

[1] W. Kies, B. Lucas, P. Rowekamp, F. Schmitz, G. Ziethen, and G. Decker, Plasma Sources Sci. Technol. **7**, 21 (1998).
[2] G. Decker, W. Kies, R. Nadolny, P. Röwekamp, F. Schmitz, G. Ziethen, K. N. Koshelev, Yu. V. Sidelnikov, and Yu. V. Sopkin, Plasma Sources Sci. Technol. **5**, 112 (1996).
[3] S. V. Bobashev, D. M. Simanovskii, Yu. Ya. Platonov, P. Rowekamp, G. Decker, and W. Kies, Plasma Sources Sci. Technol. **5**, 578 (1996).
[4] V. V. Vikhrev, V. V. Ivanov, and K. N. Koshelev, Fiz. Plazmy **8**, 1211 (1982) [Sov. J. Plasma Phys. **8**, 688 (1982)].

[5] K. N. Koshelev and N. R. Pereira, J. Appl. Phys. **69**, R21 (1991).

[6] S. V. Bobashev, D. M. Simanovskiĭ, G. Decker, W. Kies, P. Röwekamp, Ch. Zoll, and U. Berntien, Pis'ma Zh. Tekh. Fiz. **23**(8), 53 (1997) [Tech. Phys. Lett. **23**, 316 (1997)].

[7] R. Lebert and A. Engel, J. Appl. Phys. **78**, 6414 (1995).

[8] G. Decker, W. Kies, M. Malzig, C. van Calker, and G. Ziethen, Nucl. Instrum. Methods Phys. Res. A **249**, 477 (1986).

[9] D. Deutsch and W. Kies, Plasma Phys. Controlled Fusion **30**, 263 (1988).

[10] D. Deutsch and W. Kies, Plasma Phys. Controlled Fusion **30**, 921 (1988).

Translated by R. M. Durham

Deformations and overlap of instability zones in the Mathieu–Hill equation

A. I. Grigor'ev and A. S. Golovanov

P. G. Demidov State University, Yaroslavl'

A numerical analysis of the Mathieu–Hill equation describing the time evolution of the amplitudes of capillary waves at the interface between two liquids, the upper moving relative to the denser lower liquid at a time-dependent velocity, is used to show that for certain values of the characteristic physical parameters, the zones of unstable amplitude growth become deformed and overlap to form a single, singly connected instability zone. © *1999 American Institute of Physics.* [S1063-7850(99)01810-8]

In the problem of the stability of a tangential discontinuity between two immiscible ideal liquids of different densities ρ_1 and ρ_2, each filling a semi-infinite half-space, and the upper liquid moving at the time-varying velocity $U=U\{t\}$ parallel to a charged interface having the constant surface charge density σ, the differential equations describing the time evolution of the capillary wave amplitudes are Mathieu–Hill equations with time-dependent coefficients. We know from theory that the Mathieu–Hill equations have discrete zones in which the solutions are unstable.[1–3] Determining the form of these zones for the electrohydrodynamic problem under discussion is of interest for a wide range of academic, technical, and technological applications of electrohydrodynamic instabilities.[4]

1. Let us assume that the velocity fields of the upper and lower liquids are $\psi_1(\mathbf{r},t)$ and $\psi_2(\mathbf{r},t)$, respectively. The mathematical formulation of the problem of studying the time evolution of the capillary wave amplitudes in this system in a Cartesian coordinate system where the XY plane coincides with the unperturbed interface of the media and the Z axis is directed downward in the direction of the gravitational force, then has the form:[5,6]

$$\Delta\psi_j=0; \quad j=1,2;$$

$$z\Rightarrow-\infty \quad \psi_1-xU(t)\Rightarrow\text{const}=0;$$

$$z\Rightarrow\infty\;\psi_2\Rightarrow\text{const}=0;$$

$$z=\xi(x;t); \quad \frac{\partial\psi_1}{\partial z}\approx U\frac{\partial\xi}{\partial x}+\frac{\partial\xi}{\partial t}; \quad \frac{\partial\psi_2}{\partial z}\approx\frac{\partial\xi}{\partial t};$$

$$\rho_1\frac{\partial\psi_1}{\partial t}+\rho_1 g\xi+\frac{1}{2}\rho_1[(\nabla\psi_1)^2-U^2(t)]$$

$$=\rho_2\frac{\partial\psi_2}{\partial t}+\rho_2 g\xi+4\pi\sigma^2 k\xi-\alpha\frac{\partial^2\xi}{\partial x^2},$$

where $\xi(x,t)$ is the perturbation of the interface caused by the thermal capillary wave motion and $\mathbf{U}=\mathbf{U}(t)$ is the time-dependent velocity of the upper liquid relative to the lower one which is uniform along the x and z coordinates. The

direction of the vector $\mathbf{U}$ determines the orientation of the X axis, α is the surface tension of the interface, and k is the wave number.

If we assume that

$$\mathbf{U}(t)=\mathbf{U}_0+\mathbf{U}_* \cos\omega_0 t \quad (\mathbf{U}_0\|\mathbf{U}_*),$$

the differential equation describing the time evolution of the amplitudes of fixed modes of the thermal capillary waves is then given by:

$$\frac{\partial^2\zeta}{\partial t^2}+\zeta[F(k)-D(k)\cdot\cos\omega_0 t+L(k)\cdot\cos^2\omega_0 t]=0, \quad (1)$$

$$F(k)\equiv\frac{k}{(\rho_2+\rho_1)}\left[g(\rho_2-\rho_1)+\alpha k^2-4\pi\sigma^2 k-k\rho_1 U_0^2\right.$$

$$\left.+kU_0^2\frac{\rho_1^2}{(\rho_2+\rho_1)}\right],$$

$$L(k)=k^2\frac{\rho_1\rho_2}{(\rho_2+\rho_1)^2}U_*^2, \quad D(k)\equiv 2L(k)U_0/U_*.$$

This equation is the Mathieu–Hill equation which, depending on the relationship between the coefficients F, D, L, and the frequency ω_0, can either have parametrically stable or parametrically unstable solutions which increase exponentially with time. Moreover, for certain values of the parameters $[F(k)\leq 0$ and $\omega_0=0]$ it also follows from Eq. (1) that Tonks–Frenkel and Kelvin–Helmholtz instabilities may occur in the system being analyzed.

2. In Eq. (1) we now convert to dimensionless variables in which the capillary constant of the lower liquid, the density of the lower liquid, and the frequency ω_0 of the periodic external action on the interface are unity, and retaining the previous notation, we rewrite Eq. (1) in the form:

$$\frac{\partial^2\zeta}{\partial t^2}+\zeta[\delta-\alpha\cdot 2\varepsilon\cos t+2\varepsilon\cos 2t]=0; \quad (2)$$

$$\alpha=4U_0/U_*; \quad \delta=F(k)+0.5L(k); \quad \varepsilon=L(k)/4.$$

For $\alpha=0$, Eq. (2) yields the Mathieu equation for which the position of the first few zones of instability of the solu-
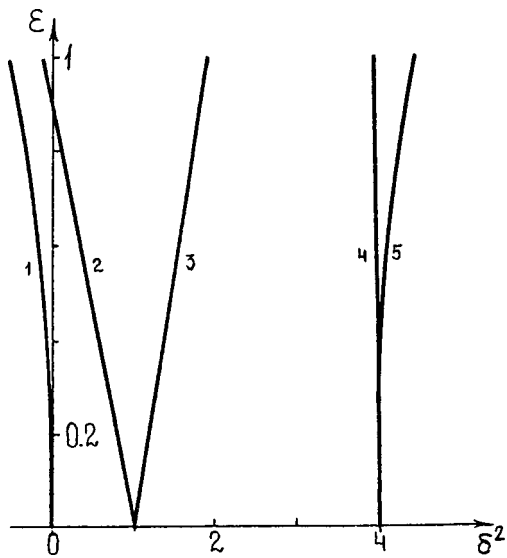
FIG. 1. Boundaries of instability zone in the plane of the parameters δ, ε for Eq. (2) for $\alpha = 0$: 1 — right-hand boundary of instability zone at $\delta^2 = 0$, left-hand boundary at $-\infty$; 2 — left-hand boundary of instability zone at $\delta^2 = 1$; 3 — right-hand boundary of instability zone at $\delta^2 = 1$; 4 — left-hand boundary of instability zone at $\delta^2 = 4$, and 5 — right-hand boundary of instability zone at $\delta^2 = 4$.

tions calculated by expanding in terms of the small dimensionless parameter ε (as described in detail in Ref. 7) is shown in Fig. 1. It can be seen that the apexes of the instability zones begin on the abscissa at integer values of the parameter δ^2, i.e., $\delta^2 = 0, 1, 2, \ldots$.

Equation (2) contains another dimensionless parameter α which characterizes the ratio of the constant and variable components of the entire velocity field of the upper medium. As the parameter α increases, the instability zones begin to deform and for a certain value of α the left and right boundaries of the $\delta^2 = 1$ zone intersect, as shown in Fig. 2 which was obtained for $\alpha = 1,3$. The geometric position of the points located between the boundary curves of this zone both below and above the point of intersection (including the
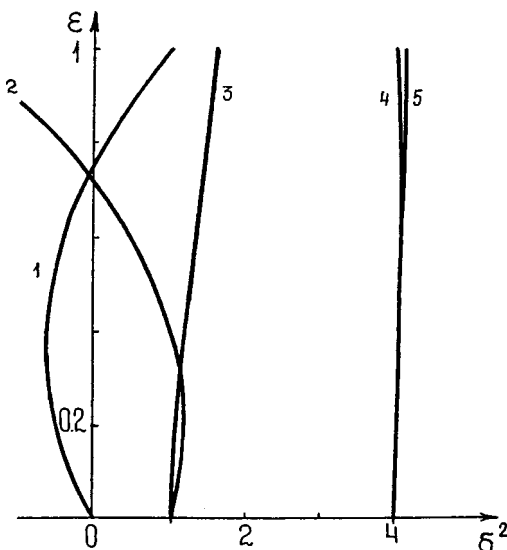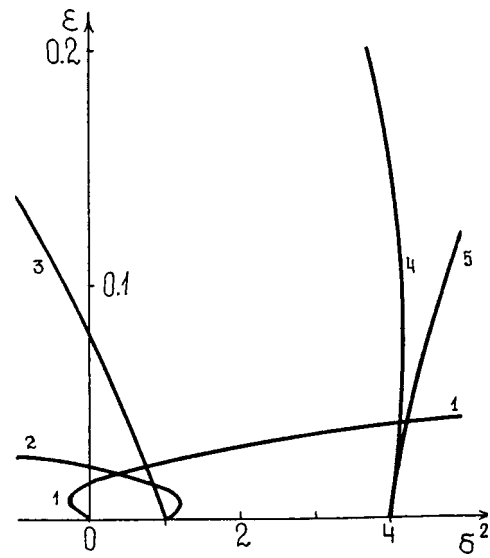

FIG. 3. The same dependences as in Fig. 2 for $\alpha = 6$.

point of intersection) corresponds to periodic instability of the solution of Eq. (2) with exponentially increasing amplitude, as was confirmed by direct calculations using Eq. (2).

A further increase in the parameter α leads to overlap of neighboring instability zones and results in the formation of a single zone on the plane of (δ, ε) values in which any pair of δ and ε values correspond to unstable solutions of Eq. (2), as can be seen from Fig. 3 which was obtained for $\alpha = 6$.

From the mathematical point of view, the deformation and overlap of the various instability zones is caused by the difference in the signs of $\cos t$ and $\cos 2t$ in Eq. (2). From the physical point of view, the formation of a single zone of instability of Eq. (2) as the parameter α increases can be attributed to the increasing role played by the Kelvin–Helmholtz vibrational instability in the overall instability pattern. This instability is established and becomes dominant at fairly high velocities U_0 (at fairly high α) and embraces the entire wave spectrum.[8]

Conclusions

3. The Mathieu–Hill equation describing the time evolution of the amplitudes of capillary waves at the charged interface between two liquids, the upper moving at a time-dependent velocity relative to the lower, denser liquid, has unstable solutions typical of all three possible types of instability which may occur in this system. When the physical parameters of the problem are varied, the discrete zones of unstable amplitude growth typical of parametric instability become deformed and overlap, forming a single, singly-connected zone of instability in which the Kelvin–Helmholtz instability plays the dominant role.

FIG. 2. The same dependences as in Fig. 1 for $\delta^2 = 1$, $\alpha = 1,3$.

[1] *Handbook of Special Functions*, edited by M. Abramowitz and I. A. Stegun (Dover, New York, 1965; Nauka, Moscow, 1979, 832 pp.).
[2] S. O. Shiryaeva and A. I. Grigor'ev, Zh. Tekh. Fiz. **62**(11), 49 (1992) [Sov. Phys. Tech. Phys. **37**, 1071 (1992)].
[3] D. V. Lyubimov, M. V. Khenner, and M. M. Shots, Izv. Ross. Akad. Nauk Ser. Mekh. Zhidk. Gaza No. 3, 25 (1998).

[4] A. I. Grigor'ev and S. O. Shiryaeva, Izv. Ross. Akad. Nauk Ser. Mekh. Zhidk. Gaza No. 3, 3 (1994).

[5] L. D. Landau and E. M. Livshitz, *Electrodynamics of Continuous Media*, (2nd ed Pergamon Press, Oxford, 1984; Nauka, Moscow, 1982), 620 pp.

[6] V. G. Levich, *Physicochemical Hydrodynamics* Fizmatgiz, Moscow (1959), 699 pp.

[7] A. H. Nayfeh, *Introduction to Perturbation Techniques* (Wiley, New York, 1981; Mir, Moscow, 1984), 535 pp.

[8] L. D. Landau and E. M. Lifshitz, *Fluid Mechanics*, (Pergamon Press, Oxford, 1987; Nauka, Moscow, 1986), 733 pp.

Translated by R. M. Durham

Characteristic electron energy losses in organic PTCDA films

S. A. Komolov, N. B. Gerasimova, A. G. Sidorenko, Yu. G. Alyaev, and V. A. Novolodskiĭ

Research Institute of Physics, St. Petersburg State University
(Submitted July 1, 1999)
Pis'ma Zh. Tekh. Fiz. **25**, 19–24 (October 26, 1999)

Studies are made of the characteristic energy losses of slow electrons during the formation of thin PTCDA films on a ZnO(0001) surface. It is shown that at low primary electron energies (<100 eV) the energy loss spectrum ($E_n = 3.0$, 6.3, and 15 eV) reflects the structure of the transitions between the valence band and the conduction band. As the primary electron energy increases, energy losses to the excitation of plasma oscillations become dominant ($\hbar\omega_1 = 6$ eV — excitation of a π-plasmon and $\hbar\omega_2 = 25$ eV — excitation of a σ-plasmon). © *1999 American Institute of Physics.* [S1063-7850(99)01910-2]

Increased interest is now being shown in organic macromolecular films which are promising new materials for applications in nano-, micro-, and optoelectronics. The formation of thin films of perylene-3,4,9,10-tetracarboxylic dianhydride (PTCDA) has been studied on various semiconducting[1,2] and metal[3] substrates in ultrahigh vacuum in connection with the observed capacity of this material to form ordered films. Studies of the electronic structure of PTCDA formed when this is adsorbed are highly relevant because of the possible applications of this material in electrical engineering and microelectronics. This possibility is indicated by the interesting photoelectronic properties of PTCDA, particularly when these large π-bonded molecules are adsorbed on an inorganic crystal substrate. We therefore investigated the formation of PTCDA films on the surface of a ZnO(0001) crystal using secondary electron techniques: total current spectroscopy, Auger spectroscopy, and characteristic electron energy-loss spectroscopy. In the present paper we report new results obtained by measuring the characteristic electron energy losses of thin PTCDA layers on ZnO(0001).

EXPERIMENT

The experiments were carried out in an ultrahigh-vacuum system incorporating a four-grid analyzer which allowed a wide range of electron-spectroscopic techniques to be used to study the surface of the solids. Facilities were also provided for depositing films of the materials being studied *in situ* and measuring the characteristic electron energy loss spectra during the deposition process. A sample heater and electron gun were also installed to purify the surfaces being studied. The heater was designed to provide controlled heating up to 750°C. The temperature was monitored using a Chromel–Alumel thermocouple. PTCDA powder was placed in a Knudsen cell and deposition was carried out at a cell temperature of 250°C after the material had undergone prolonged low-temperature outgassing. The ZnO substrate was preliminarily purified by high-temperature heating to 750°C in vacuum. The surface purity was monitored using the Auger spectrum where the intensities of the zinc (59 eV), oxygen (503 eV), and carbon (272 eV) peaks were in the ratio 100:10:0.1. The films were deposited on room-temperature substrates and the process was monitored using the total current spectra. The total current spectrum of the PTCDA film corresponds to that obtained in Ref. 4. In addition, the film thickness measured in monolayers was monitored using the deposition time. The monolayer deposition time was determined from the change in the work function of the film. During the deposition process the characteristic electron energy loss spectra were recorded at various incident electron energies. These spectra were obtained by recording the dependence $N(E)$. The electron beam current did not exceed 10^{-6} A.

RESULTS AND DISCUSSION

A series of spectra of the characteristic electron losses obtained during the deposition of a PTCDA film at $E_p = 38$ eV is shown in Fig. 1. Also shown is a structure diagram of the PTCDA molecule. Curve *1* gives the spectrum of a pure ZnO(0001) surface. The main peaks are observed at 4.5 eV (a), 7.3 eV (b), and 12.5 eV (c), which shows good agreement with earlier results.[5,6] The spectrum of characteristic electron energy losses of the film forms during the deposition process (curves *2–8* in Fig. 1). It can be seen that at the initial stage of deposition (Fig. 1, curve *2*), peak A is small while peak B has already formed. As the film thickness increases, peak A develops. Figure 1 clearly shows a difference between the intensities of the energy losses of the ZnO surface and the PTCDA film ($A = 3.0$ eV, $B = 6.3$ eV, $C = 15$ eV), which illustrates the difference between the cross section for inelastic scattering of slow electrons for these surfaces. Curve *5* gives the characteristic energy loss spectrum for a relatively thick film obtained 30 min after the beginning of deposition.

As we know,[7] the characteristic energy-loss spectrum contains information on interband transitions from the maxima of the valence-band electronic states to the maxima of the conduction-band electronic states and on collective electronic excitations (plasmons). At low excitation energies (Fig. 1) interband transitions predominate. Data given by Hi-
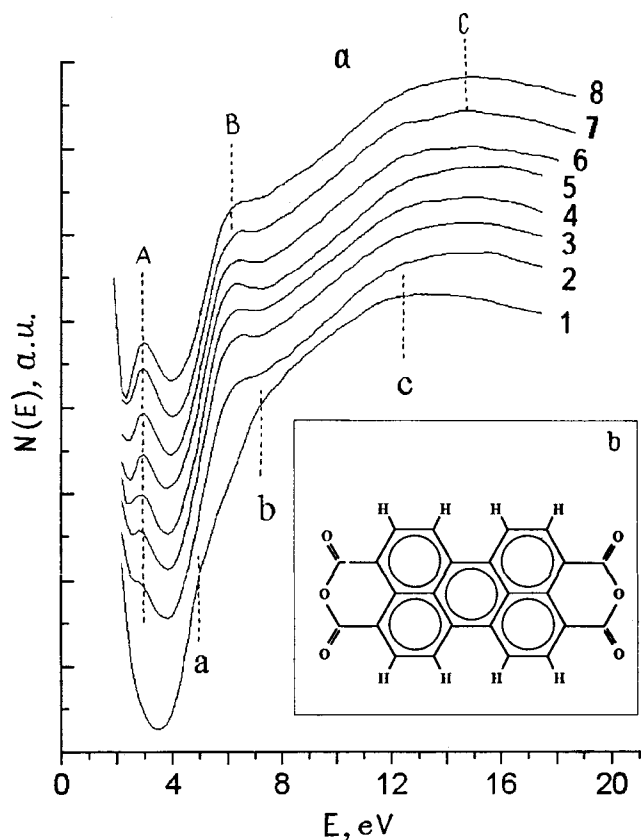
FIG. 1. a — Series of characteristic energy loss spectra obtained during the deposition of PTCDA film on a ZnO(0001) surface. Curve *1* corresponds to the pure substrate surface. Curves *2–8* give the spectra for deposition times of 4, 8, 12, 16, 20, 24, 28, and 32 min; b — schematic representation of PTCDA molecule.

FIG. 2. Characteristic energy loss spectra of PTCDA film obtained for various primary electron energies E_p: *1* — 40, *2* — 55, *3* — 90, *4* — 120, and *5* — 200 eV.

rose *et al.*[2] indicate that near the top of the valence band in PTCDA films there are three density-of-states peaks π_1, π_2, and π_3 at distances of 0.5, 2.5, and 4 eV, respectively, from the top of this band. The π_1 peak only forms finally for a thick film more than 2 ML thick. The density of free states of the PTCDA film was described in Ref. 8. According to this description, near the bottom of the conduction band there are two density peaks of the free states π_1^* and π_2^* at distances of 0.5 and 1.5 eV from the bottom of the conduction band below the vacuum level and two π_3^* and σ^* above the vacuum level, 6 and 17 eV from the bottom of the conduction band. The band gap of the film from data given in Ref. 9 is 2.1 eV. Thus, the losses *A* (3 eV) in Fig. 1 can be attributed to an interband transition from π_1 to π_1^* and these losses only occur in thick films. The *B* peak (6.3 eV) can be ascribed to a transition from π_2 and π_3 to π_1^* and is observed in both thin and thick films, its half-width decreasing as the film thickness increases. The *C* loss peak (12–15 eV) is formed from interband transitions of π_2 and π_3 to π_3^*. As the film thickness increases, the transitions from π_2 and π_3 become significantly resolved.

For a film having a structure similar to PTCDA, Mochida *et al.*[10] showed how the losses to interband transitions change as the π-shell of the carbon film is excited with increasing primary electron energy. The authors put forward two possible interpretations for these changes. One is related
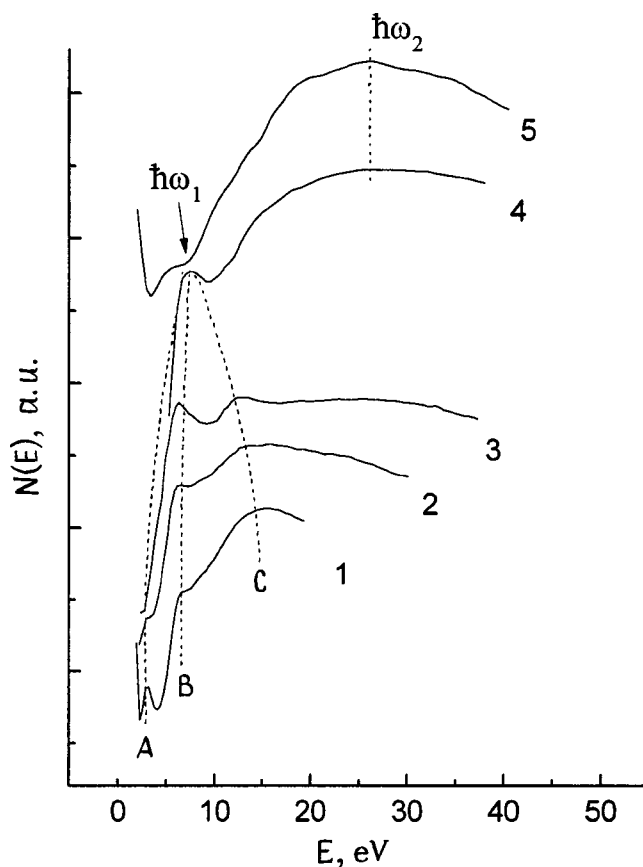
to the depth of penetration of the primary electrons while the other reflects the energy dependence of the inelastic electron scattering cross section. In our study a similar transformation of the losses is observed in the loss spectra of a PTCDA film measured at various primary electron energy losses. Figure 2 shows the characteristic energy loss spectra measured at 38–200 eV. As the primary electron energy increases from 38 to 120 eV, the loss peaks *A*, *B*, and *C* of the interband transitions are transformed to give a single peak $\hbar\omega_1$ at 6 eV. This effect may have a similar interpretation to that put forward in Ref. 10. In our view, there is another possible explanation for this effect. Quite clearly we observe the energy losses characterizing the excitation of a bulk plasmon of the carbon π-shell. This transformation of the energy loss spectrum is evidently related to the dependence of the inelastic scattering cross section on the primary electron energy via the channels for plasmon excitation and interband transitions.

When the energy of the primary electrons increases to 120 eV and above, the loss spectrum reveals a new broad maximum $\hbar\omega_2$ at 25–28 eV. This can be attributed to the excitation of the plasma oscillation of σ-bonded carbon electrons which is a well-known phenomenon for carbon compounds.

[1] U. Zimmermann, G. Shnitzler, N. Kark, and E. Umbach, Thin Solid Films **175**, 85 (1989).

[2] Y. Hirose, W. Chen, E. I. Haskal, S. R. Forrest, and A. Kahn, Appl. Phys. Lett. **64**, 3482 (1994).

[3] K. Glockler, C. Seider, A. Soukopp, M. Sokolowski, E. Umbach, M. Bohringer, R. Berndt, and W.-D. Schneider, Surf. Sci. **405**, 491 (1998).

[4] A. O. Morozov, T. U. Kampen, and D. R. T. Zahn, Surf. Sci. (1999), in press.

[5] R. L. Hengehold and F. L. Pediotty, J. Appl. Phys. **47**, 287 (1976).

[6] S. Komolov, E. Lazneva, and P. J. Moller, Surf. Sci. **323**, 102 (1995).

[7] *Application of Electron Spectroscopy to Surface Analysis*, edited by Kh. Ibakh [in Russian], Riga (1980), 315 pp.

[8] J. Taborski, P. Vaterlein, H. Dietz, U. Zimmermann, and E. Umbach, J. Electron Spectrosc. Relat. Phenom. **75**, 129 (1995).

[9] S. R. Forrest, Chem. Rev. **97**, 1793 (1997).

[10] M. Mochida, T. Shimada, and A. Koma, J. Vac. Sci. Technol. A **15**, 2119 (1997).

Translated by R. M. Durham

Mechanism for thermal destruction of polystyrene grafted to fullerene C_{60}

B. M. Ginzburg, A. O. Pozdnyakov, O. F. Pozdnyakov, and B. P. Redkov

Institute of Problems of Mechanical Engineering, Russian Academy of Sciences, St. Petersburg;
A. F. Ioffe Physicotechnical Institute, Russian Academy of Sciences, St. Petersburg
(Submitted June 29, 1999)
Pis'ma Zh. Tekh. Fiz. **25**, 25–30 (October 26, 1999)

A model is proposed for the thermal destruction of polystyrene covalently bonded to C_{60} and this is used to explain various characteristics of its experimental mass thermograms. © *1999 American Institute of Physics.* [S1063-7850(99)02010-8]

Results of investigations of the thermal destruction of polystyrene-based fullerene-containing systems by thermodesorption mass spectrometry were presented in abbreviated form in Refs. 1–3. It was observed that the grafting of polystyrene chains to fullerene C_{60} strongly influences the thermal destruction of polystyrene and the thermal behavior of C_{60}. However, the mass thermograms of these systems were fairly complex and only very general conclusions could be drawn on the mechanisms for these processes. The aim of the present paper was to analyze all the currently available published data, and as a result it is possible to propose a model for the thermal destruction of polystyrene grafted to fullerene C_{60} which can explain the characteristic features of the experimental mass thermograms. This model may be of general importance for polymers grafted to fullerenes.

In all these studies[1-3] the main object of investigation was fullerene C_{60} with six polystyrene chains grafted to it, having an average molecular mass of 1400–1500. In Ref. 1 the thermal destruction was recorded from the yield of the mass 104 product which corresponds to the polystyrene repeating unit and gives the highest-intensity peak in the overall mass spectrum. The thermal stability of the polymer was characterized by the temperature at the maximum yield rate of thermal destruction products (the temperature of the low-temperature maximum when there were two). The main result of Ref. 1 was that the formation of a covalent bond between C_{60} and polystyrene leads to a reduction in its thermal stability by more than $100\,°C$ (see Figs. 1a and 1b).

Since the mass thermograms of C_{60} with grafted polystyrene revealed two peaks, the first peak shifted by $100\,°C$ toward lower temperatures (compared with that for pure polystyrene) was ascribed to the destruction of polystyrene grafted to C_{60} and the second peak shifted by $\sim 50\,°C$ in the same direction was ascribed to the thermal destruction of free polystyrene, present as an impurity in the initial product, whose concentration could be as high as 15% (Ref. 4). The increase in this peak (curve *2* in Fig. 1b) when fullerene C_{60} was added to the sample would appear to provide indirect confirmation of this assignment of the second peak[1] since this effect was also observed for pure polystyrene (compare curves *1* and *2* in Fig. 1a). However, the intensities of both peaks on the mass thermograms of C_{60} with grafted polystyrene were almost the same, which contradicted the maximum estimate of the impurity fraction as 15%. It could be postu-

lated that this effect is merely apparent: the presence of a high-intensity first peak could distort the true intensity of the neighboring second peak but subsequent investigations[2] refuted the possibility of this interpretation.

The mass spectrometric data obtained in Ref. 2 (Figs. 1c and 1d) were obtained for the same samples as in Ref. 1 but the thermal destruction products were analyzed at a heating rate of 0.08 deg/s as compared with 10 deg/s in Ref. 1. For pure polystyrene the temperature position of the maximum yields of the main thermal destruction products (Fig. 1c) was shifted by $\sim 50\,°C$ toward lower temperatures compared with that at the high heating rate. For fullerene C_{60} with grafted chains merely a shoulder or a low-intensity maximum was observed instead of the low-temperature peak and the main intensity of the yield of thermal destruction products was observed in the second peak. The shoulder or first peak is naturally ascribed to the destruction of the polystyrene grafted to C_{60}, as in Ref. 1. According to the literature[5] the reduction in the thermal stability of the polymer grafted to fullerene C_{60} is a result of the reduced energy of the bond in the β-position to C_{60}, whose breaking initiates the thermal destruction process.

However, the high intensity of the second peak prevents this from being ascribed to the destruction of the comparatively small pure polystyrene impurity. In order to interpret this peak, we can assume that after the weak β-bond has been broken, the product free radicals are only partially destroyed, in which case only some of the products leave the sample. The rest of the low-molecular products form association compounds with the C_{60} fullerene and most of the free polystyrene radicals become deactivated, forming free polystyrene chains. Under subsequent heating, these ''retained'' low-molecular products and chains formed by the deactivation of free radicals yield repeating units and other fragments in the high-temperature peak on the mass thermograms.

Despite the short-lived nature of the elementary events, the overall times of these processes are comparable with the experimental time. This is because the processes are fairly complex and include heat transfer processes, dynamic decay and recombination processes, diffusion processes (these are only important for solid samples), and so on. In view of the comparability with the experimental times, the implementation of these processes should depend on the sample heating
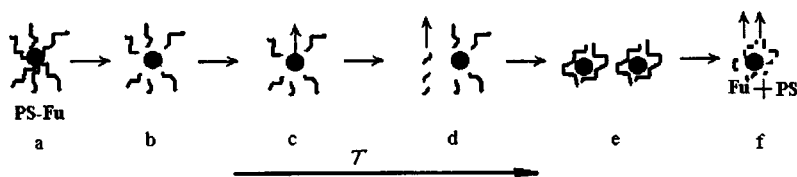
FIG. 1. Diagram to explain characteristics of mass thermograms.

rate. The lower the heating rate, the higher the intensity of these processes. Thus, as the heating rate decreases, the intensity of the yield of thermal destruction products on the two-humped curve should be redistributed toward the second, higher-intensity peak, as was observed experimentally.

Pozdnyakov *et al.*[3] investigated the thermal behavior of C_{60} during the thermal destruction of these systems. The results show that the yield of fullerene C_{60} has two maxima whose temperature positions are similar to the maximum yields of polystyrene destruction products, but are far-removed from the maximum C_{60} yield from pure fullerene film or a mixture of fullerene and polystyrene. These data are important for representing the overall pattern of the thermal destruction processes in these systems. For instance, they indicate that the fullerene yield in the first peak has a higher intensity than the yield of polystyrene destruction products. We can postulate that after the first polystyrene chain has become detached from the fullerene, the subsequent chains become detached more easily and the fullerene radicals are completely released from the grafted chains.

In order to explain the characteristics of the mass thermograms of polystyrene covalently bonded to fullerene C_{60} (Fig. 1a), we propose a model having the following sequence of elementary events: breaking of weak β-bonds (b); yield of some C_{60} molecules released from grafted polystyrene chains, in the first peak (c); destruction of some product polystyrene radicals with the release of various volatile fragments in the first peak (d); deactivation of most radicals and low-molecular polystyrene fragments, formation of association compounds with C_{60} (e); destruction of polystyrene association compounds and its low-molecular fragments with C_{60} and destruction of polystyrene chains accompanied by the release of C_{60} and fragments of polystyrene chains in the second peak (f).

In accordance with the proposed model (even in the absence of any pure polystyrene impurities), fullerene C_{60} with grafted polystyrene chains will always give two-humped mass thermograms for the yield of the main thermal destruction products of polystyrene. The first peak corresponds to the destruction of polystyrene chains grafted to C_{60} while the second corresponds to the thermal destruction of polystyrene chains formed as a result of the deactivation of its radicals and also the release of low-molecular polystyrene fragments retained in association compounds with C_{60}.

The proposed model may also apply to other polymers grafted to fullerenes. The intensity ratio of the two peaks will depend on various factors: the heating rate, the nature of the grafted polymer (the zip length), and the length of the grafted chains.

The relative intensity of the low-temperature peak should increase as the heating rate increases, as the zip length increases, and the molecular mass of the chains decreases. This dependence on the heating rate and the molecular mass of the grafted chains was in fact observed in Refs. 1, 2, and 6: the influence of the heating rate is illustrated in Figs. 2b and 1c and an increase in the molecular mass of the grafted polystyrene chains to ~ 5000 caused a relative decrease in the low-temperature shoulder on the mass thermograms.[6]

According to the proposed model, the following relation should hold:

$$I_1/(I_1+I_2)=Z/M,$$

where I_1 and I_2 are the integral intensities of the low-temperature and high-temperature peaks, respectively, Z is
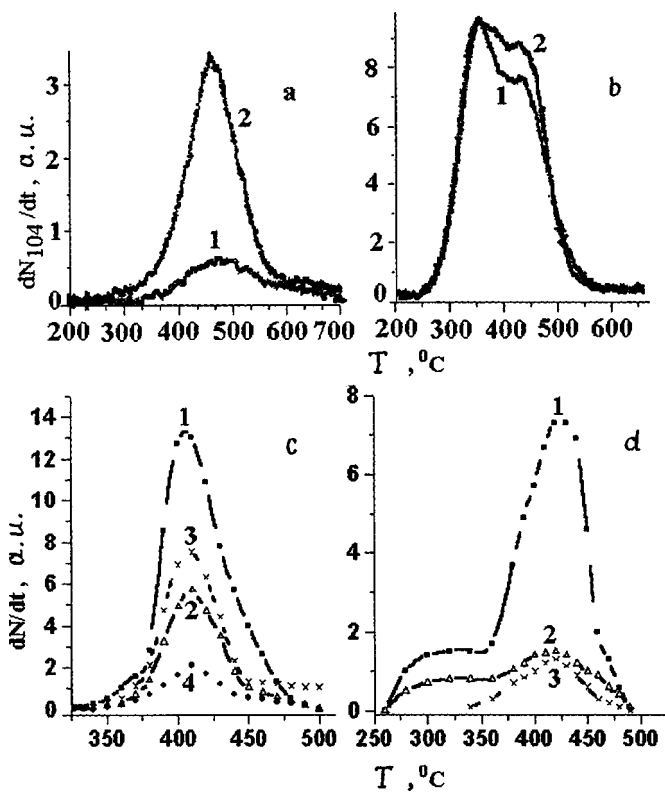
FIG. 2. Temperature dependences of the rate dN/dt of thermal destruction products of polystyrene and polystyrene grafted to C_{60}. Heating rate 10b deg/s (a,b), release of fragments of mass 104 from: polystyrene (a, curve *1*), misture of polystyrene and C_{60} (molecular ratio $\sim$1:1) (a, curve *2*), polystyrene grated to C_{60} (b, curve *1*), and grated plystyrene with added C_{60} (b, curve *2*). Heating rate 0.08 deg/s for polystyrene (c) and polystyrene grated to C_{60} (d), release of fragments of mass 104 (*1*), 91 (*2*), 78 (*3*), and 118 (*4*).

the molecular mass corresponding to the zip length, and M is the molecular mass of the grafted chain. In order to estimate the zip length, we shall use the mass thermogram obtained for the low heating rate (Fig. 1c). We define the value of I_1 as the sum of the areas below all the observed low-temperature peaks (''shoulders''), in this case corresponding to masses 104 and 91, and we define the value of I_2 as the sum of the areas of the high-temperature peaks for all three dominant masses observed: 104, 91, and 78. The value of $I_1/(I_1+I_2)$ is then ≈ 0.22 and the zip length is ≈ 3.16, which agrees with the value of 3.2 for polystyrene from the published data.[7] This result not only confirms the validity of the proposed model but also opens up new possibilities for simple experimental estimates of the zip length.

[1] B. M. Ginzburg, A. O. Pozdnyakov, V. N. Zgonnik, O. F. Pozdnyakov, B. P. Redkov, E. Yu. Melenevskaya, and L. V. Vinogradova, Pis'ma Zh. Tekh. Fiz. **22** (4), 73 (1996) [Tech. Phys. Lett. **22**, 166 (1996)].

[2] E. Yu. Melenevskaya, L. V. Vinogradova, L. S. Litvinova *et al.*, Vysoko-mol. Soedin., Ser. A Ser. B **40** (2), 247 (1998).

[3] A. O. Pozdnyakov, O. F. Pozdnyakov, B. P. Redkov, V. N. Zgonnik, L. V. Vinogradova, E. Yu. Melenevskaya, and B. M. Ginzburg, Pis'ma Zh. Tekh. Fiz. **22** (18), 57 (1996) [Tech. Phys. Lett. **22**, 759 (1996)].

[4] V. N. Zgonnik, E. N. Bykova, E. Yu. Melenevskaya, A. S. Khachaturov, A. I. Kipper, L. V. Vinogradova, I. V. Terent'eva, A. V. Novoselova, E. E. Kever, L. S. Litvinova, and S. I. Klenin, Vysokomol. Soedin., Ser. A Ser. B **38**, 964 (1996).

[5] L. A. Shibaev, T. A. Antonova, L. V. Vinogradova, B. M. Ginzburg, V. N. Zgonnik, and E. Yu. Melenevskaya, Zh. Prikl. Khim. **71** 835 (1998).

[6] L. A. Shibaev, Report on the ''Tribol'' Project of the Russian Scientific and Technical Program ''Fullerenes and Atomic Clusters'' for 1995–1997.

[7] G. G. Cameron and I. T. McWalter, Eur. Polym. J. **6**, 1601 (1970).

Translated by R. M. Durham

Thermomechanical model of crystalline elastoplastic media

V. L. Popov

Institute of Strength Physics and Materials Science, Siberian Branch of the Russian Academy of Sciences, Russia; Department of Theoretical Physics, University of Paderborn, Germany
(Submitted June 16, 1999)
Pis'ma Zh. Tekh. Fiz. **25**, 31–38 (October 26, 1999)

A model is proposed for a solid whose mathematical form is similar to the Ginzburg–Landau theory for superconductors. An effect involving loss of shear stability of a crystalline medium in a field of shear stresses is discussed and the crystalline media are classified into those of the first and second kind depending on the nature of the defect penetration in the bulk of the material. © *1999 American Institute of Physics.* [S1063-7850(99)02110-2]

A major disadvantage of classical dislocation theory is that it starts from an analysis of an ideal crystal which is assumed to be absolutely stable. As far as we are aware, aspects of thermodynamic stability in the context of mechanical actions, i.e., an unmediated increase in temperature (for instance, melting as a result of a dislocation pile-up), have not yet been examined in the literature. In classical dislocation theory a medium can ''withstand'' any defect density and any stresses not exceeding the yield points. Even the attainment of the yield point is not considered in the mechanics of continuous media as a loss of thermodynamic stability and a transition to a different phase. However, it is well-known that mechanical actions may lead to a loss of thermodynamic stability which in terms of the thermodynamics of solids is expressed in phase diagrams in ''temperature (thermodynamic variable)–pressure (mechanical variable)'' space.

As the temperature increases, a medium may become stable with respect to shear stresses not only as a result of overcoming the yield point but also by melting. Both these types of action, mechanical and thermal, are conventionally analyzed independently in terms of the thermodynamics and mechanics of solids. The fact that such an analysis may prove inadequate under certain conditions becomes particularly obvious at the melting point: an infinitely small change in temperature then leads to a loss of mechanical stability (the shear modulus vanishes) and an infinitely small change in pressure or shear stress leads to a loss of thermodynamic stability (melting). Thus, the mechanical properties of crystalline solids cannot generally be analyzed independently of their thermodynamic stability. In the present paper we propose a model of a crystalline solid which describes both the mechanical and thermodynamic properties of solids using a common basis. The proposed model is mathematically similar to the Ginzburg–Landau theory[1] for superconductors. Some aspects similar to the proposed model may be found in Ref. 2.

The starting point for the Landau thermodynamic theory of phase transitions is the choice of order parameter η which characterizes the qualitative change in the state of a medium at the phase transition point. In the case of melting, the qualitative change can be characterized by the shear modulus μ, which is nonzero in the solid phase and zero in the liquid phase. In order to illustrate the main ideas of the thermomechanical model, we shall begin by analyzing a crystal–liquid crystal transition. This transition does not generally involve a change in the point symmetry of the substance and thus in principle can be considered to be a second-order transition.[3] Although crystalline media are usually converted to an isotropic liquid as the temperature increases, Patashinskiǐ and Shumilo[9] showed that it is theoretically possible for a transition to take place to an intermediate phase (stable or metastable) which does not possess long-range translational order but does possess long-range orientational order; the shear modulus of the intermediate phase is zero. Taking into account fluctuations, this transition may take place as a second-order phase transition.[8] We shall subsequently analyze a second-order transition from the crystalline phase to this intermediate phase. The model can easily be generalized to a first-order transition similar to the second-order one (with a small jump in the order parameter and the thermodynamic quantities at the transition point).

An important assumption in the Landau phenomenological theory of phase transitions is that the free energy of a medium is expanded as a series in powers of the order parameter and its gradients. This presupposes that the order parameter can take any value near zero. Since the shear modulus is always nonnegative, it cannot be taken as the order parameter itself but may be represented as the square of this parameter:

$$\mu = \eta^2. \tag{1}$$

In the general case of a spatially nonuniform distribution of the order parameter (systems where the shear modulus varies from one point to another), the expansion of the free energy contains powers as the order parameter and its gradients. We shall subsequently confine our analysis to weakly inhomogeneous systems at temperatures close to the phase transition temperature, which allows us to consider only the lowest powers of the order parameter and its gradients needed to describe the stable state of the crystalline and liquid-crystal phases:

$$F_{\text{therm}} = \int dV \left\{ a\eta^2 + \frac{b}{2}\eta^4 + g(\nabla\eta)^2 \right\}, \tag{2}$$

where a, b, and g are functions of the thermodynamic parameters of state, i.e., temperature and pressure.

It is easy to show that the coefficient $a(T)$ in the second-order term should vanish at the phase-transition point. In the symmetric phase, the minimum of F should correspond to the order parameter $\eta=0$, for which the condition $a>0$ must obviously be satisfied. On the other side of the transition point, in the crystalline phase the stable state should correspond to nonzero η which is only possible for $a<0$. If the value of a is positive on one side of the transition point and negative on the other, then a must vanish at the transition point.

In order to ensure that the phase transition point corresponds to the stable state, i.e., that the function η has a minimum (for $\eta=0$) at this point F, the coefficient b in the fourth-power term must be positive.

Since the function $a(T)$ vanishes at the transition point, it can then be expanded in powers of the "distance" from the critical temperature, with the expansion beginning with the first-order term:

$$a(T) = \alpha(T-T_c). \tag{3}$$

Here T_c is the phase transition temperature. At temperatures close to the transition temperature, the coefficient $b(T)$ may be replaced by $b(T_c)$. The expansion of the free energy thus has the form

$$F_{\text{therm}} = \int dV \left\{ \alpha(T-T_c)\eta^2 \frac{b}{2}\eta^4 + g(\nabla\eta)^2 \right\}. \tag{4}$$

The functional (2) [or (4)] describes the system in the minimum-energy state, i.e., in the elastically undeformed state. In the crystalline phase, as a result of the nonvanishing transverse rigidity of the system, the medium may be transferred to a deformed metastable state. In order to describe this state, we need to add the free energy of elastic deformation to the free energy (2), which generally (also in the presence of a nonzero plastic distortion tensor) has the form:[1]

$$F_{\text{el}} = \int dV \left\{ \mu\left[\frac{1}{4}\left(\frac{\partial u_i}{\partial x_j} + \frac{\partial u_j}{\partial x_i} - \beta_{ij} - \beta_{ji}\right)^2 - \frac{1}{3}(u_{ll})^2\right] + \frac{K}{2}(u_{ll})^2 \right\}, \tag{5}$$

where u_i is the total displacement vector, β_{ij} is the plastic distortion tensor, and K is the bulk modulus.

In a medium having a microstructure (in the sense defined in Ref. 4) the free energy (4) must be supplemented by the elastic deformation energy of the structural elements which is a quadratic function of the dislocation density tensor α_{km} in a medium of fixed characteristic length:[4]

$$F_{\alpha} = \int dV \cdot C_{ijkm}\alpha_{ij}\alpha_{km}, \tag{6}$$

$$\alpha_{km} = e_{ijk}\frac{\partial\beta_{jm}}{\partial x_i}. \tag{7}$$

The specific form of the tensor C_{ijkm} depends on the structural characteristics of the medium. Explicit expressions for C_{ijkm} for media having one or three mutually perpendicular glide systems were derived in Refs. 4 and 5.

We stress that, as was shown in Refs. 8 and 9, reasoning on the plastic distortion tensor and the dislocation density tensor may be applied both below the phase transition point (in the crystalline phase) and above this point (in the liquid-crystal phase). This is because the "local crystalline" order is also conserved in the liquid phase. In this case, the transition from the solid to the liquid phase is associated with the formation of a finite density of open (infinitely long) dislocations. In exactly the same way the existence of moment stresses [described by term (6) in the free energy] is not directly related to the existence of long-range crystalline order but it does assume that the medium possesses local anisotropy.

The total free energy thus has the form:

$$F_{\text{tot}} = F_{\text{therm}} + F_{\text{el}} + F_{\alpha} = \int dV \left\{ C_{ijkm}\alpha_{ij}\alpha_{km} + g(\nabla\eta)^2 \right.$$
$$+ \eta^2\left[\frac{1}{4}\left(\frac{\partial u_i}{\partial x_j} + \frac{\partial u_j}{\partial x_i} - \beta_{ij} - \beta_{ji}\right)^2 - \frac{1}{3}(u_{ll})^2\right]$$
$$\left. + \frac{K}{2}(u_{ll})^2 + a\eta^2 + \frac{b}{2}\eta^4 \right\}. \tag{8}$$

For comparison we recall the expression for the Ginzburg–Landau functional[1] for the free energy of a superconductor:

$$F = \int \left[\frac{\mathbf{B}^2}{8\pi} + \frac{\hbar^2}{4m}(\nabla|\psi|)^2 + \frac{\hbar^2}{4m}|\psi|^2\left(\nabla\Phi - \frac{2e}{\hbar c}\mathbf{A}\right)^2 \right.$$
$$\left. + \alpha(T-T_c)|\psi|^2 + \frac{b}{2}|\psi|^4\right]dV. \tag{9}$$

The similar structure of both functionals is obvious. Moreover, the following analogies are found between the various fields (see Table I).

The main difference between the functional (8) of an elastoplastic medium and the Ginzburg–Landau functional is that for the elastoplastic medium the vector field **u** appears instead of the scalar phase Φ. Thus, the potential ($\hat{\beta}$) and the field strength (the latter defined in both cases as curl of the potential) are second-rank tensors.

By way of an example of the effect described by the functional (8), we shall consider a crystal in the elastic state at a temperature below the melting point in a uniform stress field. The functional (8) then reduces to

$$F = \int dV \left\{ \alpha(T-T_c)\eta^2 + \frac{b}{2}\eta^4 + \eta^2\varepsilon^2 \right\}, \tag{10}$$

where ε is the elastic deformation tensor.

For $T<T_c$ and $\varepsilon=0$ the coefficient of the second power of the order parameter is negative which implies that the substance is in the solid state with the shear modulus

$$\mu = \eta^2 = \frac{\alpha(T_c-T)}{b} \neq 0. \tag{11}$$

TABLE I.

Superconductor		Elastoplastic medium	
Absolute value of wave function	$|\psi|$	Absolute value of order parameter	$|\eta|$
Concentration of superconducting electrons	$n_s = |\psi|^2$	Shear modulus	$\mu = \eta^2$
Phase of wave function	Φ	Total displacement vector	$\mathbf{u}$
Vector potential	$\mathbf{A}$	Plastic distortion tensor	$\hat{\beta}$
Magnetic field induction	$\mathbf{B} = \mathrm{curl}\mathbf{A}$	Dislocation density tensor	$\hat{\alpha} = \mathrm{curl}\hat{\beta}$

As the elastic distortions increase, the modulus of the coefficient in the second-order terms becomes smaller. Thus, the order parameter and the shear modulus decrease:

$$\mu = \eta^2 = \frac{\alpha(T_c - T) - \varepsilon^2}{b}. \tag{12}$$

For the specific strain

$$\varepsilon_c = \sqrt{\alpha(T_c - T)}, \tag{13}$$

the transverse rigidity of the medium becomes zero. We now conclude that a medium can lose stability in the thermodynamic sense, i.e., the shear modulus goes to zero and thus the medium is transferred to a ''liquid-like'' state, not only as a result of an increase in temperature but also as a result of a fairly high shear strain being created in the medium. The conclusion that the elastic modulus locally goes to zero in regions of stress concentrators was reached earlier as a result of analysis of experimental data made by V. E. Panin (see, for example, Ref. 6). The corresponding solid state was called the highly excited state of a solid.

On the basis of the functional (8), solids like superconductors can be classified into those of the first and second kinds. For this purpose we introduce two characteristic lengths: the correlation radius of the fluctuations $\xi(T)$

$$\xi(T) = \sqrt{\frac{g}{\alpha(T_c - T)}} \tag{14}$$

and the ''London penetration depth'' $\delta(T)$ which determines the characteristic length of the nonuniformity of the dislocation density near the surface of the solid (this length was introduced in Ref. 7):

$$\delta(T) = \sqrt{\frac{C}{2\mu}} = \sqrt{\frac{bC}{2\alpha(T_c - T)}}. \tag{15}$$

Here C is the characteristic value of the tensor of the moment elastic constants [C_{ijkl} in Eq. (6)]. The Ginzburg–Landau parameter is defined as the ratio of these two lengths

$$\kappa = \frac{\delta(T)}{\xi(T)} = \sqrt{\frac{bC}{2g}}. \tag{16}$$

Solids of the second kind have values of the Ginzburg–Landau parameter $\kappa \gg 1$. These solids lose their stability to shear deformation by means of a gradual penetration of vortex filaments into the bulk of the solid. If the solid is of the first kind ($\kappa \ll 1$), as the external influence increases, it undergoes a first-order phase transition when the dislocation density tensor exceeds a certain critical value at the solid surface.

We note that despite the fact that second-order ''crystal–liquid crystal'' transitions are theoretically possible (this topic is discussed, for example, in the conclusions to Ref. 8), in practice these transitions are generally first-order transitions. If we are dealing with a first-order transition similar to a second-order one, it may be described by adding a cubic term to the functional (8):

$$F' = \int c\,\eta^3 dV. \tag{17}$$

A detailed analysis of this more complex functional and the ''mixed state'' described by the functional (8) for $\kappa \gg 1$ is considerably more complex than that for superconductors because of the higher tensor rank of the dominant fields and cannot be made within the scope of the present letter.

---

[1])For simplicity we assume that the substance is isotropic.

---

[1] L. D. Landau and E. M. Lifshitz, *Statistical Physics*, Part 2, 3rd ed. (Pergamon Press, Oxford, 1980; Part 2, Nauka, Moscow 1978).

[2] J. L. Marques, in *Proceedings of the 9th International Symposium on Continuum Models and Discrete Systems (CMDS9)* (World Scientific, Singapore, 1999), pp. 576–583.

[3] L. D. Landau and E. M. Lifshitz, *Statistical Physics*, Part 1, 3rd ed. (Pergamon Press, Oxford, 1980; Part 1, Nauka, Moscow 1976).

[4] V. L. Popov and E. Kröner, Phys. Mesomechan. **1**(1), 103 (1998).

[5] E. Kröner and V. Popov, Comput. Mater. Sci. (1999) in press.

[6] V. E. Panin, Yu. V. Grinyaev, T. F. Elsukova, and A. G. Ivanchin, Izv. Vyssh. Uchebn. Zaved. Fiz. No. 6, 5 (1982).

[7] V. L. Popov, Pis'ma Zh. Tekh. Fiz. **19**(23), 79 (1993) [Tech. Phys. Lett. **19**, 768 (1993)].

[8] S. P. Obukhov, Zh. Éksp. Teor. Fiz. **83**, 1978 (1982) [Sov. Phys. JETP **56**, 1144 (1982)].

[9] A. Z. Patashinskiĭ and B. I. Shumilo, Zh. Éksp. Teor. Fiz. **89**, 315 (1985) [Sov. Phys. JETP **62**, 177 (1985)].

Translated by R. M. Durham

Generalized excitation of a coaxial cylindrical lens

L. P. Ovsyannikova and T. Ya. Fishkova

A. F. Ioffe Physicotechnical Institute, Russian Academy of Sciences, St. Petersburg
(Submitted June 16, 1999)
Pis'ma Zh. Tekh. Fiz. **25**, 39–43 (October 26, 1999)

Calculations are made of the cardinal elements of a coaxial lens when annular beams are focused
onto its axis. An empirical formula is obtained for the excitation of the lens which takes
into account its power, and the transverse and longitudinal dimensions, and can be used to obtain
simple expressions for the position of the focus and the initial radius of the axial trajectory
of the beam. © *1999 American Institute of Physics.* [S1063-7850(99)02210-7]

An electrostatic lens consisting of two coaxial cylinders and a planar diaphragm positioned at the entrance near the cylindrical electrodes can be used to focus hollow beams of charged particles onto the optical axis of the lens.[1] This lens is strongly focusing and may replace a system of quadrupole lenses and has a much simpler design.

In previous studies the authors[2] determined the optimum position of the inlet diaphragm of a coaxial cylindrical lens and also calculated its cardinal elements and loading characteristics for various cylinder radii, for a length not exceeding the diameter of the outer cylinder. In order to obtain a general expression for the excitation of a lens which relates its electrical and geometric parameters, in the present study we make calculations for a coaxial cylindrical lens having different lengths and ratios of cylinder radii.

The calculations were made using a computer program for electrostatic electron-optical systems with rotational symmetry, of which the modification of a coaxial cylindrical lens proposed by the authors is one. The cardinal elements of the lens were calculated for axial focusing regimes: the focal length, the position of the principal plane, and also the radius of the axial trajectory about which the focusing is achieved. The ratio of the radii of the outer and inner cylinders was varied in the range $R/\rho = 10$–100 with the optimum gap between the diaphragm and the outer cylindrical electrode $s = 0.1R$. In this case, the length of the lens was increased until the particles impinged on the inner cylindrical electrode.

Figures 1 and 2 gives the results of calculating the cardinal elements of a coaxial cylindrical lens. Figure 1 shows a schematic of the lens, the profile of the axial trajectory, and the potential distribution along this trajectory for various lens powers (the ratio of the potential difference between the electrodes to the beam energy eV/ε). The brackets in these figures indicate the values of the cardinal elements in regimes when the particles begin to settle on the inner electrode of the lens.

The beam focusing problem cannot be solved analytically for this modification of a coaxial cylindrical lens. Thus, we determined the cardinal elements of the lens empirically by means of numerical calculations. In Ref. 2 we derived expressions for the focal length, the position of the principal plane, and the input radius of the axial beam trajectory for a coaxial cylindrical lens with $R/\rho = 2$–1000 and length $l \leqslant 2R$. Our results showed that these formulas give significant errors for lenses of length $l \geqslant 3R$. Thus, it is interesting to determine the cardinal elements over the entire range of lens lengths.

We noted some regularity which allowed us to obtain an empirical formula for the generalized excitation of a coaxial cylindrical lens with a planar input diaphragm, taking into account the lens power and its transverse and longitudinal dimensions:

$$q = (eV/\varepsilon)(l/R)^{2/3}R/(R-\rho). \tag{1}$$

It should be noted that it is desirable to minimize the lens power to focus beams (especially high-energy ones). Numerical calculations have shown that a coaxial cylindrical lens having a power not exceeding $eV/\varepsilon = 0.3$ can focus a beam at an arbitrary distance from the lens up to $\approx 0.5R$. Thus, we confined ourselves to this lens power to derive the formulas for the cardinal elements.

This generalized excitation was used to obtain a very simple empirical formula for the position of the focus measured from the midplane of the lens $l_f = f + h$:

$$l_f/R = 1.8/q. \tag{2}$$

The empirical formula for the input radius of the axial beam trajectory about which focusing on the lens axis takes place is then:

$$r_0/R = 0.3(3\tanh l/R - q). \tag{3}$$

The positions of the foci determined from Eq. (2) allowing for Eq. (1) differ from the numerical calculations by less than 25% over a wide range of lens lengths. Exceptions to this are regimes where the focus is close to the lens exit (at a distance less than the diameter of the outer cylinder) when the error reaches 50%. The largest difference between the initial input radii of the axial trajectory determined using formula (3) and the numerical calculations does not exceed 10–12%.

It is interesting to compare the powers of a coaxial cylindrical lens and a quadrupole lens. If the focal length of a quadrupole lens is approximately twice its length, the weak lens approximation is valid. The ratio of the focal length of coaxial cylindrical lens to that of a quadrupole lens having the same longitudinal and transverse dimensions is approxi-
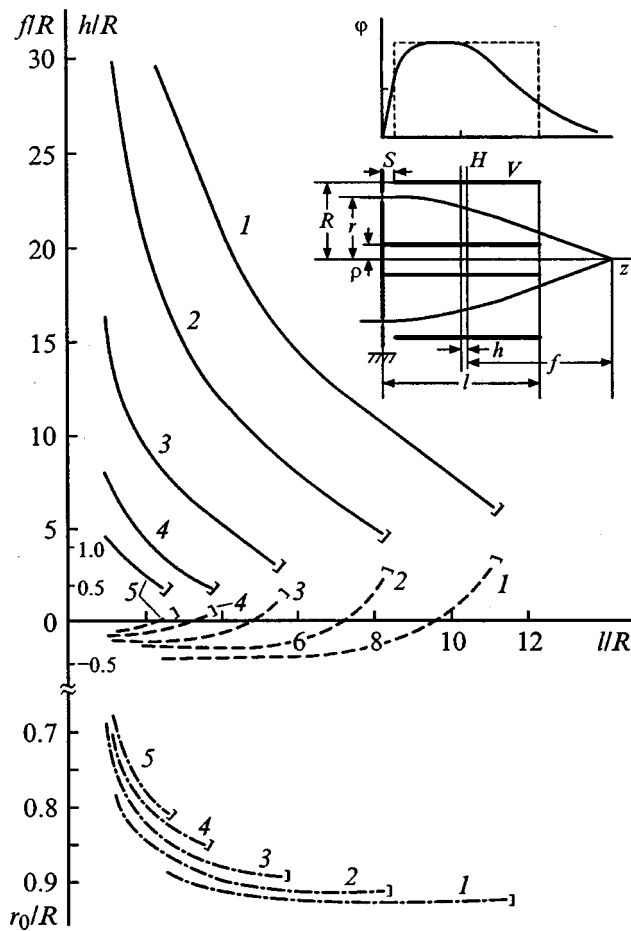
FIG. 1. Focal lengths (solid curves), positions of principal plane (dashed curves), and input radius of axial beam trajectory (dot-dash curves) as a function of the lens length for $R/\rho = 10$. Curve *1* — $eV/\varepsilon = 0.03$, *2* — 0.05, *3* — 0.1, *4* — 0.2, and *5* — 0.3.
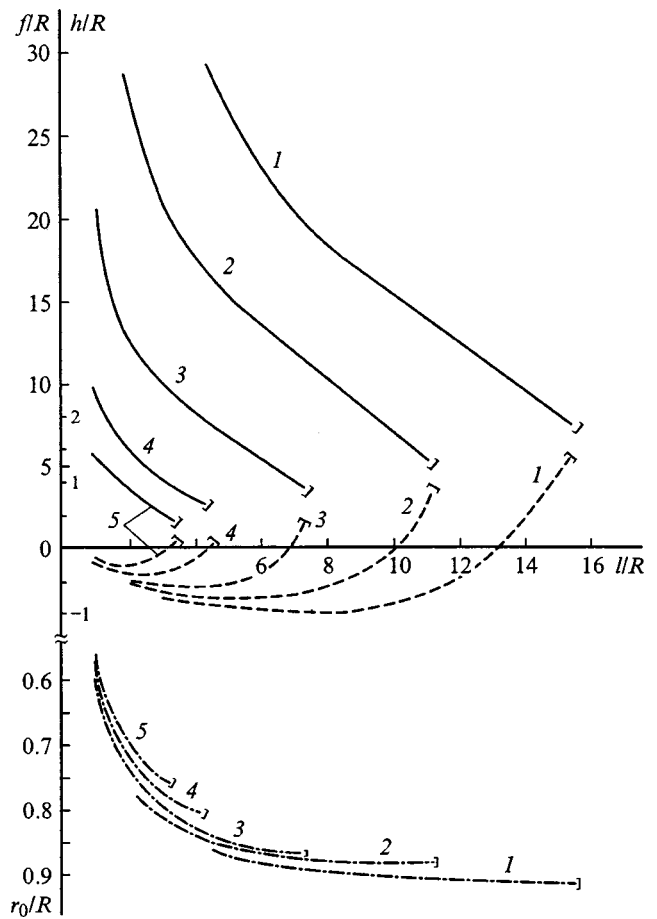

FIG. 2. As Fig. 1 for $R/\rho = 100$.

mately $(l/R)^{1/3}$. This implies that for $l \geqslant R$ a quadrupole lens is more powerful. However, since at least two quadrupole lenses are required for focusing to a point, it is natural to compare a coaxial cylindrical lens with a doublet. The calculations showed that for a coaxial cylindrical lens and quadrupole doublet of the same length, the focal length of the coaxial cylindrical lens is at least three times smaller. Moreover, if the angular intensity distribution in the source is uniform, the optical power of a coaxial cylindrical lens is substantially greater than that of a system of quadrupole lenses since, for the same expansion angles, the intensity of a

hollow beam is an order of magnitude higher than that of an axial one. Thus, in devices and equipment using annular beams it is preferable to use a coaxial lens consisting of two cylinders and a planar input diaphragm.

[1] L. P. Ovsyannikova and T. Ya. Fishkova, Pis'ma Zh. Tekh. Fiz. **22**(15), 39 (1996) [Tech. Phys. Lett. **22**, 660 (1996)].
[2] L. P. Ovsyannikova and T. Ya. Fishkova, Zh. Tekh. Fiz. **67**(12), 81 (1997); **68**(6), 124 (1998) [Tech. Phys. Lett. **42**, 1444 (1997); *ibid.* **43**, 726 (1998)].

Translated by R. M. Durham

Characteristics of microwave radiation from copper-containing fullerene resonators at liquid-nitrogen temperatures

O. I. Kon'kov and A. V. Prikhod'ko

A. F. Ioffe Physicotechnical Institute, St. Petersburg St. Petersburg State Technical University
(Submitted July 3, 1999)

An investigation is made of the radiative microwave properties (43 GHz frequency) of an open dielectric resonator based on a copper-containing fullerene membrane. It is established that a broad emission peak exists in the range 90–110 K caused by an increase in the resonator Q factor in this temperature range.   © *1999 American Institute of Physics.*
[S1063-7850(99)02310-1]

The present paper is devoted to a study of microwave antennas based on open dielectric resonators. The use of these resonators, where the electric and magnetic fields extend over distances much greater than the radiation wavelength, has revealed efficient transfer of electromagnetic energy to the surrounding space.[1] Open dielectric resonators in the form of a cylinder in which the lowest electromagnetic oscillations are excited are most frequently used for these purposes. The functional capabilities of these resonators can be extended appreciably by solving the problems of resonant frequency tuning and also by controlling the radiation intensity. In order to improve the high directionality of the radiation and enhance the gain, several resonators are distributed in a space and are excited so that the phases of their fields combine in the required direction.

Here we investigate open dielectric resonators based on a promising new low-conductivity material — polycrystalline copper-containing fullerene membrane.[2] For these membranes a correlation has been observed between magnetic and microwave experiments[3] which indicates that a diamagnetic anomaly exists at temperatures of 90–150 K. The aim of this study is to determine the characteristics of the microwave radiation in this temperature range. Note that when studying the emitting properties of powder-like copper-fullerene antennas, Masterov *et al.*[4] observed an abrupt increase in the radiation power at temperatures below 80 K as the Q factor increased.

Figure 1 shows a schematic of the microwave experiment. The measuring system is the same as that described in Ref. 4. The exciting slit measured 0.5×8 mm, and we used an R2-65 oscillatorand an S4-27 amplitude-frequency analyzer. The parameters of the open dielectric resonator formed by the copper-containing fullerene membrane were:[3] diameter 2.5 mm and thickness in central part 2 mm. The technological parameters of the membrane fabrication process were described in Refs. 2 and 3.

Figure 2 gives the temperature dependence of the emitted power P which clearly reveals a singularity in the form of a radiation peak in the temperature range 90–110 K. On the basis of the results described in

Ref. 3, this singularity can be attributed to an increase in the conductivity of the copper-containing fullerene which is accompanied by an increase in the resonator Q factor.

Figure 3 shows the amplitude-frequency characteristics of the open dielectric resonator at 225 and 110 K which indicates that the width of the resonant line decreases. At 225 K the line width at the 0.7 level (curve *1* in Fig. 3) is 0.32 MHz whereas at 110 K it is approximately half of this (0.16–0.2 MHz).

To sum up, it has been established experimentally that the microwave emission of copper-containing fullerene resonators has a singularity in the form of a peak and an increase in Q factor in the temperature range 90–110 K.
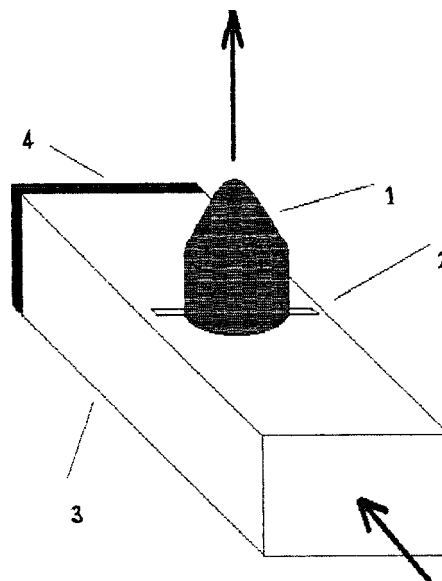

FIG. 1. Measuring system: *1* — open dielectric resonator, *2* — strongly emitting quarter-wave slit, *3* — 8 mm waveguide, and *4* — short-circuiting plunger. The arrows indicate the direction of the microwave incident on the waveguide and emitted by the membrane.
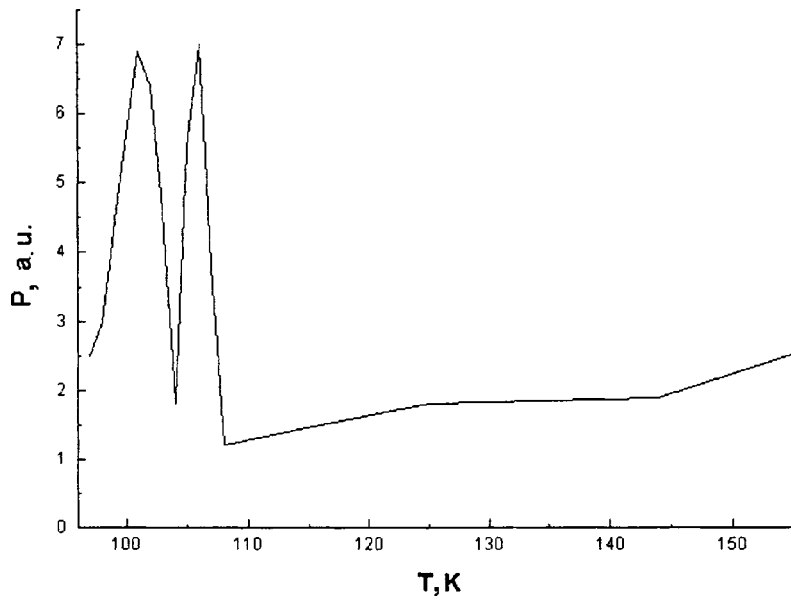
FIG. 2. Temperature dependence of the power P emitted by the open dielectric resonator.
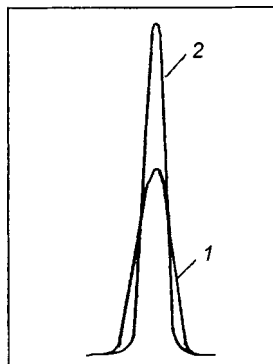

FIG. 3. Broadening of the resonant line of the open dielectric resonator at 225 K (curve *1*) compared with that at 110 K at which the radiation peak is observed (curve *2*). The resonant frequency is 43 GHz.

[1] *Dielectric Resonators*, edited by M. E. Il'chenko (Radio i Svyaz', Moscow, 1989), 328 pp.
[2] V. F. Masterov, A. V. Prikhod'ko, T. R. Stepanova, V. Yu. Davydov, and O. I. Kon'kov, Fiz. Tverd. Tela (St. Petersburg) **40**, 580 (1998) [Phys. Solid State **40**, 535 (1998)].
[3] V. F. Masterov, A. V. Prikhod'ko, O. I. Kon'kov, and E. I. Terukov, Fiz. Tverd. Tela (St. Petersburg) **39**, 816 (1997) [Phys. Solid State **39**, 722 (1997)].
[4] V. F. Masterov, A. V. Prikhod'ko, V. V. Romanov, K. F. Shtel'makh, and O. I. Kon'kov, Fiz. Tverd. Tela (St. Petersburg) **41**, 748 (1999) [Phys. Solid State **41**, 676 (1999)].

Translated by R. M. Durham

Modeling of strain localization in the dynamics of a softening rod

N. N. Myagkov

Institute of Applied Mechanics, Russian Academy of Sciences, Moscow
(Submitted May 17, 1999)
Pis'ma Zh. Tekh. Fiz. **25**, 48–53 (October 26, 1999)

An elastoplastic model with a second-order gradient is used to analyze the dynamics of a one-dimensional rod at the deformation softening stage taking into account the nonlinearity of the descending part of the diagram. An exact solution of this nonlinear equation is obtained which describes the strongly inhomogeneous nonsteady-state structure of the strain localization zone formed from an initially smooth perturbation and culminating in collapse. © *1999 American Institute of Physics.* [S1063-7850(99)02410-6]

It is well-known that the nonlinearity of a continuous medium leads to the appearance of localized formations, i.e., steady-state isolated waves or solitons. It has recently become apparent[1] that other related localized formations or wave collapses play an equally important role. In the present paper localized solutions will be analyzed with reference to the dynamics of a one-dimensional rod at the deformation softening stage.

Deformation softening, a reduction in stress with increasing strain, is the stage preceding fracture. This behavior occurs in a wide range of materials including metals, concrete, and geologic materials. Attempts to describe this effect using classical local models insensitive to the strain rate have the result that the system of equations ceases to be hyperbolic and the Cauchy problem becomes incorrectly formulated.[2,3] Various methods of regularizing this problem are available. We shall use an elastoplastic model in which the yield function depends not only on the stress and strain but also on the second-order strain gradient. In this case, the system of equations for a one-dimensional rod has the following form:[2]

$$\frac{\partial \varepsilon}{\partial t} = \frac{\partial u}{\partial x}, \quad \frac{\partial u}{\partial t} = \frac{d\sigma_s(\varepsilon)}{d\varepsilon} \cdot \frac{\partial \varepsilon}{\partial x} - \delta^2 \frac{\partial^3 \varepsilon}{\partial x^3}, \tag{1}$$

where ε is the total strain, u is the strain rate, and $\sigma_s(\varepsilon)$ is the diagram of the material. The system (1) is dedimensionalized using the density ρ, the rate $\sqrt{E_y/\rho}$, where E_y is the elastic modulus, and the characteristic length L of the problem. In addition, $\delta^2 = l^2/L^2$ is a small dimensionless parameter where l is the internal structure parameter of the material introduced to regularize the elastoplastic model.

Assuming that the state of the rod is homogeneous, we shall analyze a small perturbation of this state

$$\varepsilon', u' \propto \exp(ikx - i\omega t),$$

where ω and k are the frequency and wave number, respectively, ε' and u' are the strain increment and rate, and linearizing Eq. (1), we find the dispersion equation for this system

$$\omega^2 = (-\kappa + \delta^2 k^2) k^2, \tag{2}$$

where $\kappa = -d\sigma_s(\varepsilon_0)/d\varepsilon$. The descending part of the diagram (softening) corresponds to $\kappa > 0$. Although this system is a purely dispersive one, for $\kappa > \delta^2 k^2$ the roots of the dispersion equation (2) form a complex-conjugate pair: so-called dispersion instability occurs (see Ref. 4, for instance). When $\kappa < \delta^2 k^2$, neutral stability is established, i.e., the waves propagate as in a dispersion system. The parameter κ plays the role of the control parameter. The minimum point $k_c = 0$, $\kappa_c = 0$ on the neutral curve $\kappa = \delta^2 k^2$ is the bifurcation point and the long-wavelength mode $k = 0$ is the first mode which becomes unstable when the parameter κ passes through zero. For $\kappa > 0$ the amplitude begins to increase and it is clearly incorrect to neglect nonlinear terms at this stage. We shall use a quadratic approximation for $\sigma_s(\varepsilon)$: $d\sigma_s(\varepsilon)/d\varepsilon = -\kappa + f\varepsilon'$. Using this relation, after simple transformations we obtain an equation for ε' from Eq. (1):

$$\frac{\partial^2 \varepsilon'}{\partial t^2} + \frac{\partial^2}{\partial x^2} \left(\kappa \varepsilon' - \frac{1}{2} f\varepsilon'^2 + \delta^2 \frac{\partial^2 \varepsilon'}{\partial x^2} \right) = 0. \tag{3}$$

Note that for $\kappa < 0$ Eq. (3) agrees to within the sign of the leading derivative with the well-known Boussinesq equation which is encountered as a long-wavelength approximation in various physical applications (for instance, waves at the surface of water, waves in discrete chains). We know that the Boussinesq equation can be integrated by the method of the inverse scattering problem and has N-soliton solutions for waves propagating to the right and to the left.[5] It is easy to see that the latter may serve as a formal basis for constructing a class of exact nonsteady-state localized solutions of Eq. (3) for a softening medium corresponding to $\kappa > 0$.

We shall analyze Eq. (3) for values of the parameters $\kappa > 0$, $f < 0$. We shall use the Hirota method (see Ref. 5, for example) to construct exact particular solutions. Following this method we set

$$\varepsilon' = -\frac{12\delta^2}{f} \cdot \frac{\partial^2 (\ln F_N)}{\partial x^2}, \tag{4}$$

where F_N is a new unknown function. After substituting into Eq. (3), integrating twice, and setting the integration constants to zero, after various transformations we obtain the quadratic form
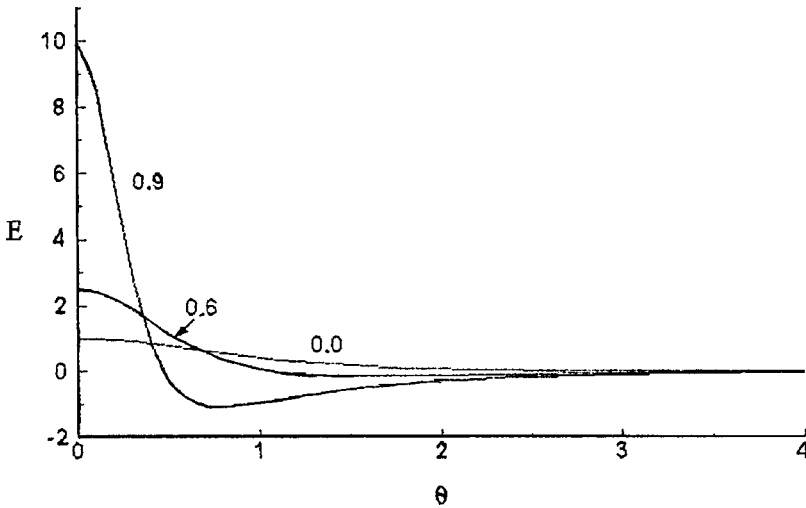
FIG. 1. Localization of the strain [the solution (9)] for various values of the parameter $a = -\exp(-A_{12}/2) \times \cos\varphi$ (indicated by the figures in the diagram). The solution is symmetric relative to the axis $\theta = 0$: $E = \varepsilon'(-f/(12\delta^2 k^2))$, $f<0$, $\theta = kx + \eta_R^{(0)} + A_{12}/2$, $\varphi = \Omega t + \eta_I^{(0)}$, $\Omega > 0$.

$$F_{N,tt} \cdot F_N - F_{N,t}^2 + \kappa(F_{N,xx} \cdot F_N - F_{N,x}^2) + \delta^2$$
$$\times (F_{N,xxxx} \cdot F_N - 4F_{N,x} \cdot F_{N,xxx} + 3F_{N,xx}^2) = 0. \qquad (5)$$

Here we have $F_t \equiv \partial F/\partial t$, $F_{tt} \equiv \partial^2 F/\partial t^2$, and so on. We shall use the family of functions which gives N-soliton solutions for the ''correct'' Boussinesq equation. The first function in this family

$$F_1 = 1 + \exp(\eta_1), \quad \eta_1 = k_1 x \pm i k_1 \sqrt{\kappa + \delta^2 k_1^2} \cdot t + \eta_1^{(0)}, \qquad (6)$$

where k_1, $\eta_1^{(0)}$ are constants, and k_1 is a real constant, is a solution of Eq. (5) and gives a complex solution of Eq. (3) by means of the transformation (4). In this case, however, only the real solutions of Eq. (3) can have any physical meaning. In order to obtain a real solution, we need to use at least the function F_2 which generates a two-soliton solution for the ''correct'' Boussinesq equation. In our case, we have

$$F_2 = 1 + \exp(\eta_1) + \exp(\eta_2) + \exp(\eta_1 + \eta_2 + A_{12}), \qquad (7)$$

$$\eta_m = k_m x + i\chi_m k_m \sqrt{\kappa + \delta^2 k_m^2} \cdot t + \eta_m^{(0)}, \quad \chi_m = \pm 1,$$

$$\exp(A_{12}) = \frac{3\delta^2(k_1 - k_2)^2 + (\chi_1 \sqrt{\kappa + \delta^2 k_1^2} - \chi_2 \sqrt{\kappa + \delta^2 k_2^2})^2}{3\delta^2(k_1 + k_2)^2 + (\chi_1 \sqrt{\kappa + \delta^2 k_1^2} - \chi_2 \sqrt{\kappa + \delta^2 k_2^2})^2},$$

where k_m are real and $\eta_m^{(0)}$ are complex constants. The function F_2, being a solution of Eq. (5), will only be real when η_1 and η_2 are complex-conjugate. Taking $k \equiv k_1 = k_2$, $\eta^{(0)} \equiv \eta_1^{(0)} = (\eta_2^{(0)})^*$, and $\chi_1 = -\chi_2 = 1$, we obtain from Eq. (7)

$$F_2 = 1 + 2\exp(kx + \eta_R^{(0)}) \cdot \cos(\Omega t + \eta_I^{(0)})$$
$$+ \exp[2(kx + \eta_R^{(0)}) + A_{12}], \qquad (8)$$

where

$$\exp(A_{12}) = \frac{\kappa + \delta^2 k^2}{\kappa + 4\delta^2 k^2}, \quad \Omega = k\sqrt{\kappa + \delta^2 k^2},$$

$$\eta_R^{(0)} = \text{Re } \eta^{(0)}, \quad \eta_I^{(0)} = \text{Im } \eta^{(0)}.$$

By substituting Eq. (8) into Eq. (4), we obtain a solution in the form of a nonsteady localized state which decays fairly rapidly for $|x| \to \infty$:

$$\varepsilon' = -\frac{12\delta^2 k^2}{f}$$

$$\times \frac{\cosh(kx + \eta_R^{(0)} + A_{12}) \cdot \cos(\Omega t + \eta_I^{(0)}) \cdot \exp(-A_{12}/2) + 1}{[\cosh(kx + \eta_R^{(0)} + A_{12}) + \cos(\Omega t + \eta_I^{(0)}) \cdot \exp(-A_{12}/2)]^2}. \qquad (9)$$

Using Eq. (4) and the first equation in the system (1), the solution for the strain 1 'rate is defined as

$$u' = -\frac{12\delta^2}{f} \cdot \frac{\partial^2(\ln F_N)}{\partial x \partial t}.$$

After substituting the solutions (8) into this expression, we obtain:

$$u' = -\frac{12\delta^2 k\Omega}{f}$$

$$\times \frac{\sinh(kx + \eta_R^{(0)} + A_{12}) \cdot \sin(\Omega t + \eta_I^{(0)}) \cdot \exp(-A_{12}/2)}{[\cosh(kx + \eta_R^{(0)} + A_{12}) + \cos(\Omega t + \eta_I^{(0)}) \cdot \exp(-A_{12}/2)]^2}. \qquad (10)$$

We shall analyze the solution (9) assuming $\Omega > 0$ and to be specific $\eta_I^{(0)} = 0$. We introduce the notation $\theta = kx + \eta_R^{(0)} + A_{12}/2$. It can be seen that the solution (9) is symmetric with respect to the axis $\theta = 0$ and at $t = 0$ describes a smooth soliton-like perturbation. The growth of the strain amplitude and subsequent collapse occurs because $\exp(A_{12}) < 1$. The solution is localized near the point $\theta = 0$ (see Fig. 1). At this point the amplitude increases with time as

$$\varepsilon'(0) = -\frac{12\delta^2 k^2}{f} \cdot \frac{1}{1 + \exp(-A_{12}/2) \cdot (\Omega t)}, \qquad (11)$$

and the effective width of the localization zone decreases as

$$\Delta\theta = 2\,\text{arccosh}\left(\frac{2 - \exp(-A_{12})\cos^2(\Omega t)}{-\exp(-A_{12}/2)\cos(\Omega t)}\right),$$

$$-\exp(A_{12}/2) < \cos(\Omega t) < 0. \qquad (12)$$

Singularity of the solution (collapse) is achieved at the point $\theta = 0$ at time

$$t_c = \Omega^{-1}[\pi - \arccos(\exp(A_{12}/2))]. \qquad (13)$$

The integrals of motion are satisfied at any point $t < t_c$ but diverge in the limit $t \rightarrow t_c$. The singularity occurring at time $t = t_c$ is nonintegrable.

Real solutions of Eq. (5) can be constructed similarly for $N > 2$. For example, for $N = 4$ the solution will be a nonlinear superposition of two localized formations.

Quite clearly, when the strain increases without bound, the analysis cannot be confined to quadratic terms in the expansion $\sigma_s(\varepsilon)$ but it is more important to include dissipa- tive mechanisms in the model (3), which limit the singularity to a specific level.

[1] V. E. Zakharov, *Problems of Physical Kinetics and Solid-State Physics*, Naukova Dumka, Kiev (1990), pp. 469–486.
[2] V. Kukudzhanov, J. Opt. Technol. **8**, 207 (1998).
[3] V. N. Kukudzhanov, Izv. Ross. Akad. Nauk Ser. MTT No. **6**, 104 (1998).
[4] R. K. Dodd, J. C. Eilbeck, J. Gibbon, and H. C. Morris, *Solitons and Nonlinear Wave Equations* (Academic Press, New York, 1982; Nauka, Moscow, 1988, 694 pp.).
[5] M. J. Ablowitz and H. Segur, *Solitons and the Inverse Scattering Transform* (SIAM, Philadelphia, Pa., 1981; Nauka, Moscow, 1987, 479 pp.).

Translated by R. M. Durham

Bulk changes in the microhardness of a solid WC–110G13 steel alloy exposed to a low-energy, high-current electron beam

S. F. Gnyusov, Yu. F. Ivanov, D. I. Proskurovskiĭ, and V. P. Rotshteĭn

Institute of Strength Physics and Materials Science, Siberian Branch of the Russian Academy of Sciences, Tomsk; Institute of High-Current Electronics, Siberian Branch of the Russian Academy of Sciences, Tomsk

Bulk changes in the microhardness of a solid WC–110G13 steel alloy are studied as a function of the energy density of a low-energy, high-current electron beam, the number of pulses, and the target thickness. It is established that the beam energy density has a threshold at which quasiperiodic changes in the microhardness occur in the bulk of the alloy. © *1999 American Institute of Physics.* [S1063-7850(99)02510-0]

It was shown in Refs. 1–3 that when martensitic steels are exposed to high-current electron beams, an extended zone of influence nonuniformly hardened over depth is formed with layers of anomalously high microhardness. The number and relative position of these layers is generally determined by the parameters of the stress wave or the shock wave generated in the surface layer under pulsed heating and by its conditions of reflection from the free surfaces of the sample.[3] A similar effect of nonuniform hardening over depth was observed when a solid WC–110G13 steel alloy (30 wt.%) was exposed to a low-energy, high-current electron beam of microsecond duration.[4] The aim of the present paper is to study the laws governing the changes in the microhardness at the surface and in the bulk of this material as a function of the beam energy density, the number of pulses, and the target thickness.

For the experiments we used samples of solid WC–110G13 steel alloy (30 wt.%) in the form of plates measuring $5 \times 40 \times 5.5$ mm and cylinders 20 mm in diameter and 10 mm high. In the initial state the material comprised tungsten carbide particles having an average grain size of 3 μm and a hcp lattice, uniformly distributed in a matrix based on an iron γ-solid solution.[4] The samples were bombarded with a low-energy, high-current electron beam having the parameters: electron energy 10–40 keV, energy density E_s = 5, 10, 20, 30, and 40 J/cm^2, pulse duration 2.5 μs, and number of pulses N = 1, 3, 6, 10, 20, and 50. The beam diameter in the target plane was 3–8 cm. The beam source was described in Ref. 5. After irradiation, the samples were cut along the beam axis for the metallographic examination and measurements of the depth distribution of the microhardness. The measurements were made using a PMT-3 device with a 0.1 N load at depth intervals of 30 μm. On each sample we made three tracks, 250 μm apart, in the axial part of the beam. The structural phase state of the material was examined by means of x-ray structural and micro-x-ray spectral analyses.

The experiments showed that at E_s = 5 J/cm^2, clear signs of melting can be detected on the surface. As the energy density increases in the range 5–40 J/cm^2, the thickness of the molten surface layer determined by metallographic ex-amination increases from 0.5–1 to 8–10 μm. In this case, an increase in the number of pulses does not cause any significant increase in the thickness of the molten zone. For E_s = 40 J/cm^2 appreciable evaporation of the material is observed, as is evidenced by the presence of solidified microdroplets on the surface and a ~10% reduction in the binding phase in a surface layer ~5 μm thick.

At energy densities $E_s \leq 30$ J/cm^2 only surface hardening is observed regardless of the number of pulses. The maximum microhardness $H_\mu \sim 10$ GPa is observed at the surface (in the initial state $H_\mu = 7.5$ GPa) and the thickness of the hardened layer is ~100 μm. A similar pattern of pure surface hardening is also observed for E_s = 40 J/cm^2 and N = 1, with the microhardness increasing to ~13 GPa at the surface. For $N \geq 3$ the hardening pattern changes abruptly: in addition to surface hardening, quasiperiodic hardening is observed in the bulk of the material (see Fig. 1). Thus, for a given pulse duration and electron energy the bulk change in the microhardness is a threshold process depending on the energy density and number of pulses.

The experiments showed that for E_s = 40 J/cm^2 and samples 5.5 mm thick, quasiperiodic changes in microhardness with a step of 0.25–1 mm are observed over the entire thickness of the sample. As the number of pulses increases (from N = 6) the number of microhardness peaks increases, with the average level remaining the same (10–11 GPa) but the maximum (in the peaks) reaching ~15 GPa. For N = 50 hardening is observed near the back of the sample (see Fig. 1e). When the sample thickness is increased to 10 mm, a quasiperiodic change in the microhardness is observed to depths of 7 mm (see Fig. 1f) (Ref. 4). However, an increase in the thickness of the target (for N = 10) leads to a reduction in the number of peaks, a lower maximum, and a lower average microhardness (see Figs. 1c and 1f).

Structural analyses showed that for E_s = 40 J/cm^2 and N = 10 a white unetched layer 1.5–2 μm thick forms on the surface (with a melt thickness of ~10 μm). This layer has a nanocrystalline structure and consists of fcc and hcp tungsten carbide particles and complex carbides such as $M_{23}C_6$ and M_7C_3. At large depths within the molten layer the binder
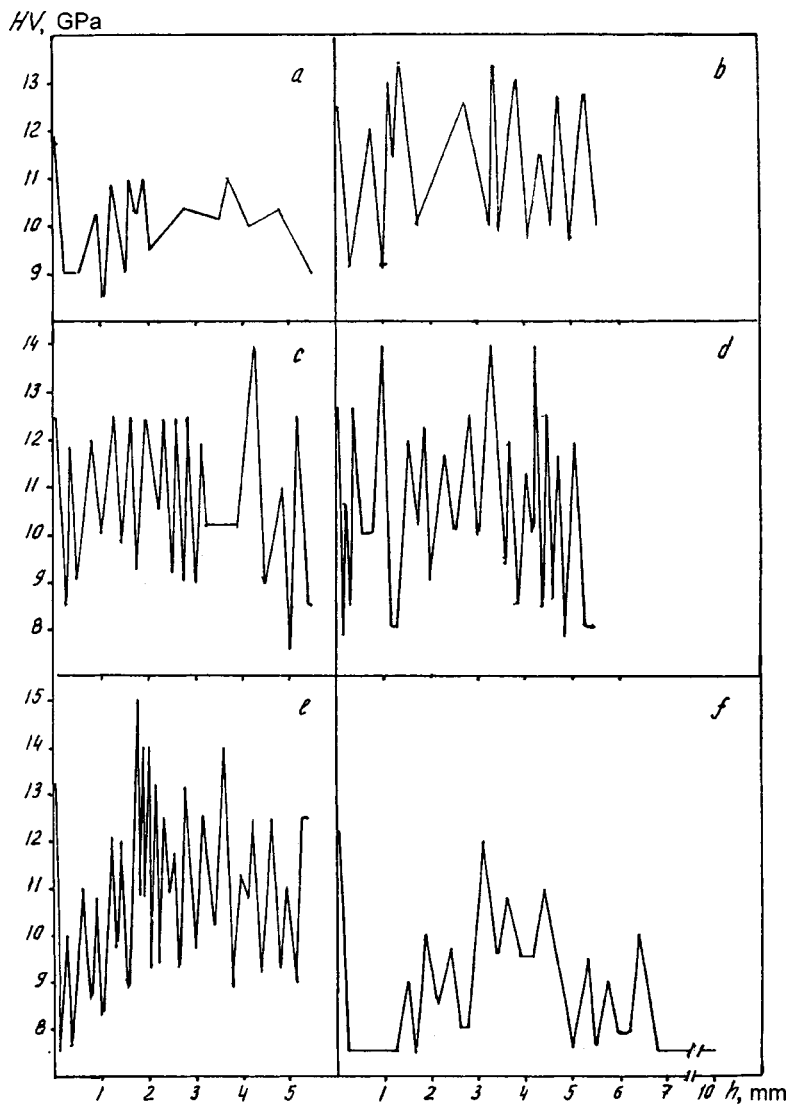
FIG. 1. Depth distributions of microhardness in WC–110G13 steel samples exposed to a low-energy, high-current electron beam with an energy density of 40 J/cm^2 for various numbers of pulses: a — 3, b — 6, c, f — 10, d — 20, and e — 50.

phase, comprising an α-Fe (bcc) solid solution, is distributed in the form of layers 8–10 nm thick between W_2C carbide crystallites.[4]

The structure of the material in the microhardness peaks is characterized by a high dislocation density and partial (~15 vol.%) $\gamma \Rightarrow \alpha$ martensitic rearrangement of the crystal lattice of the binder phase. In the tungsten carbide crystals the scalar density of dislocations and deformation twins increases and various particles disappear.[4] Note that similar substructural changes in this material (except for the $\gamma \Rightarrow \alpha$ conversion) are observed under static compression conditions at loads higher than 3 GPa (Ref. 6). The structure of the material in the layers between the microhardness peaks is almost the same as the initial material.[4]

The structure and properties of the material in the surface layer are mainly determined by the dynamics of the thermal fields formed under pulsed heating. Thermal calculations reported by Proskurovsky *et al.*[7] indicate that the formation of a nanocrystalline carbide structure in the surface layer may be attributed to the high-speed quenching from the melt. The attainment of maximum microhardness at the surface is caused by the dispersion of the structure and by a

reduction in the fraction of the binder as a result of selective evaporation.

In addition to high temperatures, the surface layer is also subjected to thermal compressive and tensile stresses because of the temperature gradients in the planes parallel to the irradiated surface. Estimates[8] indicate that the amplitude of these stresses may reach several gigapascals. These stresses are localized in the zone of thermal influence and may substantially alter the structure and microhardness of the material at depths considerably greater than the melt thickness.

The main factor determining the state of the material in the bulk is the stress wave formed as a result of the thermoelasticity effect and the recoil momentum of the expanding material vapor. Estimates show that the amplitude of the stress wave does not exceed 200 MPa. This wave may have a complex profile: unlike a pure elastic bipolar stress wave, it may change sign several times with a period of $\sim 10^{-7}$ s (Ref. 7). When reflected from free surfaces, the wave profile may become even more complex as a result of traveling and reflected waves being superposed. Since the amplitude of the stress wave is substantially lower than the yield point of the

material, the observed quasiperiodic bulk hardening effect may occur because the material undergoes short-lived variable-sign (compressive–tensile) high-frequency loading in the longitudinal direction. The local stresses at the carbide–binder–carbide contact may be an order of magnitude higher than the peak values as a result of effects similar to those achieved in a Bridgman chamber. The absence of any penetrating hardening in the 10 m thick sample (Fig. 1f) may be explained by the fact that at a depth of 7 mm because of damping, the amplitude of the stress wave becomes insufficient to form this quasiperiodic structure.

[1] Yu. F. Ivanov, V. I. Itin, S. V. Lykov *et al.*, Izv. Ross. Akad. Nauk Ser. Metally No. **3**, 130 (1993).

[2] A. M. Efremov, Yu. F. Ivanov, V. I. Itin *et al.*, Pis'ma Zh. Tekh. Fiz. **19**(2), 23 (1993) [Tech. Phys. Lett. **19**, 46 (1993)].

[3] A. B. Markov and V. P. Rotshteĭn, Fiz. Khim. Obrab. Mater. No. **6**, 37 (1997).

[4] Yu. F. Ivanov and S. F. Gnyusov, Izv. Vyssh. Uchebn. Zaved. Fiz. No. **8**, 104 (1996).

[5] D. S. Nazarov, G. E. Ozur, and D. I. Proskurovskiĭ, Prib. Tekh. Éksp. No. **4**, 83 (1996).

[6] S. F. Gnyusov, S. N. Kul'kov, Yu. F. Ivanov *et al.*, Izv. Vyssh. Uchebn. Zaved. Fiz. No. **2**, 26 (1994).

[7] D. I. Proskurovsky, V. P. Rotshtein, G. E. Ozur *et al.*, J. Vac. Sci. Technol. A **16**, 2480 (1998).

[8] E. F. Dudarev, G. P. Pochivalova, D. I. Proskurovskiĭ *et al.*, Izv. Vyssh. Uchebn. Zaved. Fiz. No. **3**, 126 (1996).

Nonlinear effects in yttrium ceramic in a nonsteady-state magnetic field

V. E. Miloshenko, I. M. Golev, and A. A. Voronov

Voronezh State Technical University
(Submitted June 7, 1999)
Pis'ma Zh. Tekh. Fiz. **25**, 60–63 (October 26, 1999)

Nonlinear electrodynamic properties in granular superconductors are studied for the case of yttrium ceramic in a nonsteady-state magnetic field and in the current state. A substantial increase in the amplitude of their even harmonics is observed. It is shown that the nonlinear properties are determined by an ensemble of vortices in the surface layer of the superconductor and depend on external influences. © *1999 American Institute of Physics.*
[S1063-7850(99)02610-5]

High-temperature superconductors are known to exhibit nonlinear effects[1,2] which account for the considerable interest shown in the application of these materials to cryoelectronics devices and navigation technology.

In the present study we used an inductive method to investigate the nonlinear properties of yttrium ceramic. We measured the harmonic components of the response signal of the superconductor to a low-frequency ac magnetic field.

We used samples of $Y_1Ba_2Cu_3O_{7-\delta}$ ceramic prepared by solid-phase synthesis, having a critical temperature of 93 K and measuring $3\times5\times15$ mm. These were exposed to an ac field of amplitude $h\leqslant10^{-2}$ Oe and frequency $f=10^2-10^4$ Hz superposed on a dc magnetic field $H = 0$–500 Oe at liquid nitrogen temperature. The dc magnetic field could be increased or decreased.

It was established that when the field H increases at a rate $V=dH/dt$ higher than 10 Oe/s (we shall call this nonsteady-state), the profile of the response signal becomes substantially distorted with limited amplitude in one half-period. In this case, the coefficient of the response signal harmonics reaches 30%. In a slowly-varying field H ($V<10$ Oe/s) this coefficient did not exceed 4%. The amplitudes of the even harmonics (especially the second U_2) increased substantially in the nonsteady-state field and were

between approximately four and five times those for a slowly increasing field (Fig. 1). The amplitudes of the odd harmonics remained almost unchanged and merely increased very slightly in fields of less than 50 Oe.

The observed characteristics of the nonlinear properties of yttrium ceramic can be attributed to detached vortices starting (in the nonsteady-state case) to migrate into the superconductor. If the field is reduced (reverse motion), the vortices migrate in the opposite direction. The observed generation of even harmonics is determined by the processes taking place in the surface layer and the vortex migration in this layer is determined by the surface barrier.[3] The barrier may be reduced, for example, by depositing a normal metal on the surface of the superconductor. In this case, changes should be observed in the amplitude of the even harmonics. Experiments carried out using indium-coated samples revealed a drop in the amplitude of the even harmonics (for example U_2 in Fig. 1, curve *3*). The amplitudes of the odd harmonics remained almost the same.
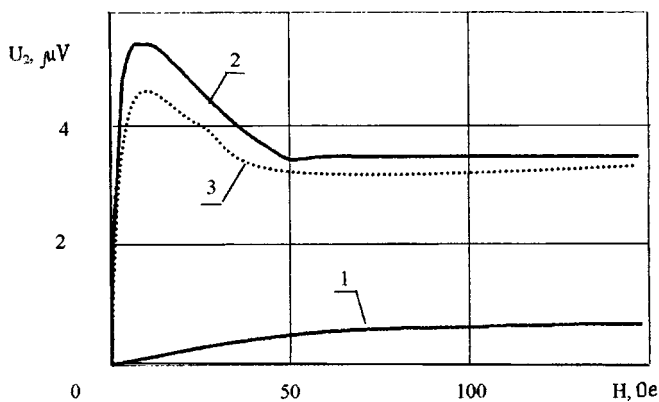

FIG. 1. Influence of the sweep rate of the dc field on the magnetic field dependence of the second harmonic: *1* — 0.8 Oe/s, *2* — 25 Oe/s for yttrium ceramic, *3* — 25 Oe/s for indium-coated yttrium ceramic; h = 0.008 Oe, f = 1 kHz.
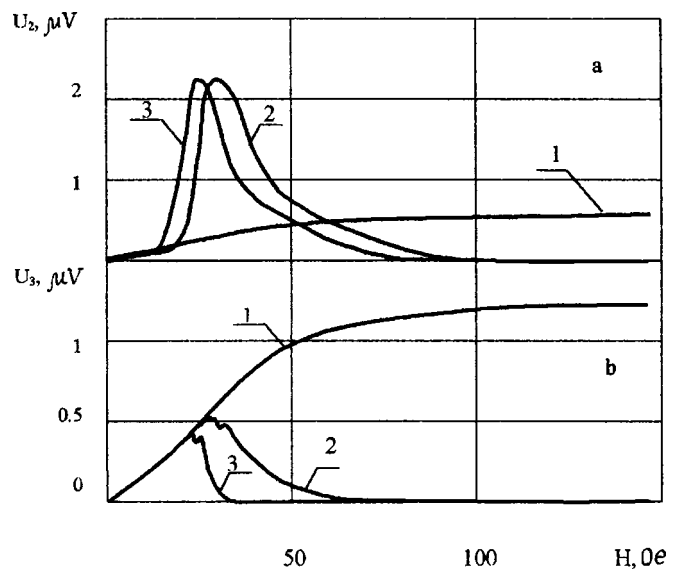

FIG. 2. Influence of the transport current on the magnetic field dependences of the U_2, U_3 response signal at $V=0.8$ Oe/s: *1* — $I_T=0$, *2* — 0.3 A, *3* — 0.4 A, h = 0.008 Oe, and f = 1 kHz.

Thus, having established a correlation between the response and the vortex motion, we applied a transport current I_T to these in different directions. In one case, a current was only passed along one face of the sample while in another, current was passed over both faces but in the same direction. We observed that for specific values of I_T and H, the second U_2 and third U_3 harmonics are also generated (Fig. 2). Their positions are determined by the current: as the current density increases, the maxima are shifted toward lower magnetic fields (curves *2* and *3*) and, as was to be expected, reversal of the transport current causes the phase of the even harmonics to rotate through 180°, as we observed when the direction of the field was changed. Thus, in both experimental scenarios vortex migration stimulates the generation of even harmonics.

In order to obtain further confirmation of this idea, we carried out experiments in which currents of the same magnitude but in the same direction were passed along opposite faces of the sample, i.e., in this case, the transport current initiates vortex motion; near one of the faces the vortices migrate inward whereas at the other they migrate toward the surface. The even-harmonic signals are in antiphase and naturally should not be observed using a measuring coil. In this situation no even harmonics were observed although in the absence of current, the dependence $U_2(H)$ was similar to the previous one. As was predicted, the behavior of the dependences $U_3(H)$ remained the same.

To sum up, these experimental investigations of the nonlinear properties of superconductors using yttrium metal oxides have shown that the generation of even harmonics in the response signal to a nonsteady-state magnetic field is related to the dynamics of an ensemble of vortices in the surface layer of the superconductor. The phase of these harmonics is determined by the direction of collective motion of the vortices. By varying the external influences, such as the magnetic field sweep rate, the magnitude and direction of the transport current, and so on, it is possible to control the nonlinear effects in superconductors.

[1] V. A. Atsarkin, G. A. Vasneva, V. V. Demidov *et al.*, Sverkhprovodimost' **3**, 1643 (1990).
[2] L. Ji, R. H. Sohn, G. C. Spalding *et al.*, Phys. Rev. A **40**, 10 936 (1989).
[3] V. E. Miloshenko, I. M. Shushlebin, A. N. Dynin *et al.*, Sverkhprovodimost' **3**, 2587 (1990).

Translated by R. M. Durham

Kinetic growth characteristics of a single dendrite during crystallization from a solution

E. G. Aksel'rod, L. M. Martyushev, and E. V. Levkina

Institute of Industrial Ecology, Russian Academy of Sciences, Ekaterinburg
(Submitted April 13, 1999)
Pis'ma Zh. Tekh. Fiz. **25**, 64–70 (October 26, 1999)

The behavior kinetics of the transition rate during free quasitwo-dimensional growth of a single dendrite from an aqueous NH_4Cl solution is studied experimentally. It is established that the integral curves are described by a Weibull distribution and the possibility of applying the Kolmogorov–Avrami theory to describe the kinetics of dendritic crystallization is discussed. Small-amplitude oscillations of the growing dendrite mass are observed against the background trend, having a quasiperiodic nature with a frequency around 0.1 Hz. The nature of these oscillations is related to the interaction between the diffusion fields of existing and newly forming secondary branches. © *1999 American Institute of Physics.*
[S1063-7850(99)02710-X]

The kinetic behavior of advanced dendritic growth (with the appearance of secondary branches) has not attracted sufficient attention, and it is frequently implicitly assumed that this is very similar to the dependences obtained for an acicular crystal.[1] However, this viewpoint only holds in the first approximation. In an experimental study[2] and in studies using computer modeling and numerical calculations,[3,4] it was observed that the growth rate of the primary dendrite branch exhibits small-amplitude oscillations and the frequency of these oscillations is related to the appearance of secondary branches (here and subsequently we always have in mind dendrite growth in the $\langle 100 \rangle$ direction). The authors of Refs. 2–4 postulated that these oscillations are caused by the action of the diffusion field of an incipient secondary branch on the local supersaturation near the primary dendrite branch. If the proposed mechanism is correct, it may be predicted that the diffusion field of the incipient secondary branch, by influencing the growth of existing secondary branches, may lead to characteristic features in the time behavior of the entire growing dendrite mass. However, no experimental data are available on the kinetics of the change in mass and the existence of nonrandom oscillations of the crystallization rate during growth of a single dendrite. In the present paper these kinetic growth characteristics of a dendritic structure are studied experimentally.

The dendritic growth system was an aqueous solution of ammonium chloride (NH_4Cl) whose morphological and kinetic crystallization parameters were described in Refs. 2,5, and 6. We used a polarization interference microscope with photometric adapter. As a result of a difference between the refractive indices of the dendrite and the solution, a difference was observed in the intensity of the interference color of these phases. A polarization attachment intensified the interference contrast. Using a combined polarization-interference system substantially improved the sensitivity. The dendrite growth took place under quasitwo-dimensional conditions (using a planar capillary whose thickness was much less that the diffusion length $2D/v \approx 400 \, \mu m$, where v and D are the growth rate and the diffusion coefficient of the

dendrite,[6] respectively) and the change in the mass of the growing dendrite was directly proportional to the change in its area in the plane of the cell. The integrated light flux passing through the sample and incident on the photodetector was proportional to the ratio of the areas occupied by the solution and the crystal. As a result of a change in the area occupied by the crystalline phase, the light flux incident on the detector, an FD-7K photodiode, was modulated. In order to reduce the dark current to 0.1 μA, the photodiode was placed in a special thermostatically controlled, electrically shielded casing. An important factor for improving the measurement accuracy was that the eyepiece with the photodiode was positioned such that the exit image of the microscope eyepiece was projected onto the photocathode surface ($1.0 \, cm^2$). This made it possible to follow the real area of the growing crystal visible in the eyepiece. The signal from the photodetector ($\sim 20 \, \mu A$), operating in the photodiode regime was fed to an electrometric amplifier having a gain of 10^8. The amplifier output signal was recorded in analog and digital forms. Additional calibration showed that the lux–ampere characteristic of the photodiode was linear over the working section.

The prepared NH_4Cl solution, having concentrations of 43.6, 41.4, and 40.1 (g/100 g H_2O), corresponding to saturation temperatures of 35, 30, and 27 °C, was placed between two cover glasses on the microscope stage of a BIOLAR PI microscope. For the experiments we used a $1.0 \, cm^2$ cell whose thickness was 40–50 μm. The cell was held at a temperature 2 °C higher than the saturation temperature for at least 10 min. The planar capillary with the sample was then cooled rapidly to 20 °C. As a result of using thin cover glasses with a small thickness of solution between them, the cell acquired this temperature within 2–3 s. Visible dendrite growth began within 20–30 s and thus occurred under conditions of uniform concentration and temperature. The temperature fluctuations of the solution at the stage of active dendrite growth did not exceed 0.01 °C. The selected magnification (110×) was sufficient to observe a single primary dendrite branch; the field of view contained up to 30–40
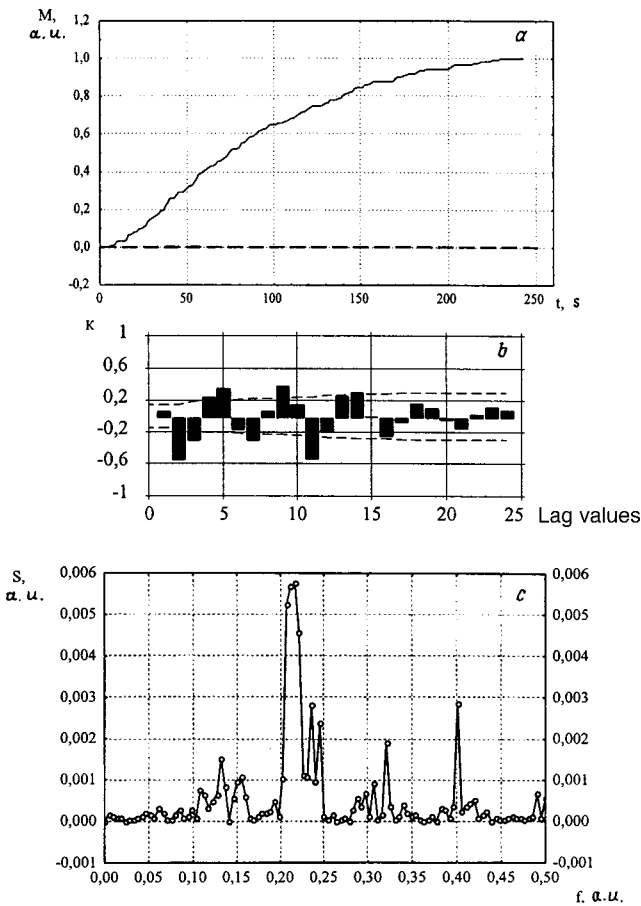
TABLE I. Averaged parameters of experimental curves approximated by a two-parameter Weibull distribution.

Temperature, °C	c	d	R	F
27	0.0030 ± 0.0030	1.6 ± 0.4	0.993 ± 0.006	0.25 ± 0.18
30	0.0008 ± 0.0007	1.8 ± 0.2	0.992 ± 0.004	0.22 ± 0.12
35	0.0031 ± 0.0021	1.5 ± 0.1	0.995 ± 0.003	0.15 ± 0.09

FIG. 1. Typical experimental curve showing the change in mass M of a growing dendrite with time t. For this curve we have $c = 0.0016$, $d = 1.4$, $R = 0.999$, and $F = 0.03$ (for explanation see text). The noise curve in the absence of growth is shown by the dashed curve (a). Autocorrelation function (b) and periodogram (c) of the oscillating component of the experimental series (a). Here K is the normalized autocorrelation coefficient, S is the spectral density, and f is the frequency.

secondary branches. The mass measurements were made for a single freely-growing dendrite located at a distance of at least the diffusion length from neighboring dendrites.

At all the saturation temperatures used experimentally, dendrite growth was observed with secondary branches oriented in the $\langle 100 \rangle$ direction. No tertiary branches formed at these supersaturations and no appreciable enlargement of the interbranch gaps occurred during growth. A total of 33 samples were investigated. It was reliably established that for all the supersaturations used in these experiments the time dependence of the dendrite mass was S-shaped and all the experimental growth curves revealed typical small-amplitude oscillations of the transition rate against the background trend. A typical curve of the transition rate is plotted in Fig. 1a.

The Curve Expert 1.3.1 package was used to show that the experimental curves are best approximated by a two-parameter Weibull distribution:

$$q = 1 - \exp(-ct^d), \tag{1}$$

where q is the volume fraction of the solid phase, t is the time, and c and d are constants. The averaged values of the parameters c and d, and also the correlation coefficients R

and the loss function F for the distribution used are given in Table I. Note that the regression dependences of the experimental curves (*1*) agree with the equation obtained in the Kolmogorov–Avrami theory for the quantity of the crystallized phase during mass crystallization.[7] This allows us to formulate a hypothesis on the validity of the Kolmogorov–Avrami theory to describe the growth kinetics of a single dendrite. In fact, one possible particular case described by this theory is the uniform time- and spatially-constant nucleation of new-phase nuclei where the growth of each of these nuclei is controlled by diffusion (the linear dimensions increase proportionally with the square root of the time).[7] During free dendrite growth these developing nuclei may be considered to be incipient new secondary branches. These branches form at approximately the same time intervals on the growing primary branch and their growth is then diffusion-controlled.[5] The shape of these branches may be considered to be acicular and thus these "nuclei" (secondary branches) are one-dimensional. According to the Kolmogorov–Avrami theory, the exponent of the time should be 1.5 under these conditions. Note that the experimentally determined parameter d is close to this value (Table I). By analyzing these dependences in terms of the Kolmogorov–Avrami theory, we can also explain the experimentally observed spread of the parameter c (Table I). This parameter is responsible for the transition kinetics (unlike the parameter d which is responsible for the growth geometry). Since in each series of experiments the time dependence of the dendrite mass was measured at different stages of growth, the values of the parameter c revealed a large spread. Additional experiments under conditions different to those of the present study are required to determine the parameter c accurately.

In order to determine whether the observed oscillations of the transition rate are nonrandom, we made a statistical analysis in which we calculated the autocorrelation functions and periodograms using the Statistica 5.0 statistical package. A typical autocorrelation function of the transition rate oscillations of a time series is plotted in Fig. 1b. It can be seen that eight lag values exceed the 95% confidence limit, which indicates that there is some regularity in the time series. The average lag values for the experimental results are shown in Table II. The fact that the confidence limit is exceeded by an average of four lags suggests that these time series are not random. A typical periodogram for the oscillation component of the experimental curve in Fig. 1a is plotted in Fig. 1c. The periodograms show clearly defined isolated peaks which indicate the presence of a deterministic (oscillating) component. The average periods of the oscillations responsible for

TABLE II. Parameters of transition rate oscillations.

Temperature, °C	Average lag values, exceeding 95% confidence limit	Average period of oscillations, s
27	6±2	9.4±0.6
30	4±1	9.0±0.5
35	4±1	9.0±0.4

the peaks having the largest amplitudes are also given in Table II.

The results indicate that the time series has an oscillating component with an average period of 9 s. Note that the time of appearance of the next secondary branch during the dendrite growth varied between 6.0 and 7.5 s according to the experimental results. Hence, the period of the observed oscillating component in the experimental time series is close to the time interval between the appearance of neighboring secondary branches. However, we stress that these nonrandom oscillations are not directly related to the appearance of secondary branches since they were also observed under conditions where the end of the primary branch with incipient secondary branches was outside the field of observation. The existence of these nonrandom oscillations may be explained as follows. It was shown in Refs. 2–4 that small-amplitude oscillations of the growth rate of the primary branch are associated with the perturbation of the periodically appearing secondary-branch diffusion field near the primary branch. However, the diffusion field of the incipient secondary branch also acts periodically on the existing secondary branches. We shall show that the time of appearance of the next secondary branch t_1 is an order of magnitude greater than the characteristic time of propagation of the diffusion field from an already-formed secondary branch t_2. According to the experimental data, the dendrite growth rate is of the order of 10 μm/s and the distance between the secondary branches L is of the order of 10 μm so that $t_1 \sim 1$ s. The diffusion coefficient of ammonium chloride D is around 1000 μm^2/s (Ref. 2) and thus $t_2 \sim L^2/D = 0.1$ s. It can therefore be considered that the influence of the diffusion field spreads almost instantaneously from the incipient secondary branch to existing branches compared with the time of appearance of the next secondary branch. As a result of this complex interaction between the diffusion fields of the secondary branches, the time variation of the growing dendrite mass exhibits periodicity. This reasoning indicates that in principle, small-amplitude oscillations of the growing dendrite mass may be initiated by an incipient secondary branch.

[1] E. A. Brener and V. I. Melnikov, Adv. Phys. **40**, 53 (1991).
[2] E. Raz, S. Lipson, and E. Polturak, Phys. Rev. A **40**, 1088 (1989).
[3] O. Shochet, K. Kassner, E. Ben-Jacob *et al.*, Physica A **187**, 87 (1992).
[4] P. K. Galenko, M. D. Krivilyov, and S. V. Buzilov, Phys. Rev. E **55**, 611 (1997).
[5] S. -K. Chan, H. H. Reimer, and M. Kahlweit, J. Cryst. Growth **32**, 303 (1976).
[6] L. Jan-Ming, L. Zhi-Guo, and W. Zhuang-Chun, Scr. Metall. Mater. **32**, 445 (1995).
[7] L. Mandel'kern, *Crystallization of Polymers*, Khimiya, Moscow (1966), 336 pp.

Translated by R. M. Durham

Self-similarity in the kinetic growth regime of a crystal in a phase-separating medium

L. M. Martyushev and V. D. Seleznev

Institute of Industrial Ecology, Russian Academy of Sciences, Ekaterinburg

An analysis is made of a simple model of the kinetic growth regime of a crystal possessing cubic symmetry in a phase-separating medium. Impurity diffusion is neglected. It is shown that in this approximation the crystal growth is self-similar. A cellular automaton model is used to represent the successive stages of structural modification as the impurity concentration increases. © *1999 American Institute of Physics.* [S1063-7850(99)02810-4]

Relatively few theoretical studies (using mathematical and computer modeling) have examined the influence of impurities on the morphology of a growing crystal. This is because of the major complexities involved in studying these phenomena.[1–3] The immensity and complexity of the analysis of the growth of crystals with impurities frequently has the result that in most cases highly specialized models are constructed to describe the crystallization of a specific substance under specific conditions.[4–6] These models are not of any great practical value since the phenomenon being modeled has been more or less well studied experimentally and the modeling reduces to a more or less successful approximation. The theoretical value is also low since particular solutions for a nonlinear problem are of no great use (and problems of crystal growth are nonlinear). Thus, there is a need to construct models which possess limiting asymptotic properties characteristic of a wide range of crystallization problems. One such model is the DLA model[7] which is very convenient for describing the influence of diffusion supply on crystal growth. In the present paper we propose to consider the kinetic growth regime as another macroscopic model of crystal growth from an impurity-containing solution. The interaction between the impurity and the crystal is determined only by its phase separation as a result of being completely expelled by the growing surface. It is assumed that local phase separation makes it impossible for the crystal to form at these sites and impossible for any material fluxes to pass through these regions. The impurity diffusion coefficient is taken to be zero. This mechanism of crystallization in a phase-separating medium is in particular a simple model of eutectic formation.[2]

This model is interesting for the following reason. Let us assume that we wish to study the morphology of a growing crystal, for which we need to divide the entire volume of the region being studied into very small cells. We select the cell size bearing in mind the required degree of detail in the description, practical interest, and so on. Inside each cell the crystal characteristics will be uniform. We then use this model to calculate the crystal morphology and obtain a certain structure with an inhomogeneity scale in the selected cell. However, because of the constraints introduced, this structure is scale-invariant. In the kinetic growth regime (assuming that this is conserved as the scale varies), the concentration near the crystal surface is the same and equal to the concentration in the solution. The growth is stable and the crystal retains its shape. The motion of the crystal surface is uniquely determined by the boundary laws but over a wide range of spatial scale, these are the same since we are using a macroscopic deterministic description (in the kinetic regime the growth kinetics are completely determined by the kinetic crystallization coefficient).[3] Since the impurity diffusion coefficient is zero, its bulk distribution is the same and equal to the initial distribution. Impurity expulsion does not depend on scale because of the scale invariance of the laws of motion of the crystal surface. Let us now assume that we need to calculate the growth of the same crystal having a smaller or larger characteristic size (earlier or later stages of growth, respectively). We again divide the new characteristic size into cells where the number of these cells remains the same as before (i.e., we wish to study this crystal size with the same degree of detail as in the previous case). However, since the crystal calculation rules also remain the same, the calculations obviously give a structure exactly the same as the previous one. Only the inhomogeneity scale changes while the crystal morphology remains the same.

Thus, in this formulation the growth of the structure is self-similar over a wide range of spatial scales, ranging from fairly small (several radii of the critical nucleus) to relatively large (the size of a stable polyhedron growing from solution). Having studied one of the scales of the structure, we therefore know everything about the morphology in the other scales (under a different microscope magnification). We stress that only the central part of the crystal is self-similar (specifically, when looking into the growth center we shall see the same pattern under different magnifications). Thus, only self-similarity exists[8] and not fractality[9] when each part of the structure is similar to the whole (like aggregates in DLA models). The "absolute" self-similarity of this model must naturally be considered as a property of model computer calculations using mesh models. In real systems crystallizing under conditions close to the model ones, the self-similarity should be understood in the statistical sense.

Self-similar regimes during crystal growth from a solution were identified earlier under certain conditions. The classical problem of self-similar growth involves the growth of a spherical crystal under diffusion-limited conditions

(Scriven–Kirkaldy) problem) which has been solved analytically.[10] In the present study self-similarity occurs in the kinetic crystallization regime in the presence of an impurity with a zero diffusion coefficient. This self-similarity occurs because the characteristic lengths determining the microstructure scales and microstructural transitions disappear from the problem.[11]

We shall use a cellular automaton model constructed on the basis of the following rules to simulate the growth conditions described above.

1. The calculations are made using an $N \times N$ square lattice where N is a positive integer. The choice of a square lattice assumes that it is possible to model the growth of crystals with cubic symmetry. The cell size is in some sense arbitrary, having an upper limit of $1/N^2$ of the critical stability dimension of the forming crystal and a lower limit of the critical nucleus. To be specific, a square, two-dimensional lattice is selected in the present study and by analogy the model can be constructed for a three-dimensional lattice and different symmetry. Testing the program showed that it is meaningless to select N greater than 100 since the crystal ''figure'' is repeated.

2. It is assumed that the crystal begins to grow at the center of the lattice. Since the kinetic growth regime is being analyzed, the concentration of the solution at the apexes and at the center of the crystal faces is the same and equal to the bulk concentration[3] so that an extremely simple rule can be applied for modeling: all cells very close to the crystal are colored black over a single cycle if this is not forbidden by the properties of the second component (see below).

3. Each cell has a concentration of the second (impurity) component C_i which is the same and equal to $C_{i,\text{in}}$ for all the cells. During growth (coloring the next cell black) the crystal expels impurity to the nearest cells and the lower the impurity content in the neighboring cell, the larger the fraction of impurity transferred to it (the mass conservation law should be satisfied for the impurity).

4. We shall assume that when the impurity reaches a specific concentration $C_{i,c}$, it is transferred to a different phase and this is expressed as the prohibition of fluxes passing through this cell and the impossibility of salt crystallizing in it. These cells are colored gray. In the present study we also introduce the simplifying hypothesis that when $C_i < C_{i,c}$ impurities have no influence on the crystallization of the salt.

The model considered here is a limiting simplification of the τ-model[12,13] because rules involving the calculation of diffusion fluxes are completely excluded.

The model constructed above has only a single control parameter, the relative impurity content $C_{i,\text{in}}/C_{i,c}$. For $C_{i,\text{in}}/C_{i,c} \to 0$ the crystal is ideally cubic. We shall analyze crystal growth as the impurity content gradually increases. For $C_{i,\text{in}}/C_{i,c} \leqslant 0.05$ the crystal, while remaining broadly homogeneous, begins to contain small regions of phase-separated impurity during the growth process (see Fig. 1a). As a result of being expelled, these inclusions build up in the central part of the growing crystal. As the relative concentration increases, the impurity begins to precipitate out at increasingly early stages of growth and its distribution ac-
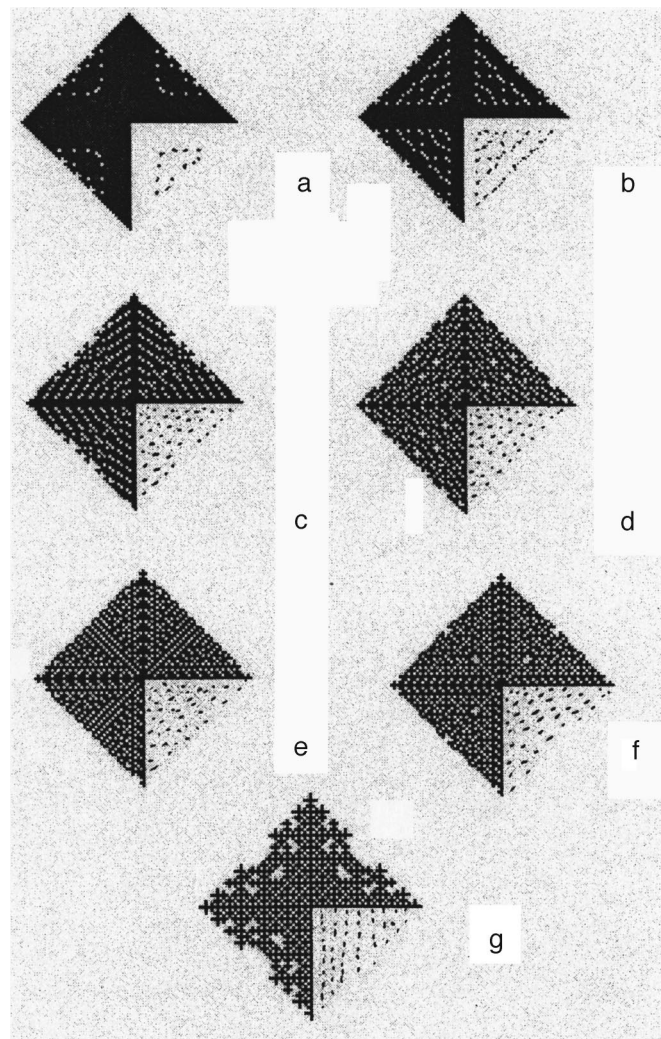

FIG. 1. Crystal morphology for various relative initial impurity concentrations $C_{i,\text{in}}/C_{i,c}$ 0.05 (a), 0.10 (b), 0.22 (c), 0.34 (d), 0.36 (e), 0.41 (f), and 0.55 (g). The black color shows the salt distribution while the gray shows the phase-separated impurity; in the right lower quadrant only the impurity distribution is shown for convenience.

quires a clearly defined layered character (see Fig. 1b). As $C_{i,\text{in}}/C_{i,c}$ increases further, the distance between the layers formed by the phase-separated impurities decreases and their density in these layers increases (see Fig. 1c). At the same time the homogeneous region without impurities becomes increasingly narrow.

At a relative impurity concentration in the region of 0.34 the layered appearance disappears from the impurity distribution and pores also appear (internal regions of crystal occupied by solution and surrounded by phase-separated impurity) (see Fig. 1d). The entire crystal becomes quasi-isotropic.

A slight increase in the ratio $C_{i,\text{in}}/C_{i,c}$ to 0.36 is accompanied by an abrupt change in the internal structure of the crystal (see Fig. 1e) since the phase-separated impurity predominantly begins to be distributed perpendicular to the faces.

A subsequent increase in the relative concentration again produces a uniform isotropic impurity distribution. Figure 1f shows a typical structure for this range of variation of the

control parameter. When the ratio $C_{i,\text{in}}/C_{i,c}$ varies between 0.42 and 0.55, the impurity distribution remains as before although the internal structure of the crystal becomes more regular (see Fig. 1g). The porosity of the crystal increases and the growth boundary changes from relatively smooth to fractal-like. As the impurity concentration increases further ($C_{i,\text{in}}/C_{i,c} \geqslant 0.56$), its separation suppresses crystal growth at an early stage.

These self-similar solutions are asymptotic for entire classes of problems, such as the kinetic growth regime in the presence of an impurity having a relatively low diffusion coefficient, eutectic crystallization, and rapid solidification of a melt. Self-similar solutions (see Fig. 1) may be used as standards for approximate calculations and computer modeling of complex crystallization problems and they accurately reproduce the geometric aspect of the impurity action. The self-similarity considered in the model has been confirmed in experimental studies of systems similar to that proposed in the present study. In particular, self-similarity (self-affine fractal) occurs in the banded distribution of impurities in various minerals.[14,15] This growth characteristic is attributed in Ref. 15 to fluctuations of the external geological conditions during the entire crystal formation time. One of the main arguments for this conclusion was the complexity of developing a different model to explain the observed self-

similarity. On the basis of the present results (see Fig. 1a–1c) self-similarity of the zonal impurity distribution can be explained in terms of the properties of the crystallizing system itself without any external influence, i.e., self-organization.

[1] G. Bakli, *Crystal Growth*, IL, Moscow (1958).
[2] Yu. N. Taran and V. I. Mazur, *Structure of Eutectic Alloys*, Metallurgiya, Moscow (1978), 313 pp.
[3] *Modern Crystallography*, Vol. 3, *Crystal Formation*, Nauka, Moscow (1980), 407 pp.
[4] R. I. Mints, S. A. Skopinov, *et al.*, Zh. Fiz. Khim. **66**, 352 (1992).
[5] Lu Shu-Zu and J. D. Hunt, Acta Metall. Mater. **42**, 1653 (1994).
[6] J. F. McCarthy, Acta Mater. **45**, 4077 (1997).
[7] T. A. Witten and L. M. Sander, Phys. Rev. B **27**, 5686 (1983).
[8] G. I. Barenblatt, *Similarity, Self-Similarity, and Intermediate Asymptotics* (Consultants Bureau, New York, 1979; Gidrometeoizdat, Leningrad 1982, 220 pp.).
[9] E. Feder, *Fractals* (Plenum Press, New York, 1988; Nauka, Moscow, 1991, 260 pp.).
[10] L. E. Scriven, Chem. Eng. Sci. **10**(1), 1 (1939).
[11] R. Trivedi, Mater. Sci. Eng., A **178**, 129 (1994).
[12] L. M. Martyushev, V. D. Seleznev, *et al.*, Pis'ma Zh. Tekh. Fiz. **22**(16), 12 (1996) [Tech. Phys. Lett. **22**, 648 (1996)].
[13] L. M. Martiouchev, V. D. Seleznev *et al.*, J. Stat. Phys. **90**, 1413 (1998).
[14] N. M. Halden and F. C. Hawthorne, Am. Mineral. **78**, 1113 (1993).
[15] T. Holten, B. Jamtveit, P. Meakin *et al.*, Am. Mineral. **82**, 596 (1997).

Translated by R. M. Durham

Microwave phase shifter with planar capacitors using strontium titanate films

A. Kozyrev, A. Ivanov, O. Soldatenkov, E. Gol'man, A. Prudan, and V. Loginov

St. Petersburg State Electrotechnical University
(Submitted May 18, 1999)
Pis'ma Zh. Tekh. Fiz. **25**, 78–83 (October 26, 1999)

A design of a microwave phase shifter based on a loaded microstrip line using planar $SrTiO_3$ capacitors as nonlinear elements is described. The microwave phase shifter (at $T = 300$ K) demonstrated a continuous phase shift between 0 and ~ 55 deg in the frequency range 8.6–9.0 GHz with a phase error not exceeding 5 deg. The quality parameter of the phase shifter in the operating frequency range was 110 deg/dB. © *1999 American Institute of Physics.*
[S1063-7850(99)02910-9]

The nonlinear properties of ferroelectric materials such as strontium titanate $SrTiO_3$ and barium strontium titanate $(Ba,Sr)TiO_3$ can be used to design electrically controllable microwave devices (tunable resonators and filters, phase shifters, and so on).[1,2] Previous studies of ferroelectrics have demonstrated their high speed[3] and their capacity to operate at high microwave powers without any substantial degradation of the dielectric properties.[4] Bearing in mind the relatively low cost of ferroelectric nonlinear elements compared with similar semiconducting and ferrite components, we note that these may be potentially useful for the microwave range. Ferroelectric nonlinear elements for microwave devices operating at room temperature are usually based on $(Ba,Sr)TiO_3$ films. However, the fairly strong temperature dependence of the permittivity and the relatively high level of microwave dielectric losses in these materials[5] limit their application in the microwave range at $T = 300$ K. Strontium titanate films are used at cryogenic temperatures ($T \leqslant 77$ K) (Ref. 2). Nevertheless, the nonlinearity of the permittivity of $SrTiO_3$ in high static electric fields was recently demonstrated by the authors of Refs. 6–8 at $T = 300$ K and low frequencies. The present study demonstrates for the first time the use of $SrTiO_3$ films in electrically controlled microwave devices at $T = 300$ K. Here we report results of an investigation of the characteristics of a microwave phase shifter using planar $SrTiO_3$ capacitors.

MICROWAVE PROPERTIES OF SrTiO₃ CAPACITORS

Strontium titanate films were prepared by rf magnetron sputtering of a stoichiometric target in an $0.7 O_2 - 0.3$ Ar atmosphere at pressure $P = 4$ Pa. The substrates for the planar capacitors were prepared using single-crystal sapphire (r-cut). The substrate temperature ($T = 700°C$) was kept constant during the film deposition process. After the required thickness of $SrTiO_3$ film had been reached ($h = 0.8 \mu$m), deposition ceased and the samples were cooled to room temperature at a rate of ~ 10 deg/min. Before depositing the $SrTiO_3$ film, platinum (Pt) electrodes were formed on the substrate surface by photolithography. The gap between the electrodes was $g = 4 \mu$m. After the film had been deposited, the multilayer $SrTiO_3$/Pt(electrodes of the planar capacitor)/Al_2O_3 system was annealed in air for 2 h at $T = 1050°C$. The technology used to fabricate the multilayer structures containing a thin $SrTiO_3$ film was described in greater detail in Ref. 8. The nonlinearity and dielectric losses of the $SrTiO_3$ capacitors were estimated by a resonance technique[5] at frequency $f \sim 10$ GHz and $T = 300$ K. It was established that as the dc bias U_b applied to the capacitors increased to $U_b = 400$ V, their capacitance decreased by a factor of 1.8. The Q factor of the capacitors $Q \sim 70$ ($Q = 1/\tan \delta$, where $\tan \delta$ are the dielectric losses) increased slightly, by no more than 10%, with increasing bias.

TOPOLOGY OF MICROWAVE PHASE SHIFTER

The topology of the microwave phase shifter is shown in Fig. 1. Two parallel LC circuits containing planar ferroelectric capacitors are incorporated in a microstrip line ($Z_0 = 50 \Omega$). The LC circuits are connected by a section of microstrip line having a lower wave impedance ($Z_{01} = 40 \Omega$) which is required to improve the matching of the phase shifter with the external microwave circuits. The length of the microstrip line connecting the LC circuits is approximately $3\lambda/4$ near the central frequency $f \sim 8.8$ GHz in the operating range of the phase shifter. The planar $SrTiO_3$ capacitors C were placed in the gaps between the microstrip line and radial quarter-wave loops which ensure that the short-circuiting condition is satisfied for the microwave signal in this design of phase shifter. The inductances (L) were sections of microstrip line having a wave impedance $Z = 50 \Omega$ and lengths less than $\lambda/4$ and were shorted with respect to the microwave signal using the radial quarter-wave loops. A dc bias U_b is supplied to the planar capacitors via thin ($\sim 10 \mu$m) silver (Ag) wires soldered to the radial loops and the microstrip line of the phase shifter.

MICROWAVE CHARACTERISTICS OF PHASE SHIFTER

The frequency dependences of the transmission coefficient S_{21} and the phase shift $\Delta\varphi$ of the microwave phase shifter are plotted in Figs. 2a and 2b. The measurements were made at $T = 300$ K. A dc bias $U_b = 0–400$ V was applied to the planar $SrTiO_3$ capacitors. At the central frequency of the operating range, the insertion losses of the
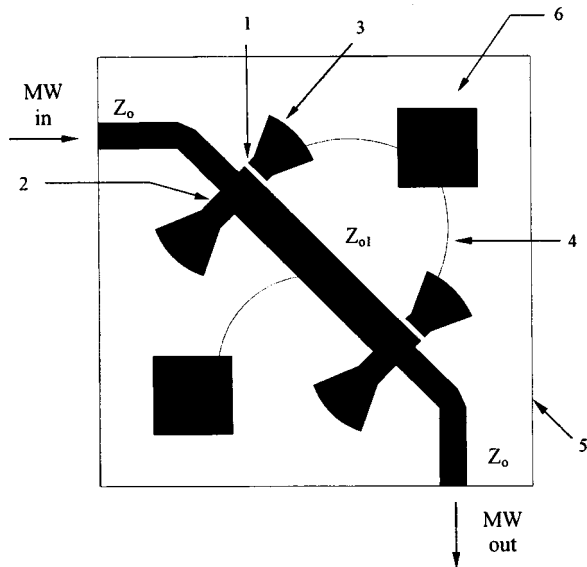
FIG. 1. Topology of a two-element phase shifter. Substrate dimensions — $16.4 \times 16.4 \times 1.0$ mm: *1* — gap for planar capacitor, *2* — microstrip inductance, *3* — quarter-wave radial loop, *4* — 10 μm wire, *5* — substrate (polikor Al_2O_3), and *6* — contact areas to supply dc voltage.

FIG. 2. Microwave characteristics of two-element phase shifter using planar $SrTiO_3$ capacitors as nonlinear elements.

phase shifter did not exceed 0.5 dB and varied little with increasing bias (Fig. 2a). It should be noted that the measurement error for the transmission coefficient does not exceed ± 2 dB. Measurements of the reflection coefficient S_{11} in the frequency range 8.6–9.0 GHz gave $S_{11} = -13$ dB which corresponds to losses of approximately 0.2 dB in the phase shifter as a result of reflection of the microwave signal. Thus, the additional losses of the order of 0.3 dB are caused by the losses in the planar $SrTiO_3$ capacitors and the microstrip line of the phase shifter. The losses in the substrate (Al_2O_3) and the radiation losses are negligible for this design. The measured phase shift of the microwave signal in the frequency range 8.6–9.0 GHz varied between 0 and ~ 55 deg for voltages of 0–400 V (Fig. 2b). In this case, the maximum phase error was less than 5 deg in the operating frequency range. Taking into account the damping of the microwave signal introduced by the phase shifter ($S_{21} = -0.5$ dB), the quality parameter may be determined as 110 deg/dB.

CONCLUSIONS

It has been demonstrated experimentally that ferroelectric capacitors using $SrTiO_3$ films may be used as nonlinear elements in electrically controlled microwave devices operating at room temperature. The microwave phase shifter with planar $SrTiO_3$ capacitors studied here demonstrated a continuous phase shift (0–55 deg) in the operating frequency range and a quality parameter of 110 deg/dB.
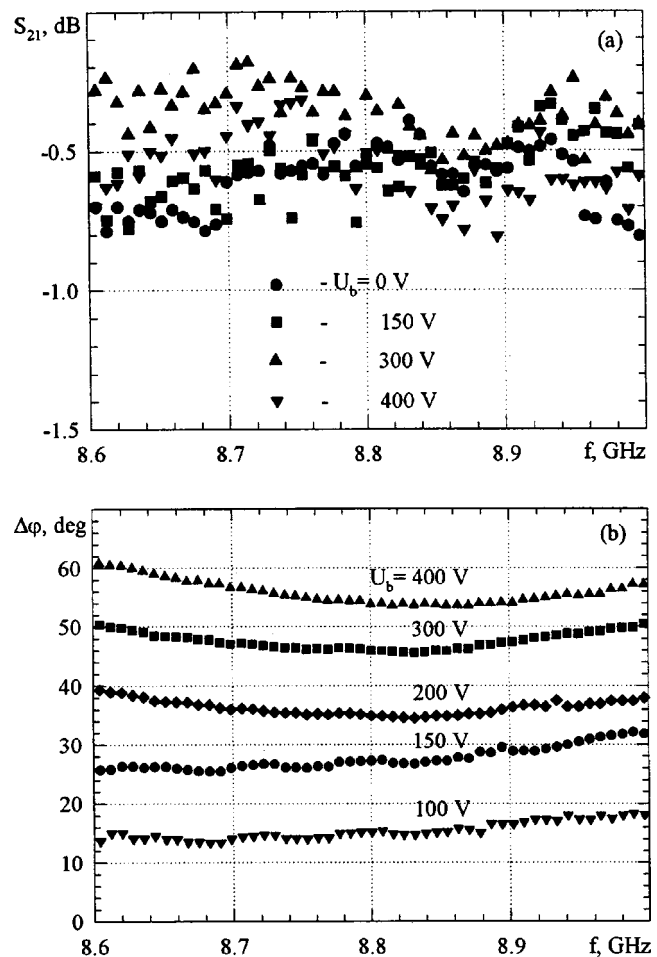
[1] V. K. Varadan, D. K. Ghodgaonkar, V. V. Varadan, J. F. Kelly, and P. Glikerdas, Microwave J., 116 (1992).

[2] G. Subramanyam, F. Van Keuls, and F. A. Miranda, IEEE Microwave Guid. Wave Lett. **8**, 78 (1998).

[3] A. B. Kozyrev, O. I. Soldatenkov, and A. V. Ivanov, Pis'ma Zh. Tekh. Fiz. **24**(19), 19 (1998) [Tech. Phys. Lett. **24**, 755 (1998)].

[4] A. B. Kozyrev, O. I. Soldatenkov, T. B. Samoilova, A. V. Ivanov, G. A. Koepf, C. H. Mueller, and T. V. Rivkin, in *Power Handling Capability and Response Time of Microwave Controlling Devices Based on Ferroelectric Films, Proceedings of the International Symposium on Integrated Ferroelectrics*, 1998 (in press).

[5] A. B. Kozyrev, V. N. Keis, G. Koepf, R. Yandrofski, O. I. Soldatenkov, K. A. Dudin, and D. P. Dovgan, Microelectron. Eng. **29**, 257 (1995).

[6] K. Abe and S. Komatsu, Jpn. J. Appl. Phys., Part 2 **32**, L1157 (1993).

[7] A. M. Prudan, E. K. Gol'man, A. B. Kozyrev, A. A. Kozlov, and V. L. Loginov, Pis'ma Zh. Tekh. Fiz. **24**(9), 8 (1998) [Tech. Phys. Lett. **24**, 332 (1998)].

[8] A. M. Prudan, E. K. Gol'man, A. B. Kozyrev, A. A. Kozlov, V. E. Loginov, and A. V. Zemtsov, Fiz. Tverd. Tela (St. Petersburg) **40**, 1473 (1998) [Phys. Solid State **40**, 1339 (1998)].

Translated by R. M. Durham

Distribution of screening currents in thin superconducting films

D. Yu. Vodolazov

Nizhniĭ Novgorod State University, Nizhniĭ Novgorod

A theoretical analysis is made of the magnetic field screening in thin superconducting films in the Meissner state. Simple approximations are derived for the current density distribution over the film thickness which are everywhere analytical and satisfy the initial equations with a high degree of accuracy. This approximation can be used to determine the demagnetization factor of the film and to estimate the magnetic field for entry of the first vortices into the sample. © *1999 American Institute of Physics.* [S1063-7850(99)03010-4]

Studies of the magnetic characteristics of thin superconducting films in a perpendicular magnetic field [such as the ac (field) susceptibility, magnetization, and so on] require a knowledge of the screening current and magnetic field distribution over the film width. At present, simplified expressions for the screening current density[1] obtained using quasi-one-dimensional models (see, for example, Ref. 2) are used to analyze the experimental data and for quantitative calculations. The screening current distribution thus determined has a root singularity at the edge of the film which prevents the true magnetization factor of the superconducting films from being determined. Moreover, one-dimensional models cannot be used to calculate the screening current and magnetic field distribution in films of finite thickness d.

In the present study, a numerical solution of the Ginzburg–Landau equation for the vector potential $\mathbf{A}$ is used as the basis to study the Meissner state of a thin ($d < \lambda$, where λ is the London penetration depth) superconducting film of width W in a perpendicular magnetic field. The numerical solutions obtained for $\mathbf{A}$ (over a wide range of values of the parameter $0.005 < \lambda_{\text{eff}}/W < 5$, $\lambda_{\text{eff}} = \lambda^2/d$) were used to construct a simple approximation for the vector potential $\mathbf{A}(\mathbf{r})$ [and the current density $\mathbf{j}(\mathbf{r})$].

For analyses of the Meissner state the Ginzburg–Landau equation for $\mathbf{A}(\mathbf{r})$ (in dimensionless units: $A \to \Phi_0/2\pi\xi$, $j \to c\Phi_0/8\pi^2\lambda^2\xi$, $r \to \xi$, where Φ_0 is the magnetic flux quantum and ξ is the coherence length) reduces in practice to the London equation:

$$\Delta \mathbf{A} = \frac{\mathbf{A}}{\kappa^2}, \qquad (1)$$

where $\kappa = \lambda/\xi$ is the Ginzburg–Landau parameter and it is assumed that the film is infinite in the x direction. In addition, Eq. (1) was obtained assuming that the order parameter of the superconducting condensate $\Psi(\mathbf{r})$ is everywhere unity. Numerical calculations show that this last assumption holds over a wide range of fields $H < H_s$, where H_s is the field for which vortices begin to enter the film. Allowance for local suppression of Ψ near the film edges merely yields negligible corrections, of the order of a few percent, for $\mathbf{A}(\mathbf{r})$ when $H \approx H_s$. It follows from the symmetry of the problem

that only the x component of the vector potential $\mathbf{A}$ is nonzero: $\mathbf{A} = (A_x, 0, 0)$ (since the superconducting current only flows in the x direction) and the Laplacian in Eq. (1) is two-dimensional (since the system is homogeneous in the x direction). The following boundary conditions are used:

$$\left.\frac{\partial A_x}{\partial y}\right|_{y \to \pm\infty} = -H^{\text{ext}}, \qquad \left.\frac{\partial A_x}{\partial z}\right|_{z \to \pm\infty} = 0,$$

where H^{ext} is the external magnetic field.

In this case, it is convenient to convert from the differential equation (1) to its integral analog using the Green function of the two-dimensional Laplace operator:

$$A_x(y,z) = A_x^{\text{ext}}(y) + \frac{1}{2\pi\kappa^2} \int_{-W/2}^{W/2} \int_{-d/2}^{d/2} (\ln|(\mathbf{r}-\mathbf{r}')/$$

$$W|)A_x(y',z')dy'dz'. \qquad (2)$$

Test calculations show that for films of thickness d less than λ, instead of the two-dimensional equation (2), we can use the one-dimensional equation:

$$A_x(y) = -H^{\text{ext}}y + \frac{Wd}{4\pi\kappa^2}$$

$$\times \int_{-W/2}^{W/2} \ln|(y-y')/W|A(y')dy'. \qquad (3)$$

This is because in thin films A_x is almost independent of z. The difference between the numerical solution of Eq. (3) and the solution of Eq. (2) for $d = \lambda/4$ is less than 1% (the largest difference arises at the edge; inside the film the error is negligible). Note that Eq. (3), being differentiated with respect to y, is the same as the one-dimensional variant of the Maxwell–London equation.[1]

By solving Eq. (3) numerically, we obtained an approximation for the vector potential $A_x(y)$ (Fig. 1) which satisfies Eq. (3) to within at least 3% (here and subsequently all the quantities are given in dimensional form):

$$A_x(y) = -\frac{\lambda_{\text{eff}}H^{\text{ext}}y}{\sqrt{\alpha\left[\left(\dfrac{W}{2}\right)^2 - y^2\right] + \beta\lambda_{\text{eff}}W}}. \qquad (4)$$
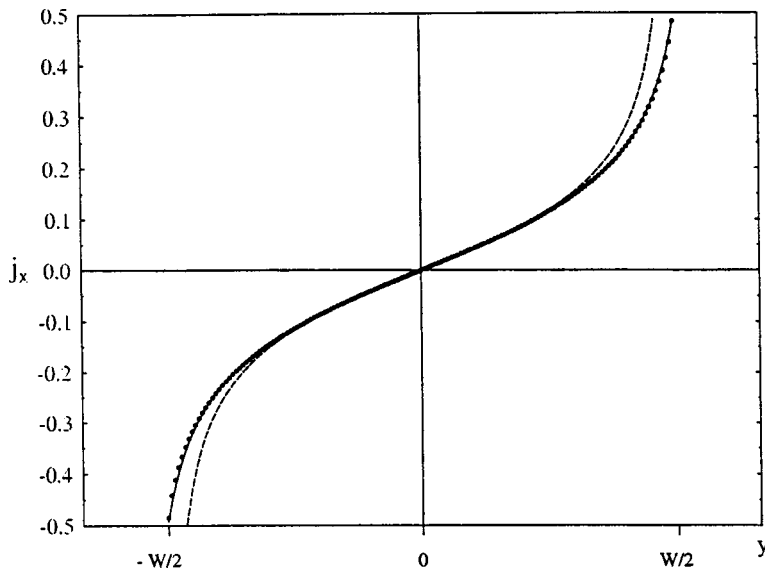
FIG. 1. Distribution of screening current density over film thickness. The circles give the numerical calculations of Eq. (3), the dashed curve gives the screening current distribution obtained in Ref. 2, and the solid curve gives the approximation (4), $H^{\text{ext}}=0.01$, and $W/\lambda_{\text{eff}}=20$.

The dependence $\alpha(W/\lambda_{\text{eff}})$ is plotted in Fig. 2 while the parameter β is accurately described by the expression $\beta=1/2\pi+\lambda_{\text{eff}}/W$. For widths $W<\lambda_{\text{eff}}$, the dependence $A_x(y)$ is almost linear: $A_x(y)\simeq-H^{\text{ext}}y$.

Expression (4) also describes the current density distribution over the film width since the vector potential and the current density (in dimensionless units) are related by the expression: $j_x=-A_x$.

This dependence $A_x(y)$ can be used to calculate the degree of concentration of the magnetic field $\gamma=H^{\text{edge}}/H^{\text{ext}}$ (where H^{edge} is the field at the edge) near the edge of the film in fields $H<H_s$:

$$\gamma=\frac{H^{\text{edge}}}{H^{\text{ext}}}=\frac{1}{\sqrt{\beta}}\left(\sqrt{\frac{\lambda_{\text{eff}}}{W}}+\frac{\alpha}{4\beta}\sqrt{\frac{W}{\lambda_{\text{eff}}}}\right). \qquad (5)$$

The value of γ determines the demagnetization factor n using the formula $n=1-1/\gamma$. For $W\gg\lambda_{\text{eff}}$ Eq. (5) gives

$$\gamma=\frac{\pi\sqrt{2\pi}}{10}\sqrt{\frac{W}{\lambda_{\text{eff}}}},$$

where the coefficient before the square root is a value of the order of unity. The difference between Eq. (5) and the expression for γ obtained using the numerical solution of Eq. (3) may reach 30%. This is because unlike the function $A_x(y)$, the derivative of Eq. (4) with respect to y (i.e., the magnetic field) accurately satisfies the numerical solution everywhere except for a narrow region near the edge of the film.

Expression (4) can be used to estimate H_s. Equating A_x at the edge $0.6\cdot\Phi_0/2\pi\xi$ (which corresponds to the current density at the edge, which is equal to the depairing current density), we obtain

$$H_s=1.2\frac{\Phi_0}{2\pi\xi}\sqrt{\frac{\beta}{\lambda_{\text{eff}}W}}. \qquad (6)$$
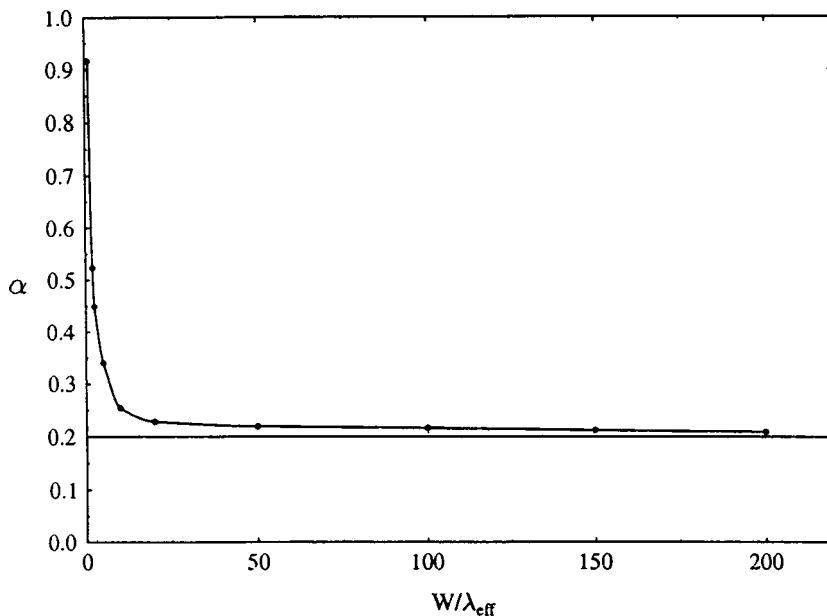

FIG. 2. Dependence of the parameter α on the ratio W/λ_{eff}.

Apart from the coefficient of the order of unity, the dependence (6) is the same as the expression obtained by Likharev[3] for wide ($W \gg \lambda_{eff}$) and narrow ($W \ll \lambda_{eff}$) films, respectively.

[1] M. R. Trunin, Usp. Fiz. Nauk **168**, 931 (1998).
[2] A. I. Larkin and Yu. N. Ovchinnikov, Zh. Éksp. Teor. Fiz. **61**, 1221 (1971) [Sov. Phys. JETP **34**, 651 (1971)].
[3] K. K. Likharev, Izv. Vyssh. Uchebn. Zaved. Radiofiz. **14**, 909 (1971).

Translated by R. M. Durham

Modeling of a vircator with internal TEM feedback

A. E. Dubinov and V. D. Selemir

Russian Federal Nuclear Center — Research Institute of Experimental Physics, Sarov
(Submitted June 8, 1999)
Pis'ma Zh. Tekh. Fiz. **25**, 89–94 (October 26, 1999)

The Karat electromagnetic PIC code is used for computer modeling of a vircator with internal TEM feedback proposed by the authors. It is shown that the output power can be effectively controlled by varying the feedback length. © *1999 American Institute of Physics.*
[S1063-7850(99)03110-9]

Virtual-cathode microwave oscillators, known as vircators, are among the most promising devices in high-power relativistic rf electronics. Their advantages are fairly obvious and have been elaborated in the literature on many occasions.[1–3]

The main features of the electron dynamics in vircators and the mechanisms for the generation of microwave radiation therein are broadly understood and it has become clear that the onset of radiative instability (in other words stimulated emission), avoiding saturation or quenching for as long as possible, is required to achieve further development of these devices and enhance their efficiency.

The basic principle for obtaining a stimulated process is to achieve positive feedback which causes instability. It was previously assumed that feedback could be established in vircators by means of electrons reflected from the virtual cathode and returned to the cathode or even by means of charge density waves in the reflected beam.[2–5] However, it was shown in Refs. 6 and 7 that this feedback only plays a positive role at the initial stage of existence of the virtual cathode and then leads to the onset of strong electron beam turbulence near the virtual cathode[8] and the radiative instability is quenched.

There is thus a need to establish feedback artificially, not using the reflected electron beam but by some other means. The simplest technical solution may involve deflecting a small fraction of the microwave radiation generated by the vircator and transporting it by means of a waveguide to the diode region of the vircator so that the microwave phase is ''positive'' near the cathode.

Gadetskiĭ *et al.*[9] and Korovin *et al.*[10] examined various design solutions for achieving positive feedback in vircators using waveguides, although these systems are not symmetrical and consequently are extremely cumbersome and nonoptimal in terms of the parasitic inductances of the high-voltage circuits. Dubinov *et al.*[11] proposed a vircator system in which feedback is achieved in a system of internal coaxial lines formed by a cylindrical slot in a cathode *2* with the cylindrical part of the anode *3* protruding into this slot (Fig. 1a). A TEM microwave can propagate in these lines for which the absence of dispersion may be additional advantage of this feedback system.

The aim of the present study was therefore to check the efficiency of the vircator proposed in Ref. 11 and to examine

the following aspects: whether the phase of the return microwaves and the output power can be effectively controlled by regulating the length of the coaxial feedback line and whether a considerably greater output power can be achieved, compared with an ordinary vircator without feedback.
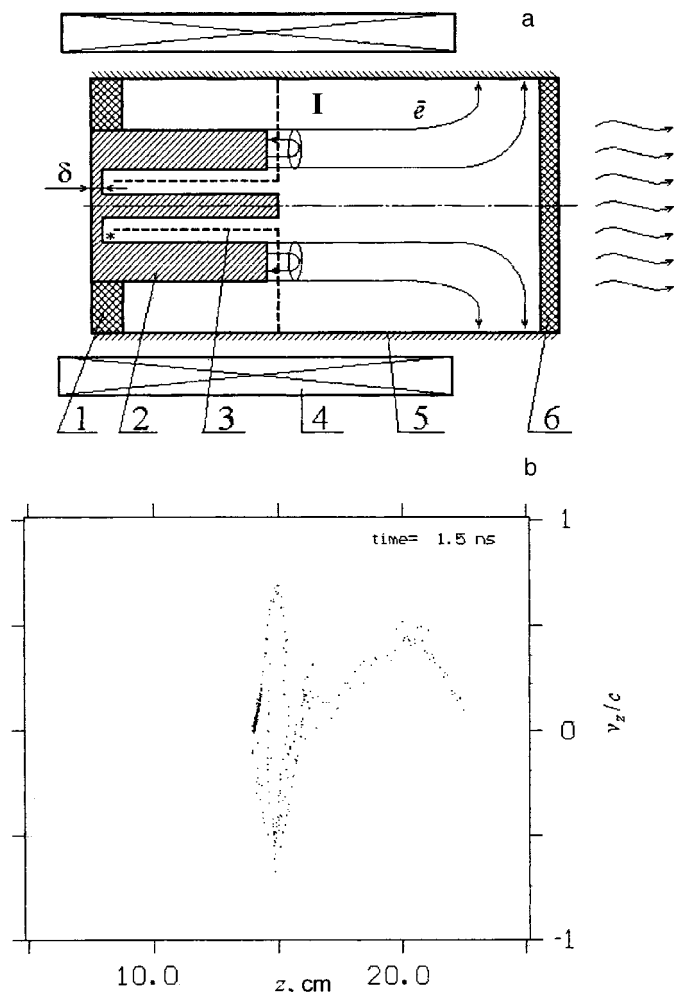

FIG. 1. Schematic of vircator with TEM feedback (a) and matched electron phase portrait (b); *1* — high-voltage insulator, *2* — cathode, *3* — anode grid, *4* — solenoid, *5* — anode, *6* — microwave exit window; the position of the detector for the azimuthal component of the magnetic field $H_\varphi(t)$ is indicated by the asterisk; I — virtual cathode.
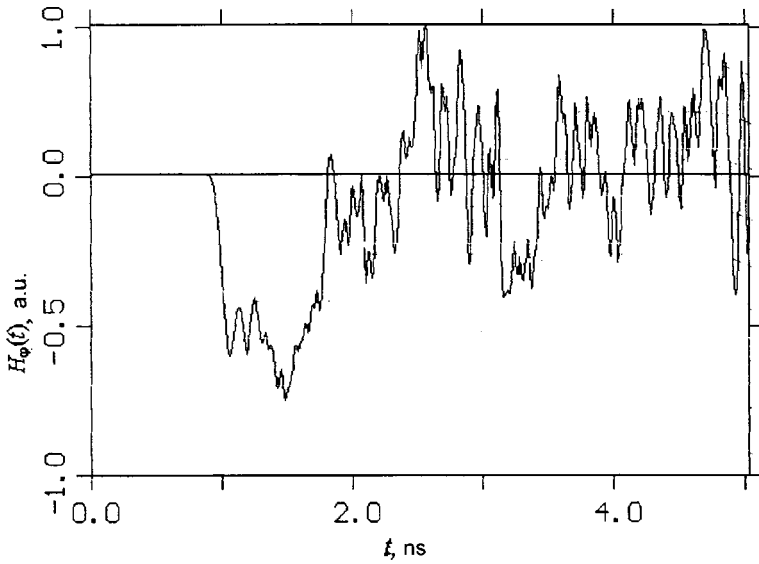
FIG. 2. Calculated oscilloscope trace of the azimuthal component of the magnetic field $H_\varphi(t)$.

For these investigations we selected a method of computer modeling using the well-known Karat electromagnetic, self-consistent relativistic PIC code.[12] The modeled region is as shown in Fig. 1a.

We assumed that a high-voltage pulse in the form of a high-voltage wave of amplitude 300 kV having a 1 ns leading edge is applied to the cathode *2* and the vircator is located in the 5 T magnetic field of a solenoid *4*, which decreases to zero near the exit window *6* for the microwave radiation. This magnetic field configuration was selected first, to force the beam drift electrons to reach the anode tube *5* to close the charging circuit and second, to separate the Coulomb field of the beam from the emitted microwave field in the cross section near the window in calculations of the Poynting flux vector. The emission of electrodes from the cathode was determined assuming that the extracting electric field near the cathode is zero.

At the point indicated by the asterisk in Fig. 1a we placed a ''detector'' to record the time profile of all the microwave field components in the feedback line.

The phase portrait of the beam shown in Fig. 1b shows that immediately after the planar section of the anode a virtual cathode forms in the tubular beam, approximately at the point shown in Fig. 1a.

Figure 2 shows a typical calculated ''oscilloscope trace'' of the azimuthal component of the magnetic field $H_\varphi(t)$ at the site of the detector, which reveals two characteristic sections: the first section (approximately 1 ns $< t < 2$ ns) corresponds to the high-voltage line-charging wave when a pulsed voltage is applied to the cathode while the second section ($t > 2$ ns) corresponds to the generation of microwave radiation. This behavior indicates that a microwave propagates in the coaxial feedback lines, implementing a particular locking regime.

The value of δ was varied in the calculations (Fig. 1a) so that the difference between the depth of the slot in the cathode and the length of the cylindrical part of the anode was constant (1 cm) and the position of the detector varied accordingly.

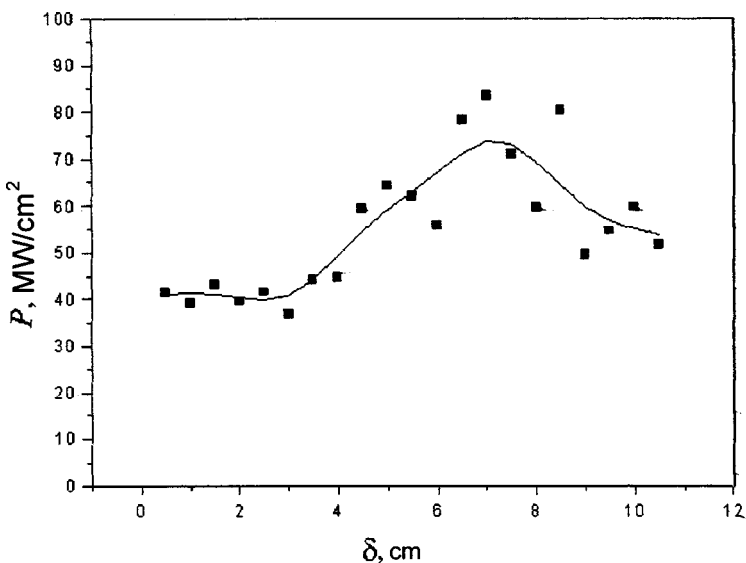Figure 3 gives the average power flux after 5 ns in the

FIG. 3. Average microwave power flux as a function of δ: symbols — calculated values, solid curve — smoothed dependence.

cross section near the radiation exit window plotted as a function of δ, from which it can be seen that this dependence has a maximum and minimum corresponding to different phases of the microwave feedback wave and differing from each other by $\mu = 83.6 \, \mathrm{MW \cdot cm^{-2}}/36.7 \, \mathrm{MW \cdot cm^{-2}} \approx 2.3$. We note that an ordinary vircator without a slot in the cathode and without a cylindrical anode section only gives $40.9 \, \mathrm{MW \cdot cm^{-2}}$.

Thus, the results of this computer modeling indicate that the vircator proposed in Ref. 11 can produce a more efficient source of microwave radiation with controllable power, demonstrating all the ideas inherent in it.

The authors thank V. P. Tarakanov for assistance with the work.

[1] A. A. Rukhadze, S. D. Stolbetsov, and V. P. Tarakanov, Radiotekh. Élektron. **37**, 385 (1992).

[2] B. V. Alyokhin, A. E. Dubinov, V. D. Selemir, O. A. Shamro, K. V. Shibalko, N. V. Stepanov, and V. E. Vatrunin, IEEE Trans. Plasma Sci. **945**, 945 (1994).

[3] A. E. Dubinov and V. D. Selemir, Zarub. Radioélektron. No. 4, 54 (1995).

[4] V. E. Vatrunin, A. E. Dubinov, and V. D. Selemir, Voprosy Atomnoĭ Nauki i Tekhniki Ser. Teoreticheskaya i Prikladnaya Fizika No. 2, 24 (1994).

[5] V. E. Vatrunin, A. E. Dubinov, V. D. Selemir, and N. V. Stepanov, in *Lectures on Microwave Electronics and Radio Physics*, Book 2 [in Russian], Saratov (1996), p. 89.

[6] A. E. Dubinov, V. D. Selemir, and A. V. Sudovtsov, Élektronnaya Tekhnika Ser. 1, SVCh-Tekhnika, No. 1(469), 7 (1997).

[7] A. E. Dubinov and V. D. Selemir, Pis'ma Zh. Tekh. Fiz. **24**(4), 41 (1998) [Tech. Phys. Lett. **24**, 142 (1998)].

[8] V. E. Vatrunin, A. E. Dubinov, and V. D. Selemir, Pis'ma Zh. Tekh. Fiz, **22**(23), 92 (1996) [Tech. Phys. Lett. **24**, 994 (1996)].

[9] N. P. Gadetskiĭ, I. I. Magda, S. I. Naĭsteter, Yu. V. Prokopenko, and V. I. Chumakov, Fiz. Plazmy **19**, 530 (1993) [Plasma Phys. Rep. **19**, 273 (1993)].

[10] S. D. Korovin, I. V. Pegel, S. D. Polevin, and V. P. Tarakanov, in *Digest of Technical Papers of the 11th IEEE International Pulsed Power Conference*, Baltimore, 1997, Vol. 1, p. 736.

[11] A. E. Dubinov, I. V. Konovalov, N. N. Makarova, and V. D. Selemir, Russian Patent No. 2123740, MKI: H 01 J 25 / 68; Byull. Izobret. No. 35 (1998).

[12] V. P. Tarakanov, *User's Manual for Code* KARAT, Berkley Research Associates, Springfield, VA (1992).

Translated by by R. M. Durham